

CONFRONTING ASTROPHYSICAL UNCERTAINTIES IN THE DIRECT DETECTION OF DARK MATTER

BRADLEY J. KAVANAGH, MSci

Thesis submitted to the University of Nottingham for the degree of Doctor of
Philosophy

May 24, 2014

Abstract

Published work

Parts of the work described in this thesis have appeared in the following published works:

1. *Parametrizing the local dark matter speed distribution: a detailed analysis*
B. J. Kavanagh
Submitted to Phys. Rev. D, arXiv:1312.1852
2. *WIMP physics with ensembles of direct-detection experiments*
A. H. G. Peter, V. Gluscevic, A. M. Green, **B. J. Kavanagh**, S. K. Lee
Submitted to Phys. Dark Universe, arXiv:1310.7039
3. *Model independent determination of the dark matter mass from direct detection*
B. J. Kavanagh and A. M. Green
Phys. Rev. Lett. 111, 031302 (2013), arXiv:1303.6868
4. *Improved determination of the WIMP mass from direct detection data*
B. J. Kavanagh and A. M. Green
Phys. Rev. D 86, 065027 (2012), arXiv:1207.2039

Acknowledgements

*This is dedicated to all of those with big egos
Never fakin', we get the dough and live legal*

—Dr. Dre

Contents

Contents	iv
List of Figures	vi
List of Tables	xi
1 Introduction	1
1.1 Evidence for dark matter	2
1.2 Properties of dark matter	8
1.3 Particle dark matter candidates	11
1.4 Detection of dark matter	13
2 Direct detection of dark matter	19
2.1 Introduction	19
2.2 Direct detection formalism	20
2.3 Direct detection experiments	28
2.4 Uncertainties	33
2.5 Conclusion	42
3 Parameter Reconstruction	44
3.1 Introduction	44
3.2 Frequentist statistics	45
3.3 Bayesian statistics	48
3.4 Exploring the parameter space	50
3.5 Likelihood examples	53
3.6 Conclusions	54
4 Parametrising the speed distribution	56
4.1 Uncertainties in $f(v)$	57
4.2 Binned speed distribution	60

4.3	Momentum parametrisation for a single experiment	68
4.4	Momentum parametrisation for several experiments	73
4.5	Discussion	84
4.6	Conclusion	86
5	A polynomial parametrisation of the speed distribution	88
5.1	Parametrising the logarithm of $f(v)$	89
5.2	Parameter reconstruction	91
5.3	Results	96
5.4	Varying m_χ	101
5.5	Statistical properties	103
5.6	Reconstructing $f_1(v)$	107
6	Breaking the cross section degeneracy: neutrino telescopes	116
7	Directional detection	117
7.1	Introduction	117
7.2	Directional event rate	118
7.3	Directional experiments	121
7.4	Reconstructing the velocity distribution	124
7.5	Discretising the velocity distribution	126
7.6	Discretisation for general N	134
7.7	Conclusion	134
8	Conclusions	140
	Bibliography	141

List of Figures

1.1	CMB anisotropies measured by the Planck experiment	4
1.2	Schematic illustration of galaxy rotation curves	6
1.3	Schematic dark matter interactions	14
2.1	Examples of spin-independent event spectra for direct detection experiments	27
2.2	Examples of dark matter speed distributions	40
3.1	Likelihood-based parameter inference	47
3.2	Posterior-based parameter inference	50
4.1	Biased reconstruction of WIMP parameters	58
4.2	Binned approximation to the SHM	62
4.3	Range of accessible WIMP speeds for mock direct detection experiments	63
4.4	Distribution of reconstructed WIMP masses using the binned speed parametrisation	65
4.5	Distribution of the pull statistic δ using the binned speed parametri- sation	66
4.6	Reconstructed speed distribution and mean inverse speed using the binned speed parametrisation	67
4.7	Reconstructed mean inverse speed for the SuperCDMS-like ex- periment	68
4.8	Distribution of the reconstructed scale parameter, D_{rec} , for the Argon experiment using the momentum parametrisation	71
4.9	Reconstructed momentum distribution for a single Argon ex- periment using a benchmark of a 50 GeV WIMP and the SHM	72
4.10	Comparison of WIMP masses reconstructed using the binned speed and momentum parametrisations	75

4.11	Reconstructed momentum distribution from all three mock experiments using a benchmark of a 50 GeV WIMP and the SHM	76
4.12	Speed distributions and mean inverse speeds for the Standard Halo Model (SHM), SHM + Dark disk (SHM+DD) and Via Lactea 2 (VL-2) distribution functions	78
4.13	Distribution of reconstructed masses using the binned momentum distribution for a 50 GeV WIMP with SHM, SHM+DD and VL2 distribution functions	79
4.14	Distribution of reconstructed masses using the binned momentum distribution for a 100 GeV WIMP with SHM, SHM+DD and VL2 distribution functions	80
4.15	Reconstructed speed distribution from all three mock experiments using the momentum parametrisation method. The benchmark is a 50 GeV WIMP and the SHM distribution function. The upper pane shows the underlying SHM speed distribution (solid blue) and the fitted values of the speed bin parameters (red points). The errors on the bin values are within-chain standard deviations as described in Sec. ???. The lower pane shows the mean inverse speed corresponding to these fitted values (dashed red line) and the true mean inverse speed (solid blue). The underlying distributions have been rescaled by α for comparison to the reconstructions.	82
4.16	As Fig. 4.15 for a 100 GeV WIMP with DD distribution function using 5 momentum bins (left panes) and 7 momentum bins (right panes).	83
4.17	Distribution of reconstructed masses using the 7-bin momentum method for 250 reconstructions for a DD benchmark distribution. The true mass of 100 GeV is shown as a dashed vertical line.	84
4.18	Reconstructed speed distribution from all three mock experiments using a benchmark of a 50 GeV WIMP with SHM distribution. The reconstructed values have been rescaled by α for comparison to the true distributions. <i>SHM(solidblue), DD(dashedgreen) and VL-2(dottedred).</i> . . .	85
5.1	Examples of $\ln f(v)$ polynomial distributions	91

5.2	Several of the benchmark speed distributions used in this work. They are defined in Eqs. 5.5 and 5.6 with parameters from Tab. 5.2. These distributions are the SHM (solid blue), SHM+DD (dashed green), Lisanti et al. (dot-dashed red) and the stream (dotted magenta).	95
5.3	Benchmark speed distributions used in Sec. 5.3.1 to test the performance of the parametrization as a function of the number and type of basis functions.	97
5.4	Bayesian information criterion (BIC) as a function of the number of basis functions for an underlying ‘bump’ distribution function, 50 GeV WIMP and using Legendre polynomial basis functions (upper panel). Also shown (lower panel) are the reconstructed WIMP mass (dashed blue line), 68% confidence interval (shaded blue region) and underlying WIMP mass (solid horizontal black line).	99
5.5	As Fig. 5.4 but for an underlying ‘double-peak’ distribution function.	100
5.6	Time taken (using 4 processors in parallel) for the reconstruction of the ‘bump’ benchmark, as a function of number of basis functions. The time taken using the Chebyshev basis (blue squares) grows more slowly with N than for the Legendre basis (red triangles).	101
5.7	Reconstructed WIMP mass m_{rec} (central dashed blue line) as a function of input WIMP mass m_χ as well as 68% and 95% intervals (inner and outer blue dashed lines respectively). The line $m_{\text{rec}} = m_\chi$ (solid red line) is also plotted for reference.	102
5.8	As fig. 5.7 but including the effects of finite energy resolution and non-zero backgrounds, as described in the text.	104
5.9	Distribution of the reconstructed mass m_{rec} for 250 mock data sets generated using several benchmark speed distributions, defined in Sec. 5.2.2. These are the SHM (top), SHM+DD (middle) and Lisanti et al. (bottom) distributions. The input WIMP mass of $m_\chi = 50$ GeV is shown as a vertical dashed red line.	106

5.10	Reconstructed speed distribution for a single realisation of data, generated for a 50 GeV WIMP. 68% and 95% credible intervals are shown as dark and light shaded regions respectively, while the underlying SHM distribution function is shown as a solid blue line.	108
5.11	Reconstructed speed distribution for the same realisation of data as Fig. 5.10. In this case, we have also normalized $f_1(v)$ to unity above $v_a \approx 171 \text{ km s}^{-1}$ (vertical dashed line). This is the lowest speed accessible to the experiments for a WIMP of mass 50 GeV. 68% and 95% credible intervals are shown as dark and light shaded regions respectively, while the underlying SHM distribution function is shown as a solid blue line.	109
5.12	Mean reconstructed values of the rescaled mean inverse speed $\eta(v)/\alpha(v)$ at several values of v , calculated over 250 realisations of data using a 50 GeV WIMP and underlying SHM distribution function. Errorbars indicate the mean upper and lower limits of the 68% credible intervals. The underlying form of $\eta(v)/\alpha(v)$ obtained from the SHM is shown as a solid blue line.	110
5.13	Rescaled mean inverse speed $\eta(v)/\alpha(v)$, reconstructed from a single realisation of data using a 50 GeV WIMP and underlying SHM distribution function. At each value of v we calculate 68%, 95% and 99% credible intervals (shown as shaded intervals). We also show the calculated values of $\eta(v)/\alpha(v)$ for several possible benchmark speed distributions: SHM (solid blue), SHM+DD (dashed green), Lisanti et al. (dot-dashed red) and stream (dotted magenta). The benchmark curves are truncated when the underlying distribution function goes to zero.	111
5.14	As Fig. 5.13, but using as input a Lisanti et al. speed distribution and an exposure time which is 2.5 times longer.	112
5.15	As Fig. 5.14, but focusing on the region around $v \sim 400 \text{ km s}^{-1}$. Notice that in the range $400 - 550 \text{ km s}^{-1}$, both the SHM and SHM+DD curves lie at or below the lower limit of the 95% credible interval.	113
7.1	Illustration of DM-nucleus scattering	118
7.2	Radon transform examples	122
7.3	Discretised velocity distribution for $N = 2$ components	135

7.4	Discretised Radon transform for $N = 2$ components	136
7.5	Discretised velocity distribution for $N = 3$ components	137
7.6	True and approximate transforms when the full velocity distribution is discretised into $N = 3$ directional pieces. In the ‘forward’ case $\cos \theta \in [1/2, 1]$, in the ‘backward’ case $\cos \theta \in [-1, -1/2]$, and in the ‘transverse case’ $\cos \theta \in [-1/2, 1/2]$	138
7.7	True and approximate folded transforms when the full velocity distribution is discretised into $N = 3$ directional pieces. In the ‘longitudinal’ case $ \cos \theta \in [1/2, 1]$ while in the ‘transverse case’ $ \cos \theta \in [0, 1/2]$	139

List of Tables

1.1	Cosmological parameters obtained by the Planck Collaboration	3
2.1	Summary of current and completed direct detection experiments.	33
4.1	Parameter values for the three mock experiments used in this work, chosen to closely match those used in Ref. [1]. The meanings of the experimental parameters are described in Sec. 4.2.1.	63
4.2	Coverage statistics for the speed and momentum parametrisation methods for a 50 GeV SHM benchmark model.	76
4.3	68% and 95% confidence interval coverage results for the momentum parametrisation method using a variety of benchmark parameters, as defined in Sec. ??	81
5.1	Summary of experimental parameters used in this work, defined in Sec. 5.2.1. An exposure of $t_{\text{exp}} = 2$ years is used for all 3 experiments.	92
5.2	Summary of speed distribution benchmarks used in this work. Some benchmarks are modelled as mixtures of two gaussian components (defined in Eq. ??), for which we give the fractional contribution of each component (labelled ‘Fraction’). The remaining parameters are defined in Eqs. ?? and ?? and the accompanying text. The ‘bump’ and ‘double-peak’ distributions are discussed in Sec. 5.3.1.	94
5.3	Summary of the priors on the parameters used in this work. The background rate R_{BG} is defined in Sec. 5.4 while the $\{a_k\}$ are the polynomial coefficients used in the parametrisation. . . .	94
5.4	Summary of the MultiNest sampling parameters used in this work.	95

5.5	Reconstructed mass using the parametrization presented in this chapter, as well as the the speed binning and momentum binning methods of Chapter 4 for comparison. The benchmark used is a stream distribution function described in Somewhere! and a 50 GeV WIMP. In all cases, 5 speed distribution parameters (either bins or basis coefficients) are used.	96
5.6	Mean bias $\langle b \rangle$ in the reconstructed log WIMP mass (Eq. 5.10). This was calculated over 250 realisations using three different benchmark speed distributions.	105
5.7	Coverage of 68% and 95% credible intervals calculated from 250 data realisations each for three benchmark speed distributions. The concept of coverage is described in the text of Sec. 5.5. . . .	107

Nomenclature

$\sigma_{SI(SD)}$ WIMP nucleon spin-independent (spin-dependent) cross section

m_χ WIMP mass

Chapter 1

Introduction

What is dark matter? For a question so central to cosmology and particle physics, the prospects for finding an answer do not at first glance seem promising. The interaction of dark matter (DM) particles must be very weak in order to evade a myriad of bounds set by precision astrophysical and cosmological tests. Our failure to observe dark matter particles thus far tells us that their interactions must be even weaker still. The effort to detect these interactions both on Earth and in the wider universe is a vast technological and scientific challenge.

However, DM is almost ubiquitous in the universe and such efforts are advancing rapidly. The detection of particle DM using terrestrial detectors would give strong clues about the nature and identity of DM. However, the analysis of these so-called ‘direct detection’ experiments is plagued with uncertainties. One such uncertainty is in our understanding of the astrophysical speed distribution of dark matter, which influences the typical energies which would be deposited in a detector in the lab. If these uncertainties can be overcome, direct detection promises to be a powerful probe of both the particle physics and astrophysics of DM.

Without a detection of a possible particle candidate, then, the question ‘What is dark matter?’ is perhaps best answered by reviewing the current evidence for its existence. Evidence for dark matter is found on scales from the Milky Way up to the cosmological horizon, with a range of observations which cannot be adequately explained with the observed constituents of the universe. Dark matter is an invisible component introduced to reconcile these observations with the known laws of physics - most importantly, General Relativity. Beyond this general definition, there are a wide range of particle physics candidates which may play the role of dark

matter. These typically derive from theories of physics beyond the Standard Model, meaning that the study of the properties of dark matter can shed light on theories of high energy physics. Many of these proposed dark matter candidates have weak but non-zero interactions with particles of the Standard Model, leading to several avenues through which it is hoped the non-gravitational detection of dark matter may soon be achieved.

In this chapter, we summarise the evidence in support of the dark matter paradigm, including constraints from precision cosmology. We discuss some of the features which particle DM must possess, as well as describing a few specific candidates in more detail. Finally, we discuss current progress and constraints from direct and indirect searches for particle dark matter.

1.1 Evidence for dark matter

Dark matter is a key component of the Λ CDM paradigm of modern cosmology. In this framework, the energy density of the universe today is dominated by the constant and uniform contribution of the vacuum, Λ , also referred to as Dark Energy. This contribution exerts a negative pressure and drives the accelerating expansion of the universe which was the subject of the 2011 Nobel Prize in Physics [2, 3]. However, the formation of structure in the early universe is driven by the clustering of an inert, slow moving and as yet undetected matter component [4], Cold Dark Matter (CDM). The fact that DM is non-interacting means that it begins to collapse gravitationally earlier in cosmic time than baryonic matter. After decoupling, baryons then fall into the gravitational wells produced by the infalling DM structures. Without DM, the baryonic matter in the universe could not have had enough time to collapse to form the range of gravitationally bound structures we see today [4, 5]

Cosmological experiments sensitive to the expansion and structure formation history of the universe allow us to precisely determine the contributions of the various different components to the energy density of the universe (see e. g. WMAP [6], BOOMERanG [7], BOSS [8], BICEP2 [9] and CFHTLenS [10, 11] to name just a few). For example, Baryon Acoustic Oscillations (BAOs) are a feature imprinted on the distribution of matter in the universe by acoustic waves prior to recombination. BAOs can be measured by using galaxy redshift surveys (such as SDSS [12]) to map

Parameter	68% limits
Ω_Λ	0.686 ± 0.020
$\Omega_m h^2$	0.1423 ± 0.0029
$\Omega_b h^2$	0.02207 ± 0.00033
$\Omega_c h^2$	0.1196 ± 0.0031

Table 1.1: Energy density Ω of the cosmological constant (Λ), total matter (m), and separate baryonic (b) and cold dark matter (c) components in units of the critical density, as obtained by the Planck Collaboration [15]. The Hubble parameter is defined as $H_0 = 100 h \text{ km s}^{-1} \text{ Mpc}^{-1}$.

out the large scale structure of the universe and they provide a ‘standard ruler’ for measuring cosmological distances. Type-Ia Supernovae provide ‘standard candles’ which can be used to measure luminosity distances in the universe. Redshift surveys of these supernovae [13] then allow us to reconstruct these distance scales over cosmic time. Complementary information from these probes and others allow us to constrain the expansion history of the universe and therefore the various contributions to the density of the universe.

A particularly sensitive probe for determining the dark matter contribution to the energy budget of the universe is the measurement of the temperature anisotropies of Cosmic Microwave Background (CMB) photons. These contain an imprint of the acoustic oscillations of the baryon-photon fluid during the era of recombination. The scale of these oscillations is sensitive to the size of the gravitational potential generated in the early universe by dark matter, which does not interact with the photons [4]. The recent Planck experiment [14] measured the angular power spectrum of these CMB temperature anisotropies. Figure 1.1 shows the results of these measurements, as well as the best fit 6-parameter Λ CDM model. The contributions of the cosmological constant, the total matter component, and the separate baryonic and dark matter components to the total energy density of the universe are shown in Table 1.1, constrained with an accuracy of less than 3%. These results point to the conclusion that $\sim 84\%$ of the matter content of the universe is in fact dark.

However, the evidence for dark matter is not purely cosmological. In 1933, Zwicky measured the velocity dispersion of galaxies in the Coma cluster [16]. An application of the Virial Theorem indicated a gravitational mass in the cluster which was several hundred times bigger than that ex-

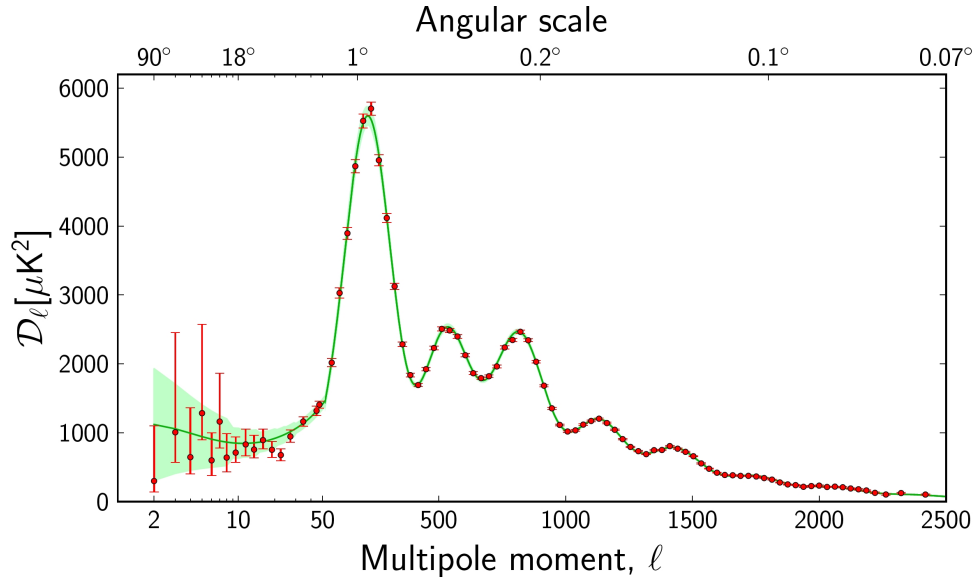


Figure 1.1: Power spectrum of CMB temperature anisotropies as measured by the Planck satellite. Data are shown as red points with the best fit Λ CDM cosmological model shown as a green line. Reproduced from Ref. [14]. *Check that's the right citation...*

pected from the luminosity of the member galaxies. It is now known that some of this mass is in the form of hot (~ 1 million K), X-ray emitting intracluster gas [17]. Nonetheless, a discrepancy remains; current estimates of the mass-to-light ratio of the Coma cluster give a value of roughly 150 times that of the Sun [18, 19]. The Coma cluster does not appear to be unusual. Measurements of the masses of a large number of galaxy clusters using gravitational lensing [20], X-ray observations [21] and dynamical estimates [22] indicate that a significant fraction of a cluster's mass must be dark.

The success of the Λ CDM paradigm is also borne out in results from N-body simulations. These simulations track the evolution of structure in the universe by modeling the dynamics and gravitational interactions of a large number of particles starting from some initial conditions. These may be horizon-scale cosmological simulations, tracing the collapse of the initial density perturbations after decoupling (such as the the Millenium simulation [23]), or galaxy-scale simulations, tracing the formation and growth of a small number of galaxies starting from initial conditions at intermediate redshift (such as the Via Lactea [24] and Aquarius [25] simulations).

Many N-body simulations are DM-only, simulating only the gravita-

tional dynamics of collisionless particles. However, an increasing number are incorporating baryonic physics such as gas dynamics, as well as stellar evolution, chemical enrichment and a variety of feedback processes (see e.g. [26, 27]). Appropriately accounting for these factors is extremely complex and in some cases the strength of these processes is unknown and must be tuned in the simulations to match observations [28]. Due in part to these difficulties, the impact of baryonic physics on the formation of galaxies and the properties of DM haloes is still uncertain (see for example Refs. [29, 30]). I will revisit this topic - and its consequences for the direct detection of dark matter - in Chapter 2.

A variety of sophisticated computational techniques (such as smoothed particle hydrodynamics [31], adaptive mesh refinement [32] and moving mesh cosmology [33]) have been employed and refined to make such simulations computationally feasible and to allow higher and higher resolutions to be reached. In spite of this, computational limitations mean that the highest resolution simulations still use ‘particle’ masses of the order of $10^5 M_\odot$ [30], many orders of magnitude more massive than the $O(\text{GeV-TeV})$ particles expected to make up the universe’s dark matter.

In spite of this, a consistent picture has emerged from a vast array of N-body simulations. The distribution of galaxies observed in large scale structure surveys matches that predicted by N-body simulations over a range of distance scales [23]. In addition, N-body simulations have begun to accurately reproduce the observed populations of elliptical and spiral galaxies [27], as well as obtaining Milky Way-like simulated galaxies [26].

N-body simulations also suggest that galaxies such as the Milky Way should be embedded in a large, approximately spherical dark matter halo. This is corroborated by observations of the rotation curves of spiral galaxies. In particular, the circular velocity of stars in these galaxies is observed to be approximately constant out to large galactocentric distances [34, 35]. In fact, observations of hydrogen 21cm emission indicate that the constancy of the circular velocity extends well beyond the optical edge of galaxies [36, 37].

This is shown schematically in Fig. 1.2. The majority of the mass of the luminous disc is concentrated at small radii, suggesting that there should be a Keplerian decay of the circular velocity at large radii: $v \sim r^{-1/2}$. However, the inclusion of a non-luminous dark matter halo can reconcile this expectation with the observed flat rotation curves. The density profiles

$\rho(r)$ required to provide a good fit to rotation curve data are consistent with those obtained from N-body simulations, such as the Navarro-Frenk-White profile

$$\rho(r) = \frac{\rho_0}{r/R_s(1 + r/R_s)^2}, \quad (1.1)$$

which is described by the central density ρ_0 and a scale radius R_s . This provides a good cross-check between the results of N-body simulations, which span scales up to the cosmological, and galactic-scale observations of the local universe. The rotation curve of the Milky Way itself has also been studied [38–40] and found to have an almost flat rotation curve. Using a variety of techniques, it is also possible to measure a non-zero DM density near the Sun’s position. An understanding of this density has significant implications for the study of dark matter detection and we defer a detailed discussion to Chapter 2.

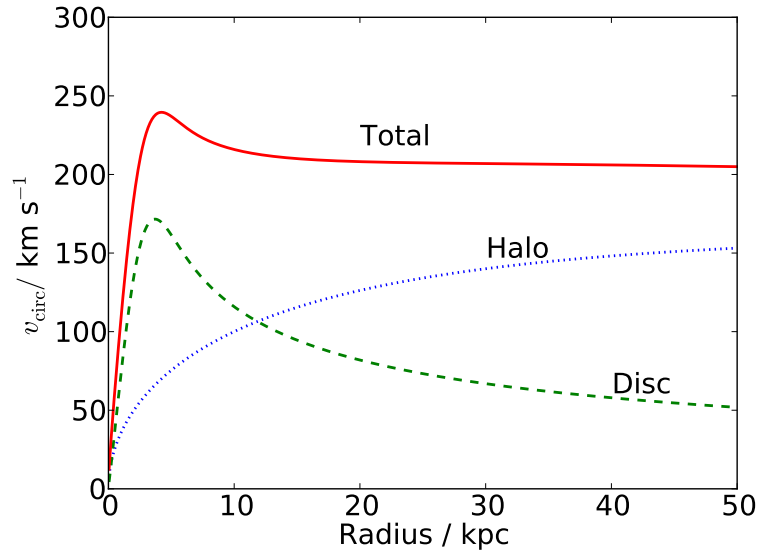


Figure 1.2: Schematic illustration of galaxy rotation curves (circular velocity as a function of galactocentric distance). The contribution to the circular velocity from the luminous disc (green dashed line) and dark matter halo (red dotted line) are shown, as well as the total circular velocity (solid blue line).

We see that evidence for dark matter appears over a wide range of distance scales, from the cosmological horizon down to our own Milky Way. Dark matter is required to explain the formation and growth of large scale structure, the dynamics of both galaxies and galaxy clusters and the

anisotropic temperature distribution of the CMB among others. In spite of this, there remain several problems and unanswered questions with the dark matter paradigm.

1.1.1 Problems with dark matter

There have emerged several issues with the dark matter dominated model of structure formation as studied with N-body simulations. For example, DM-only simulations predict the existence of a large number of massive subhalos around Milky Way-size galaxies [25]. Using semi-analytical models of galaxy formation Kauffmann et al. [41] predicted that a Milky Way-size halo should host over 100 subhalos massive enough to support observable satellite galaxies. However, the known population of dwarf spheroidal (dSph) satellite galaxies for the Milky Way is on the order of 20 [42], although more ultra-faint satellites are still being discovered (e.g. see Ref. [43]). This discrepancy between the predicted and observed amount of substructure in CDM structure formation is often referred to as the ‘missing satellite problem’ [44].

A related issue is the so-called ‘too big to fail’ problem, which concerns the density of dark matter subhalos. In particular, it is found that the most massive DM subhalos found in N-body simulations are too massive to host the brightest of the Milky Way’s dSph satellites [45]. If the observed dSph galaxies are hosted instead by less massive subhalos, this leaves a large number of more massive DM halos which have not yet been accounted for [46].

Finally, there is also a discrepancy between observed and simulated density profiles for dSphs: the ‘Core-Cusp’ problem (for a review, see Ref. [47]). Cosmological simulations indicate that the DM density should be sharply peaked near the centre of low surface brightness and dSph galaxies [48, 49]. In contrast, observations of the rotation curves of a large number of galaxies suggests the presence of a core - a flat dark matter density profile near the centre [50, 51]. While these results are still under contention (for example, Ref. [52] find rotation curves consistent with *cuspy* density profiles), they may indicate a discrepancy between the process of structure formation in the universe and that implied by Λ CDM.

A number of possible solutions to these issues have been suggested. Baryonic effects such as dynamical friction and stellar and supernova feed-

back (see for example Refs. [53–55]) can lead to the expulsion of DM from the centres of subhalos, reducing the total halo mass and leading to a flatter central density profile. Others have suggested that a *warm* dark matter model may be a better fit to the data [56–58], reducing the amount of structure on small scales, as we will discuss in Sec. 1.2. Whatever the ultimate resolution of these problems, it is clear that dark matter dominated structures such as dSph galaxies are a testing ground for an even more precise understanding of structure formation in the DM paradigm.

There remains one problem which is of a much more theoretical nature. Dark matter is invoked to account for missing mass in a wide range of scenarios. However, this missing mass has not yet been observed indicating that it must interact only very weakly with photons and other particles of the standard model. In fact, as we shall see, there is strong evidence that particles making up the universe’s dark matter cannot be baryonic and must originate from beyond the Standard Model of particle physics. In the next section, we investigate what more can be inferred about the nature of particle dark matter and explore some well-motivated candidates.

MACHOs? MOND?

1.2 Properties of dark matter

Beyond its gravitational contribution to the universe, we appear to know little about the nature of particle dark matter. However, the success of modern cosmology and the lack of a confirmed detection so far means that we do have a grasp on some of the properties of any potential candidate.

For example, DM can have no significant electromagnetic charge, otherwise it would have been seen in a range of searches [59–62]. DM carrying bare color charge can also be excluded due to the disruption it would cause to galaxy formation [63] and the formation of the CMB [64]. Any particle candidate must also be long-lived - otherwise it cannot play the role of dark matter today. For models in which DM is not indefinitely stable, this allows us to place stringent limits on the lifetime of the DM particle [65, 66].

In an effort to summarise what is known about dark matter, Taoso et al. [67] present a ‘10-point test’ which must be passed by any particle before it can be considered as a viable dark matter candidate. Here, I will briefly discuss three of these points, namely, that the DM candidate must

be cold, produced with the appropriate relic density and compatible with primordial nucleosynthesis.

1.2.1 Coldness

Dark matter cannot be hot. That is, DM must have been travelling non-relativistically when it decoupled from the thermal bath in the early universe. The typical speed of DM particles in the early universe defines the so-called *free-streaming length*. Below this length-scale, density perturbations are suppressed due to Landau damping [68]. For non-relativistic species, this free-streaming length scales as $m_\chi^{-1/2}$ for thermal relics of mass m_χ [69]. For particle candidates which are too light - and which therefore travel too quickly after decoupling - small scale structures cannot form and cannot match the distribution of structures we see today. In practise, this typically means that DM cannot have a mass greater than around 1 keV [70]. It is typically assumed that dark matter is significantly heavier than this, decoupling ultra-non-relativistically in the early universe, rendering it cold. *Warm* dark matter candidates with keV-scale masses have been suggested to explain the subhalo structures at the scale of dSph galaxies (as has already been discussed). However, *hot* dark matter, which decouples at relativistic speeds, is strongly-constrained and cannot make up more than around 1% of the total dark matter component [71, 72].

1.2.2 Relic density

In order to account for the dark matter in the universe, a good candidate must be produced in the early universe with sufficient abundance to match the currently observed value $\Omega_c h^2 = 0.1196 \pm 0.0031$ (see Table 1.1). If produced with a smaller abundance, the candidate cannot account for the entirety of the universe's dark matter (though it could still contribute, along with other candidates, as in Ref. [73]). If on the other hand, it is produced with too great an abundance, it could threaten to exceed the DM density constraint set by Planck and overclose the universe.

The standard scenario for the production of dark matter is referred to as thermal freeze-out [4]. In this scenario, DM particles remain in kinetic and chemical equilibrium with SM particles in the very early universe by scattering and annihilation processes. Their number density n follows a

Maxwell-Boltzmann distribution

$$n \sim (m/T)^{3/2} \exp(-m/T), \quad (1.2)$$

for a mass m and temperature T . As the universe expands, however, the particles become diluted, reducing the interaction rate until eventually the DM particles become decoupled from the SM particles and are ‘frozen-out.’ They are then left with the abundance they had when they decoupled, which is further diluted by the expansion of the universe to become the abundance we see today. The exact relic abundance depends on $\langle\sigma_{\text{ann}}v\rangle$, the average annihilation cross section of the DM particles (weighted by the DM speed). If this is small, DM will decouple early when the temperature of the universe is still high, leading to a large relic abundance. If the annihilation cross section is large, DM will remain in equilibrium for longer, even as the particles become more and more diluted. The DM then freezes out later, with a lower temperature and lower relic abundance. The resulting relic abundance for GeV-scale DM is given approximately by:

$$\Omega_c h^2 \approx \frac{3 \times 10^{-27} \text{ cm}^3 \text{ s}^{-1}}{\langle\sigma_{\text{ann}}v\rangle}, \quad (1.3)$$

leading to a canonical value of around $\langle\sigma_{\text{ann}}v\rangle \approx 3 \times 10^{-26} \text{ cm}^3 \text{ s}^{-1}$ for the annihilation cross section. This coincides well with the value expected for particles with weak-scale interactions (so-called weakly interacting massive particles, or WIMPs), leading some to refer to this argument as the WIMP miracle. In reality, the full differential equations describing the DM number density must be solved [74], accounting for co-annihilations [75], which may boost the total cross section. However, the simplicity of this scenario make cold thermal relics an attractive candidate for DM.

Dark matter may also achieve the correct relic abundance through a variety of other mechanisms. ‘Freeze-in’ [76] involves particles which interact so weakly (termed feebly interacting massive particles, FIMPs) that they never reach equilibrium. Instead, a relic population is built up gradually through the production of FIMPs by annihilation of SM particles. In contrast to the freeze-out scenario, the relic abundance of FIMPs increases with increasing annihilation cross section. Dark matter may also be produced gravitationally from vacuum fluctuations during and after inflation [77, 78] or from the decays of heavier meta-stable particles (e.g. Ref. [79]). These possibilities open up the range of candidates which may

be considered to include much lighter or much heavier particles than the freeze-out scenario alone might allow.

1.2.3 Primordial nucleosynthesis

Primordial nucleosynthesis (or Big Bang Nucleosynthesis, BBN) describes the production of light nuclei in the first few minutes after the big bang. By solving a set of coupled Boltzmann equations describing the nuclear reactions of protons, neutrons and light nuclei, we can obtain the primordial abundances of these light nuclei and compare with the inferred values [80]. Significantly, these abundances depend strongly on the baryon-photon ratio η and therefore the total baryon density. Fits to data lead to the result $\Omega_b h^2 = 0.017 - 0.024$ [81], independent of the value obtained from CMB measurements (Table 1.1). Thus, the baryonic matter can make up only a fraction of the total matter density of the universe. We are led to conclude that particle dark matter must consist of some non-baryonic particle.

The results of BBN are also very sensitive to light new species, which can alter the number of relativistic degrees of freedom in the early universe and therefore affect the expansion rate. These include, for example, gravitinos [82] and right-handed neutrinos [83]. BBN therefore provides strong constraints on the parameters of such models. In addition, the decay of dark matter particles into electromagnetic or hadronic showers during nucleosynthesis can drastically change the primordial abundances of the light elements. BBN can therefore be used to constrain models in which dark matter undergoes early decays (or in which dark matter is produced by the decays of heavier particles) [84].

1.3 Particle dark matter candidates

While *valid* DM candidates need only satisfy the conditions and constraints which have already been discussed, *well-motivated* candidates should derive sensibly from some physical model. In fact, dark matter candidates can be found in a wide range of models of particle physics beyond the standard model. As has already been discussed, massive particles with GeV-scale masses and weak-scale interactions are attractive for obtaining the correct DM relic density. Such a WIMP candidate may be provided by the lightest supersymmetric particle (LSP) in supersymmetric theories

[85]. In supersymmetry, each of the known SM particles has a supersymmetric partner (or ‘spartner’), with bosons having fermionic partners and vice versa - this additional symmetry is often invoked to help alleviate the hierarchy problem [86]. In models which possess R-parity (which may be required to protect the proton from decay), particles carry R-parity 1 while supersymmetric particles (‘sparticles’) carry R-parity -1. This means that the lightest sparticle cannot decay into SM particles and is therefore stable, making it a promising DM candidate.

Depending on the parameters of the supersymmetric theory, there are many possibilities for which sparticle will be the LSP. One popular and well-studied possibility is the neutralino χ [87], which is a linear combination of the neutral supersymmetric partners of the W and B with the CP-even higgsinos. The properties of the neutralino can vary dramatically depending on the mixing between these different components and the underlying supersymmetric parameters [88]. In other cases, the LSP may be sneutrino [89], a partner of the standard model neutrino. Another alternative is the gravitino, in which case it may be produced gravitationally in the early universe with a mass greater than 10^{12} GeV, leading to the title ‘WIMPzilla’ [90].

WIMPs also arise in theories of universal extra dimensions, in which the additional dimensions are compactified, leading to a tower of excited states of the standard model particles [91]. These ‘Kaluza-Klein’ (KK) particles also possess a KK-parity, which means that the lightest KK particle (LKP) is stabilised [92]. One possibility for the LKP is the first excitation of the B weak hypercharge boson, $B^{(1)}$. In this case, the WIMP would be a spin-1 particle with a mass of around 1 TeV (in order to be produced thermally with the correct relic abundance) [93]. It has also been shown that the first KK excitations of the photon and neutrino are viable DM candidates if they also have masses at the TeV scale [94]. In contrast to the LSP, the LKP is described by a relatively small parameter space and may be more easily constrained by upcoming experiments [95].

In light of the problems with models of dark matter structure formation on small scales, there are several candidates which may be attractive for constituting warm dark matter. While standard neutrinos (with masses of a few eV [96]) cannot account for a large fraction of the dark matter, keV-scale sterile neutrinos may be viable [97]. Sterile neutrinos interact with ordinary matter via neutrino mixing rather than via electroweak in-

teractions. While attractive for providing warm dark matter, non-thermal production [98] or multiple sterile neutrinos species [99] may be required to avoid many astrophysical and cosmological constraints [100, 101].

Another non-WIMP candidate is the axion. The axion was originally introduced by Peccei and Quinn [102] to solve the strong CP problem. It was observed that this spin-zero particle should be produced in abundance in the early universe via the ‘misalignment mechanism’ and, for masses in the range $10^{-5} - 10^{-3}$ eV, can account for the cosmological dark matter [103]. It was recently noted that axion dark matter would thermalise and form a Bose-Einstein condensate, acting as cold dark matter at late times [104], as well as explaining anomalies in the alignment of CMB multipoles [105]. Also of interest are axion-like particles (ALPs), which emerge naturally in string theory and are expected to span many orders of magnitude in mass and coupling strength [106].

As is clear from this discussion, there are a wide range of well-motivated candidates for the dark matter in the universe. Some further examples include WIMPlless dark matter [107], mirror dark matter [108] and little Higgs dark matter [109], as well as minimal approaches to DM [110]. In this work, we focus on the WIMP, not only because of its popularity and generic nature, but because of the large number of experimental searches which provide sensitivity to WIMP dark matter.

The final condition appearing in the ‘10-point test’ of Taoso et al. asks the question ‘Can it be probed experimentally?’ While it may be possible that DM interacts only gravitationally, a wide variety of proposed candidates can interact (however weakly) with the particles of the standard model. While the experimental accessibility of a given DM candidate is not a strict necessity, it allows models to be tested (and either falsified or confirmed) beyond the hypothesis stage. In the next section, we explore the different avenues by which models of particle dark matter may be probed.

1.4 Detection of dark matter

Many of the candidates which have been discussed are expected to interact weakly with the particles of the Standard Model (SM). We note in particular that dark matter particles which are produced by thermal freeze-out in the early universe must have interactions with SM particles in order to maintain thermal and kinetic equilibrium. These interactions are medi-

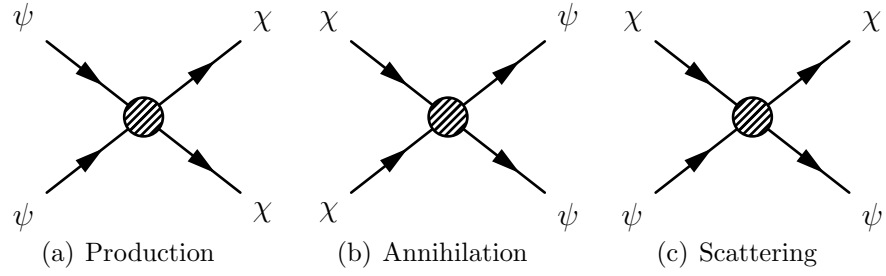


Figure 1.3: Schematic interactions between dark matter particles χ and standard model particles ψ .

ated by Feynman diagrams which can be represented (schematically) as in Fig. 1.3. The existence of production, annihilation and scattering processes between DM and SM particles provides a window into the possible detection of particle DM. Each of these processes leads to a distinct detection strategy, referred to as collider, indirect and direction detection.

1.4.1 Collider production

Searches for dark matter at the particle colliders such as the LHC rely on processes such as Fig. 1.3(a), in which SM particles annihilate to produce dark matter particles. However, the weak interactions of the DM means that once produced, it will escape the detectors around the interaction point without being observed. Thus, collider searches for dark matter must look for other signatures.

One approach is to look for signatures which are characteristic of a particular theory. For example, looking for evidence of KK states which are expected in theories of universal extra dimensions [111, 112], or searching for particle signatures from decay chains which are expected from supersymmetry [113, 114]. While this allows constraints to be placed on specific models, the range of models may be large, meaning that each must be constrained separately.

An alternative approach is to look for deviations from the SM expectation and use this to place limits on the operators of an effective field theory (see e.g. [115]). One possible signature is to look for the pair production of DM states, with initial state radiation of a SM particle. It is then possible to search for this initial state radiation (which may be a single jet or a single boson or lepton, depending on which particle was radiated). By combining all the possibilities for the form of the initial state radiation, we can place bounds on the effective operators which govern SM-DM interactions [116].

Mention actual numbers/results. It is also possible to look for more general missing energy signatures [117], in which energy is carried away by the dark matter particle produced.

One advantage of this effective operator approach is that these bounds can be translated into limits on signals at direct and indirect experiments, allowing collider results to be incorporated with other experimental searches in a complementary fashion [118]. However, it has been noted that caution must be exercised in naively applying the field theory approach at the LHC as well as in translating this to other search channels [119, 120].

So far, there has been no evidence observed for the production of dark matter particles at the LHC []. The non-observation of supersymmetry at the LHC has also begun to place some tension on SUSY dark matter models [121], though they are not yet excluded [122]. The proposed International Linear Collider (ILC) [123] should be able to explore more of the possible dark matter parameter space [124, 125]

1.4.2 Indirect detection

The possibility of dark matter annihilation into SM particles (as described in Fig. 1.3(b)) means that DM may be detected indirectly, by searching for these excess annihilation products (and related decay products). Some searches aim to look for the contribution of these products to signals obtained over large survey areas. The Fermi-LAT collaboration have published limits on searches for spectral lines and contributions to the diffuse background of gamma-rays [126]. Cosmic ray experiments such as PAMELA [127] have aimed to measure the p^\pm and e^\pm abundances in cosmic rays. The AMS experiment [128] has recently reported a rise in the cosmic ray positron fraction at energies above 10 GeV, which has been interpreted as tentative evidence for dark matter annihilations (see e.g. Ref. [129]). For charged cosmic rays, astrophysical magnetic fields deflect the paths of particles, meaning that it can be difficult to resolve individual sources [130].

In contrast, photon searches allow specific locations to be targeted. Because the signal rate is proportional to the DM annihilation rate (along the line of sight), the potential signal scales as the square of the dark matter density. Thus, searching in areas where the DM density is expected to be high can boost the signal rate significantly [131]. As has already

been discussed, dSph galaxies are dark matter dominated objects and thus represent promising targets for indirect searches. A survey of 25 Milky Way satellite galaxies by the Fermi-LAT telescope [132] has so far found no significant gamma-ray signal. However, upper limits on the annihilation cross section are in some cases close to the thermal freeze-out value of $\langle\sigma_{\text{ann}}v\rangle \approx 3 \times 10^{-26} \text{ cm}^3 \text{ s}^{-1}$, depending on the WIMP mass and annihilation channel. By optimising search regions near the centre of the Milky Way for maximum signal-to-noise, Weniger recently found a bump in the gamma-ray spectrum of Fermi-LAT data around 130 GeV [133]. However, subsequent analysis has found that this feature may be a systematic effect in the detector [134] and that it is difficult to reconcile with conventional models for dark matter [135, 136].

Perhaps more promising is a different gamma ray signal coming from the inner regions of the Galaxy, peaking at energies around 1-3 GeV [137, 138]. Fits of the data point towards a dark matter particle with a mass of 31-40 GeV, annihilating predominantly to $b\bar{b}$ with a cross section of $\langle\sigma v\rangle = (1.4 - 2.0) \times 10^{-26} \text{ cm}^3 \text{ s}^{-1}$, approximately matching the value required for a particle created by thermal freeze-out in the early universe. While it has been suggested that this signal is actually consistent with known sources [139] or as yet unresolved astrophysical sources [140], further analysis has shown that the signal matches the spectrum and morphology expected from DM annihilation [141]. Confirmation of the signal may have to wait until it is corroborated by independent observations, for example a DM annihilation signal from dSph galaxies.

The sensitivity of gamma ray searches can be extended up to TeV-scale masses with ground-based Imaging Atmospheric Cherenkov Telescopes (IACTs). These work by imaging the Cherenkov radiation from charged particles produced when high energy gamma rays impinge on the atmosphere. The current generation of IACTs - HESS [142], MAGIC [143] and VERITAS [144] - have been used to conduct searches for line-like gamma ray spectra as well as searches for signals from dwarf galaxies. However, these limits are typically around two orders of magnitude above the thermal cross section. The planned Cherenkov Telescope Array (CTA) may be able to probe down to this thermal cross section for high WIMP masses [145].

Another potentially rich source of DM annihilations are the Sun and Earth. DM particles may scatter with nuclei in these bodies, losing energy

and eventually becoming captured. Eventually, the DM sinks to the centre of the object and annihilates. The only annihilation products which can escape are neutrinos, which can then be detected at neutrino telescopes such as ANTARES [146] and IceCube [147]. Because the neutrino flux depends on the scattering rate of DM with nuclei, such signals can probe similar (but complementary) parameter spaces to direct detection experiments. We treat this subject in more detail in Chapter ??.

1.4.3 Direct detection

Processes described by the diagram in Fig. 1.3(c) lead to the possibility of scattering between DM and SM particles. The principle of direct detection is to look for nuclear recoils due to this scattering in a dedicated detector [148, 149]. WIMPs with GeV-scale masses and speeds $v \sim 10^{-3}c$ are expected to produce keV-scale nuclear recoils. In addition, due to the expected low cross section for such interactions, the predicted rate is less than around 1 event per year per kg of detector mass. Detecting such rare, low energy recoils requires not only large ton-scale detectors, but also sophisticated methods for discriminating signal from background.

Several direct detection experiments have claimed a tentative signal, such as DAMA/LIBRA [150], CoGeNT [151, 152] and CRESST-II [153]. However, these are in tension with null results from other experiments such as the recent LUX report [154]. Due to a range of uncertainties in nuclear physics, particle physics and astrophysics it may be possible to reconcile these results. In any case, a firm understanding of these uncertainties will be necessary to build a coherent picture from future results. The interpretation of direct detection data will be the main focus of this work and the main subject of Chapter 2.

1.4.4 Conclusions

The Λ CDM paradigm has enjoyed great success in explaining observations from galactic to cosmological scales. While discrepancies with observations on smaller scales remain, these are being actively pursued and may prove to be valuable testing grounds for the process of dark matter structure formation.

The identity of dark matter is unknown and cannot be accounted for by any of the known standard model particles. Even so, we know that

it must be neutral, long-lived and cold (or possibly warm) and that it must pass a variety of stringent tests coming from BBN and the CMB. There is no lack of well-motivated CDM candidates, including the lightest supersymmetric and Kaluza-Klein particles, sterile neutrinos, axions and many more. We have focussed on the search for weakly interacting massive particles (WIMPs) and described how direct, indirect and collider searches have been used to place limits on the WIMP parameters and soon hope to make the first non-gravitational detection of DM.

Chapter 2

Direct detection of dark matter

2.1 Introduction

The idea that particle dark matter (DM) may be observed in terrestrial detectors was first proposed by Goodman and Witten in 1985 [148] and by Drukier, Freese and Spergel in 1986 [149]. If DM can interact with particles of the Standard Model, the flux of DM from the halo of the Milky Way may be large enough to cause measureable scattering from nuclei. If the subsequent recoils can be detected and their energy spectrum measured, it should be possible to infer some properties of the DM particles.

However, the expected event rate for keV-scale recoils at such a detector would be of the order of 10^{-10} events per kg of detector material per day per keV recoil energy [155]. With such a low event rate, it is imperative that backgrounds can be reduced as much as possible. In addition, detectors should be as large as possible and sensitive to as wide a range of recoil energies as possible, in order to maximise the total number of events observed. Thus, specialised detectors are required to shield the active detector material from backgrounds and to discriminate between these backgrounds and signal events.

There exist at present a wide range of detectors using a variety of different sophisticated techniques for detecting such a weak signal against ubiquitous backgrounds, each probing a slightly different range of DM parameter space. Several of these experiments - such as DAMA/LIBRA [150], CoGeNT [151, 152] and CRESST-II [153] - claim to have observed a signal

indicative of a WIMP with mass ~ 10 GeV. However, a number of other experiments have reported null results creating tension for a dark matter interpretation of these tentative signals. It remains to be seen whether this discrepancy is an experimental effect or a hint of new physics.

There remain a number of uncertainties in the direct detection of dark matter. These come from a variety of sources and can be approximately partitioned into experimental, nuclear, particle and astrophysical uncertainties. Understanding these uncertainties is imperative for properly interpreting the results of direct detection experiments and understanding whether a coherent picture can emerge from a number of different experimental efforts.

In this chapter, I will review the formalism for direct detection which was introduced by Goodman, Witten, Drukier, Freese and Spergel in the 1980s (and subsequently refined). I will then briefly discuss some of the experimental techniques which are used to achieve the required sensitivity for DM searches, as well as summarising current experimental constraints and results. I will also outline some of the uncertainties which afflict the interpretation of direct detection data.

I will focus on astrophysical uncertainties in direct detection. In particular, I will discuss how the local density and distribution of dark matter impacts the direct detection event rate, how well we understand these different factors and review approaches which have been developed in the past to mitigate these uncertainties.

2.2 Direct detection formalism

We wish to obtain the rate of nuclear recoils per unit detector mass due to elastic, non-relativistic scattering from a fermionic weakly interacting massive particle (WIMP). Dark matter is typically assumed to be spin-1/2, though the analysis here can be generalised to particles of arbitrary spin [156]. The differential event rate R can be written straightforwardly as

$$\frac{dR}{dE_R} = N_T \Phi_\chi \frac{d\sigma}{dE_R}, \quad (2.1)$$

for recoils of energy E_R , N_T target particles, a DM flux of Φ_χ and a differential scattering cross section of $d\sigma/dE_R$. Per unit detector mass, the number

of target particles is simply $N_T = 1/m_N$, for nuclei of mass m_N . The DM flux for particles with speed in the range $v \rightarrow v + dv$ in the laboratory frame is $\Phi_\chi = n_\chi v f_1(v) dv$. Here, n_χ is the number density of dark matter particles χ and $f_1(v)$ is the speed distribution for the dark matter. The periodic motion of the Earth means that its velocity is time-varying, producing an annual modulation in $f_1(v)$ and therefore in the direct detection event rate [157]. However, this modulation is expected to be a percent-level effect and we consider here only the time averaged distribution.

We can convert from the number density to the mass density ρ_0 by dividing by DM particle mass m_χ : $n_\chi = \rho_0/m_\chi$. By integrating over all DM speeds, we therefore obtain

$$\frac{dR}{dE_R} = \frac{\rho_0}{m_N m_\chi} \int_{v_{\min}}^{\infty} v f_1(v) \frac{d\sigma}{dE_R} dv, \quad (2.2)$$

where v_{\min} is the minimum speed required to excite a nuclear recoil of energy E_R :

$$v_{\min} = \sqrt{\frac{m_N E_R}{2\mu_{\chi N}^2}}. \quad (2.3)$$

The differential scattering cross section per solid angle in the zero-momentum frame (ZMF), Ω^* , is given by:

$$\frac{d\sigma}{d\Omega^*} = \frac{1}{64\pi^2 s} \frac{p_f^*}{p_i^*} |\mathcal{M}|^2, \quad (2.4)$$

where \mathcal{M} is the scattering amplitude obtained from the Lagrangian. For elastic scattering, the final and initial momenta in the ZMF are equal: $p_f^* = p_i^*$. The centre-of-mass energy squared, s , can be written $s \approx (m_\chi + m_N)^2$, where we have used the non-relativistic approximation. The recoil energy can be written in terms of the ZMF scattering angle θ^* as [155]

$$E_R = \frac{\mu_{\chi N}^2 v^2}{m_N} (1 - \cos \theta^*). \quad (2.5)$$

Noting that $d\Omega^* = d\cos \theta^* d\phi$, we can write:

$$\frac{dE_R}{d\Omega^*} = \frac{\mu_{\chi N}^2 v^2}{2\pi m_N}, \quad (2.6)$$

and therefore

$$\frac{d\sigma}{dE_R} = \frac{1}{32\pi m_N m_\chi^2 v^2} |\mathcal{M}|^2. \quad (2.7)$$

The matrix element \mathcal{M} is obtained from interaction terms in the lagrangian between the DM particle and quarks. This will depend on the particular DM model under consideration and the full form of these interaction terms is not known. It is typically assumed that these terms can be adequately described by a contact interaction, an implied assumption that the particles mediating the interaction are much more massive than the momentum transferred [158]. The momentum transfer in direct detection experiments is typically less than ~ 200 MeV, suggesting that this assumption should be a valid one. However, we will consider briefly scenarios where this is not the case in Sec. 2.4.2.

Because the WIMPs have speeds of order $10^{-3}c$, the scattering occurs in the non-relativistic limit, leading to some important simplifications. In this limit, the axial-vector interaction simply couples the spins of the WIMP and quark. The scalar interaction induces a coupling of the WIMP to the number of nucleons in the nucleus, with the vector¹ and tensor interactions assuming the same form as the scalar in the non-relativistic limit [85]. All other interactions are typically suppressed by powers of v/c and so will be subdominant. Generically, then, the cross section is typically written in terms of spin-independent (SI) and spin-dependent (SD) interactions [148]

$$\frac{d\sigma}{dE_R} = \frac{d\sigma_{SI}}{dE_R} + \frac{d\sigma_{SD}}{dE_R}. \quad (2.8)$$

We now discuss the form of the SI and SD cross sections in turn.

2.2.1 SI interactions

Spin-independent interactions are generated predominantly by scalar terms in the effective lagrangian

$$\mathcal{L} \supset \alpha_S^{(q)} \bar{\chi} \chi \bar{q} q, \quad (2.9)$$

for interactions with a quark species q with coupling $\alpha_S^{(q)}$. The operator $\bar{q}q$ is simply the quark number operator, which couples to the quark density. However, we should recall that the quarks are in nucleon bound states. We consider first the contributions from neutrons $|n\rangle$, so we should evaluate $\langle n | \bar{q}q | n \rangle$, adding coherently the contributions from both valence and sea

¹For the case of a Majorana fermion, the vector current vanishes and we need not consider it.

quarks. These matrix elements are obtained from chiral perturbation theory [159] or Lattice QCD [160]. These matrix elements can be parametrised in terms of their contribution to the nucleon mass in the form:

$$m_n f_{Tq}^n \equiv \langle n | m_q \bar{q}q | n \rangle. \quad (2.10)$$

Adding the contributions of the light quarks, as well as the heavy quarks and gluons (which contribute through the chiral anomaly [161]), we obtain

$$\langle n | \sum_{q,Q,g} \bar{q}q | n \rangle = \left(\sum_{q=u,d,s} \frac{m_n}{m_q} f_{Tq}^n \alpha_S^q + \frac{2}{27} f_{TQ}^n \sum_{q=c,b,t} \frac{m_n}{m_q} \alpha_S^q \right) \equiv f^n. \quad (2.11)$$

The parameters describing the contributions of the different quarks to the nucleon mass must be determined experimentally. The uncertainties this produces will be discussed shortly in Sec. 2.4.1. *Need to double check this expression and exactly what it's equal to...*

We now consider the matrix elements of the nucleon operators within a nuclear state, $|\Psi_N\rangle: \langle \Psi_N | f^n \bar{n}n | \Psi_N \rangle$. These operators now simply count the number of n nucleons in the nucleus, along with a momentum-dependent form factor, $F(\mathbf{q})$, corresponding to the Fourier transform of the nucleon density. This takes into account the loss of coherence for nuclear scattering due to the fact that the nucleus is not point-like. We therefore obtain:

$$\langle \Psi_N | f^n \bar{n}n | \Psi_N \rangle = \langle \Psi_N | \Psi_N \rangle f^n N_n F_n(\mathbf{q}) = 2m_N f^n N_n F_n(\mathbf{q}), \quad (2.12)$$

where we note that we require the wavefunctions to be normalised to $2E \approx 2m_N$ for a nucleus of mass m_N . We now add the contribution from protons to the matrix element, noting that $F_n \approx F_p = F$ (see Sec. 2.4.1)

$$\langle \Psi_N | f^n \bar{n}n + f^p \bar{p}p | \Psi_N \rangle = 2m_N (f^n N_n + f^p N_p) F(\mathbf{q}), \quad (2.13)$$

where N_n and N_p are the neutron and proton numbers of the nucleus respectively.

The corresponding matrix element for the scalar WIMP operator $\bar{\chi}\chi$ is simple in the non-relativistic limit, evaluating to $2m_\chi$ []. Combining these, we obtain the scalar matrix element

$$|\mathcal{M}_S|^2 = 16m_\chi^2 m_N^2 |f^p Z + f^n (A - Z)|^2 F_{SI}^2(\mathbf{q}), \quad (2.14)$$

and the SI cross section

$$\frac{d\sigma_{SI}}{dE_R} = \frac{m_N}{2\pi v^2} |f^p Z + f^n (A - Z)|^2 F^2(\mathbf{q}), \quad (2.15)$$

where we have used the atomic number Z and mass number A to describe the composition of the nucleus. It is conventional to write this in terms of the WIMP-proton SI cross section, which does not depend on the particular (A, Z) of the target nucleus and thus allows easy comparison between experiments. This cross section is given by

$$\sigma_{SI}^p = \frac{\mu_{\chi p}^2}{\pi} (f^p)^2, \quad (2.16)$$

meaning that

$$\frac{d\sigma_{SI}}{dE_R} = \frac{m_N}{2\mu_{\chi p}^2 v^2} |Z + (f^n/f^p)(A - Z)|^2 F^2(E_R). \quad (2.17)$$

2.2.2 SD interactions

The spin-dependent interaction is typically sourced by axial-vector currents of the form

$$\mathcal{L} \supset \alpha_{AV}^{(q)} (\bar{\chi} \gamma^\mu \gamma_5 \chi) (\bar{q} \gamma_\mu \gamma_5 q). \quad (2.18)$$

These result in a coupling of the spins of the WIMP and nucleus. In analogy with the SI case, we can write the neutron quark matrix elements in the form [162, 163]

$$\langle n | \bar{q} \gamma_\mu \gamma_5 q | n \rangle = 2s_\mu^n \Delta_q^n, \quad (2.19)$$

where s_μ is the spin 4-vector and Δ_q parametrises the contribution of quark q to this total spin. Adding the contributions of the different quarks, we can define

$$a_{p,n} = \sum_{q=u,d,s} \frac{\alpha_{AV}^{(q)}}{\sqrt{2}G_F} \Delta_q^{p,n}, \quad (2.20)$$

which are the effective proton and neutron spin couplings.

The full nuclear matrix elements can then be written in the form [Check this expression...](#)

$$\langle \Psi_N | \sum_{q=u,d,s} \bar{q} \gamma_\mu \gamma_5 q | \Psi_N \rangle = 2\sqrt{2}G_F \frac{a_p \langle S_p \rangle + a_n \langle S_N \rangle}{J} \langle \Psi_N | \hat{J} | \Psi_N \rangle F_{SD}^2(E_R) \quad (2.21)$$

where J is the total nuclear spin, $\langle S_{p,n} \rangle$ the expectation value of the total proton and neutron spin in the nucleus and F_{SD}^2 is a form factor, as in the SI case, which is determined by the internal spin structure of the nucleus. Noting that $\langle \Psi_N | \hat{J} | \Psi_N \rangle = 2J(J+1)m_N$, we obtain for the SD cross section

$$\frac{d\sigma_{SD}}{dE_R} = \frac{4m_N}{\pi v^2} G_F^2 \frac{J+1}{J} |a_p \langle S_p \rangle + a_n \langle S_n \rangle|^2 F_{SD}^2(E_R). \quad (2.22)$$

Again, as in the SI case, it is convenient to rewrite this expression in terms of the proton cross section σ_{SD}^p , which is given by

$$\sigma_{SD}^p = \frac{6G_F^2}{\pi} \mu_{\chi p}^2 (a_p)^2. \quad (2.23)$$

This leads to the final expression for the SD cross section

$$\frac{d\sigma_{SD}}{dE_R} = \frac{2m_N \sigma_{SD}^p}{3\mu_{\chi p}^2 v^2} \frac{J+1}{J} |\langle S_p \rangle + (a_n/a_p) \langle S_n \rangle|^2 F_{SD}^2(E_R). \quad (2.24)$$

2.2.3 The final event rate

It is helpful to collect these various results together to form a coherent picture of the event rate. Combining the SI and SD rates together, we can write

$$\frac{d\sigma}{dE_R} = \frac{m_N}{2\mu_{\chi p}^2 v^2} (\sigma_{SI}^p \mathcal{C}_{SI} F_{SI}^2(E_R) + \sigma_{SD}^p \mathcal{C}_{SD} F_{SD}^2(E_R)), \quad (2.25)$$

where the proton cross sections $\sigma_{SI,SD}^p$ were defined in the previous section, the form factors $F_{SI,SD}^2$ will be discussed in more detail in Sec. 2.4.1 and we have defined the enhancement factors as

$$\mathcal{C}_{SI} = |Z + (f^n/f^p)(A - Z)|^2 \quad (2.26)$$

$$\mathcal{C}_{SD} = \frac{4}{3} \frac{J+1}{J} |\langle S_p \rangle + (a_n/a_p) \langle S_n \rangle|^2. \quad (2.27)$$

We can now incorporate these into the full event rate:

$$\frac{dR}{dE_R} = \frac{\rho_0}{2\mu_{\chi p}^2 m_\chi} (\sigma_{SI}^p \mathcal{C}_{SI} F_{SI}^2(E_R) + \sigma_{SD}^p \mathcal{C}_{SD} F_{SD}^2(E_R)) \int_{v_{\min}}^{\infty} \frac{f_1(v)}{v} dv. \quad (2.28)$$

The shape of the different event rate then depends on a range of factor: the DM and target nuclear masses, the ratios of the proton and neutron couplings and the shape of the speed distribution $f_1(v)$. This distribution is typically assumed to have a simple form, the so-called Standard Halo Model (SHM), which we discuss in detail in Sec. 2.4.3. We show in Fig. 2.1 the SI differential event rate for Xenon (solid blue), Germanium (dashed green) and Argon (dot-dashed red) targets and several WIMP masses, assuming equal couplings to protons and neutrons.

As we increase the mass of the target nucleus, we see an increase in the low energy event rate. This is a result of the A^2 enhancement for SI interactions, resulting in the Xenon ($A \approx 131$) spectrum being a factor of around 10 higher than the Argon ($A \approx 40$) spectrum at low energies. As we consider higher energies, however, we observe that the spectrum for heavier targets decays more quickly, resulting in a much steeper spectrum. This is due to a more sharply falling form factor; the larger size of the nucleus results in a more rapid loss of coherence as the recoil energy is increased.

As we increase the WIMP mass, the recoil spectrum becomes flatter. This is primarily due to the dependence of v_{\min} on m_χ (shown in Eq. 2.3). As we increase m_χ , the reduced mass $\mu_{\chi N}$ increases, meaning that v_{\min} varies more slowly with energy. This means that the integral over the speed distribution also varies more slowly with energy. Physically, low mass WIMPs require a larger speed to impart the same recoil energy and as we increase the recoil energy this required speed grows quickly. The rapid cut-off in the spectrum observed in the $m_\chi = 10$ GeV case (top panel of Fig. 2.1) occurs when there are no more WIMPs below the galactic escape velocity which have sufficient speed to produce recoils of the desired energy.

Here I might want to do a SI/SD comparison, say just a single plot comparing the shape of the SI and SD rates in Xenon for a given WIMP mass.

For a real experiment, the detector will be sensitive to recoil energies only in some range E_{\min} to E_{\max} . The total number of events expected is obtained by integrating over this range of recoil energies and multiplying by the exposure time t_{\exp} , detector mass m_{\det} and efficiency (which may also be a function of the recoil energy E_R) $\epsilon(E_R)$:

$$N_e = m_{\det} t_{\exp} \int_{E_{\min}}^{E_{\max}} \epsilon(E_R) \frac{dR}{dE_R} dE_R. \quad (2.29)$$

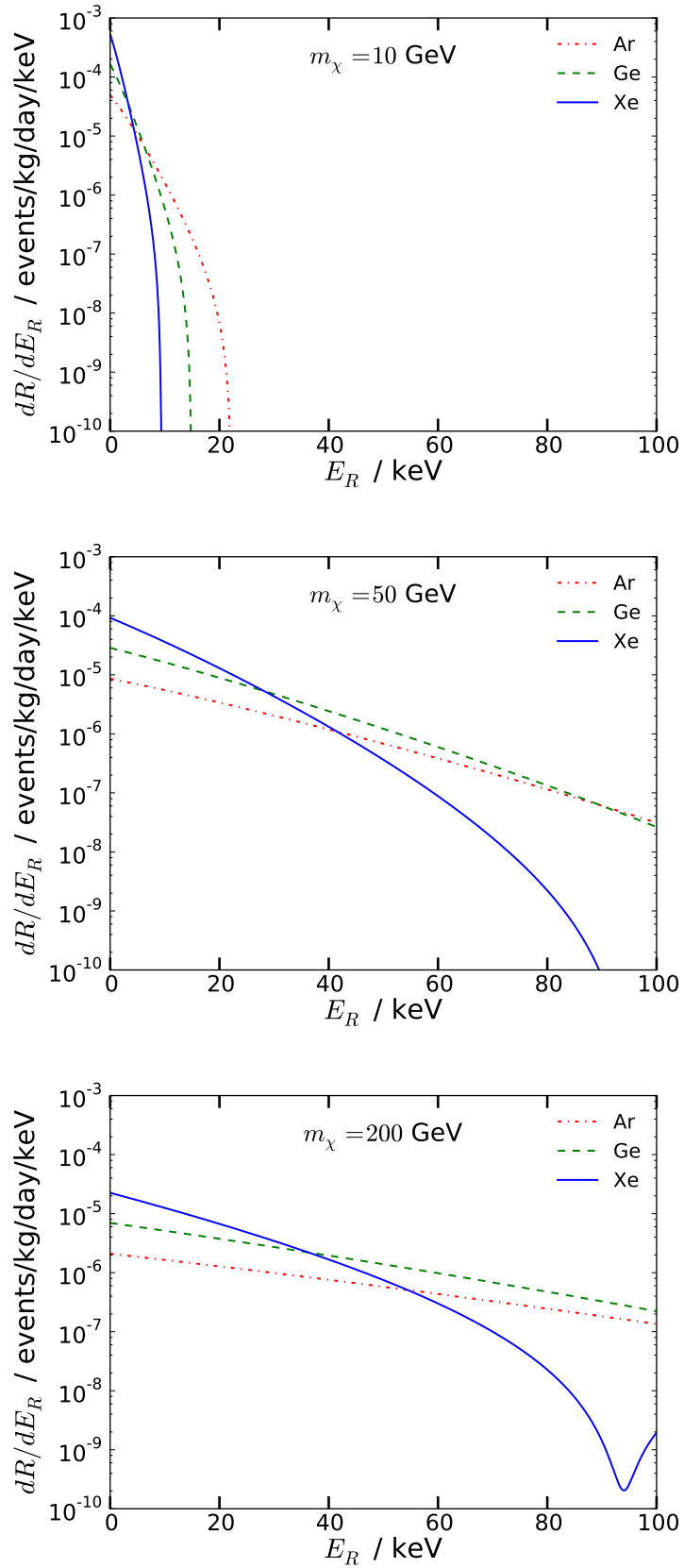


Figure 2.1: Spin-independent differential event rates predicted for the nuclear targets Xenon, Germanium and Argon and for several WIMP masses m_χ , assuming $f_p \approx f_n$. We assume a Standard Halo Model speed distribution, $\rho_0 = 0.3 \text{ GeV cm}^{-3}$ and a spin-independent cross section $\sigma_p^{\text{SI}} = 10^{-45} \text{ cm}^2$.

For the case of a more realistic experiment in which the measurement of energy has only a finite resolution $\sigma(E_R)$, we convolve the event rate with a resolution function to obtain the observed recoil spectrum $d\tilde{R}/dE_R$,

$$\frac{d\tilde{R}}{dE_R}(E) = \int_{E'=0}^{\infty} \frac{e^{-(E-E')^2/(2\sigma(E'))}}{\sqrt{2\pi}\sigma(E')} \frac{dR}{dE_R}(E') dE'. \quad (2.30)$$

We now turn our attention to the discussion of such ‘realistic experiments’ and the current state of dark matter direct searches.

2.3 Direct detection experiments

In order to measure the event spectrum, a range of obstacles must be overcome. One possible source of backgrounds are high energy cosmic rays. For this reason, direct detection experiments are typically operated underground, such as at the Gran Sasso laboratory in Italy or the Boulby laboratory in the UK, in order to reduce the penetration of these cosmic rays. However, cosmogenic muons and neutrons can still penetrate the experiments, leading to the need for active shields which can detect these particles and provide a veto for any nuclear recoils they produce. It is also possible to veto events which produce multiple-scatters in the detector as WIMPs are expected to scatter only once. Passive shielding also reduces the neutron flux from surrounding rock and other sources. For a detailed analysis of neutron sources at dark matter experiments, see Ref. [164] (CRESST-II) and Ref. [165] (XENON100).

Radioactive decays due to naturally occurring isotopes may cause keV energy nuclear recoils in the detector, meaning that care must be taken to reduce their impact. The radiopurity of the target material is therefore of utmost importance (see for example Ref. [166]), as well as the radiopurity of detector equipment itself [167, 168]. In some cases, the naturally occurring target material is contaminated with a particular radioisotope, such as ^{39}Ar contamination in Argon. In these cases, special sources of the material must be found [169], or the amount of contamination must be carefully monitored and reduced [170, 171].

A major source of backgrounds is also electron recoils, which deposit energy in the detector and must be distinguished from nuclear recoils caused by WIMP interactions. Depending on the design of the detector, different methods are used to discriminate electron from nuclear recoils and to mea-

sure the recoil energy itself. We will now summarise some of the techniques which are used.

Which ones are sensitive to spin independent and spin dependent?

Cryogenic experiments, such as CDMS [172–174], CRESST [175], Co-GeNT [151, 152, 176–178] and EDELWEISS [179], use cryogenic crystals of materials such as Germanium or Silicon as target materials. When a WIMP recoils from a target nucleus a phonons are generated in the crystal along with an ionization signal. By summing the energy collected in these two channels (and accounting for any which may be incompletely collected), the total energy of the nuclear recoil can be obtained. The ratio of the total nuclear recoil energy and the ionization signal is referred to as the ‘ionisation yield’ and can be used to discriminate electron from nuclear recoils; electron recoils deposit more energy into ionisation. However, care must be taken to identify so-called ‘surface events’ - events occurring close to the detector surface which result in an incomplete collection of ionisation signal and can thus mimic a WIMP signal.

Noble liquid experiments use liquid (or two-phase) noble elements such as Xenon and Argon as target materials. Completed or operational Xenon detectors include ZEPLIN [180], XENON [181] and LUX [154]. In these detectors, Xenon recoils produce a scintillation signal (S1) which can be observed directly using photomultiplier tubes. Ionisation electrons are also produced, which drift in an applied magnetic field, producing an electroluminescence signal (S2) in the gas phase. The sum of these signals can be used to reconstruct the total recoil energy, while the ratio S1/S2 is used to discriminate electron from nuclear recoils. The two signals can also be used to localise the event within the detectors. A fiducial volume is then defined within the detector - only events inside this volume are considered in data analysis. This allows liquid Noble detectors to be self-shielding; the fiducial volume is shielded by the remaining detector volume. Experiments utilising Argon [182, 183] and Neon [184] are currently under development, using either the scintillation to ionisation signal as a discriminant or using timing of the scintillation signal (pulse shape discrimination).

Superheated liquid detectors such as COUPP [185], SIMPLE [186] and PICASSO [187] use a detector volume filled with droplets of superheated liquid such as C_4F_{10} . The deposition of kinetic energy by a WIMP will induce the nucleation of a bubble producing an acoustic signal which is detected by piezoelectric transducers. Energy deposition by other particles

such as muons and γ - and β -radiation typically occurs over longer length scales and thus does not register a signal. The temperature and pressure of the detector can be tuned to specify the threshold energy, the minimum energy which must be deposited before nucleation occurs. As such, superheated liquid detectors cannot measure the energy of specific events but rather the total event rate above the energy threshold. However, by ramping up the energy threshold, the recoil spectrum can effectively be measured. *More sensitive to SD and light WIMPs.*

Crystal scintillator experiments [188] such as DAMA/LIBRA [150, 189, 190] and KIMS [191] use crystals such as Thallium-doped Sodium Iodide (NaI(Tl)) as the detector material. When a nuclear recoil occurs with the nuclei in the crystal, scintillation occurs. The light is collected by photomultiplier tubes, with the total recoil energy being related to the amount of scintillation light produced. In the case of DAMA/LIBRA, electron-nuclear recoil discrimination is not employed. Instead, the experiment aims to observe the annual modulation of the signal which is expected due to the periodic motion of the Earth through the WIMP halo. In other cases, such as NAIAD [192], pulse shape discrimination has been used to distinguish nuclear and electronic recoils.

A final class of direct detection experiments are known as ‘directional’ direct detection experiments. These aim to measure not only the energy deposited by WIMP scattering events but also the direction of the nuclear recoils. It is hoped that a recoil spectrum peaked in the direction opposite to the Earth’s motion will provide strong evidence for a DM origin for the recoils. This requires the use of specialised gas time projection chambers (TPCs), which allow measurable track lengths from which the recoil direction can be determined. The directional detection of dark matter is the subject of Chapter ?? and we therefore defer a more detailed discussion until then.

Irreducible neutrinos backgrounds..?

2.3.1 Current limits and results

The first major dark matter detection to be reported was that of DAMA/NaI [193] and its successor DAMA/LIBRA. The experiments observed an annual modulation over 13 annual cycles, with a phase matching that expected from a dark matter signal. The detection of the annual modula-

tion has been reported at the 8.9σ confidence level over an energy range of 2-6 keV. The modulation signal was only found in single-hit events at low energies, again suggesting a dark matter origin for the signal. It has been suggested that the signal may be explained by a dark matter particle of mass $m_\chi \sim 10$ GeV and SI cross section $\sigma_{SI} \sim 10^{-41}$ cm² [194]. An annual modulation signal was also observed in the CoGeNT experiment [152, 177]. In this case too, the period and phase are consistent with expectations, though, in both cases the amplitude of the annual modulation is approximately 5 times larger than expected.

Excesses above the expected backgrounds have also been observed in a number of experiments. The CoGeNT experiment observed an exponentially rising excess of events at low energies, down to 0.5 keV_{ee}. A maximum likelihood analysis [178] pointed towards a 10 GeV WIMP interpretation, with a cross section of around $\sigma_{SI} \sim 5 \times 10^{-42}$ cm², though the significance of the ‘signal’ lies at only 2.9σ . CRESST-II [175] observe 67 events in the nuclear recoil signal region but expect a background of only one event due to leakage of electron recoils into this window. Taking into account other backgrounds, the CRESST-II collaboration estimate that 25-30 of these events may be due to a WIMP signal. A fit to the data produces two minima in the likelihood function: one at $m_\chi \approx 25$ GeV (in which scattering from Tungsten is appreciable) and another at $m_\chi \approx 12$ GeV (where Tungsten recoils lie below the energy threshold). In both cases, the fitted cross section is in the range $\sigma_{SI} \approx 10^{-42} - 5 \times 10^{-41}$ cm². Finally, a recent analysis of the Silicon detector data from CDMS-II [174] finds 3 events in the signal region. However, the very low expected backgrounds mean that this small number of events may be significant. The probability of the known backgrounds producing these three events has been calculated at 5.4% and a likelihood analysis shows consistency with WIMP with $m_\chi \approx 9$ GeV and $\sigma_{SI} \approx 2 \times 10^{-41}$ cm².

While it appears that a reasonably consistent picture of a low mass WIMP is emerging from several experiments [195], a large number of competing experiments have reported null results. Results from CDMS-II (Ge), XENON100, LUX, SuperCDMS [196] and others set upper limits on the standard WIMP cross section several orders of magnitude lower than the claimed signal. Several explanations for this discrepancy have been offered. One possibility is background contamination of the experiments claiming to have observed a signal [168]. Another possibility is that ion-channeling in

the detector crystals may affect the collected ionisation signal and therefore alter the signal [197]. The DAMA/LIBRA signal has also been attributed to an annually modulated muon signal [198, 199].

An alternative explanation is that the claimed signals *are* due to a dark matter particle, but that its properties are not as simple as in the canonical case, explaining why it has not been observed in all experiments. One possibility is that the astrophysical distribution of dark matter does not match the standard assumptions. We will discuss this astrophysical distribution in more detail shortly in Sec. ???. However, it appears that even with this additional freedom, the different results cannot be reconciled [200–203]. A number of particle physics models have also been considered to explain the results, including spin-dependent interactions [204], isospin violating dark matter (for which $f^p \neq f^n$) [205], inelastic dark matter [206] and mirror dark matter [207]. However, a consistent picture which reconciles all experimental datasets remains elusive [208].

We summarise some of the completed and current direct detection experiments in Table 2.1. The most stringent limits on the SI WIMP-proton cross section are set by LUX [154], who find a limit of $\sigma_{SI}^p \leq 7.6 \times 10^{-46} \text{ cm}^2$ at a mass of $m_\chi = 33 \text{ GeV}$. The best limit for the SD cross section is set by XENON100 [209]: $\sigma_{SD}^p \leq 3.5 \times 10^{-40} \text{ cm}^2$. The confirmation or falsification of the signals which have been claimed thus far may have to wait for the next generation of dark matter experiments, or for corroboration from collider or indirect searches.

Give some typical values for thresholds and efficiencies..?

2.3.2 Future experiments

Experiments which are planned or under construction typically aim to scale up the size of current detectors and reduce unwanted backgrounds (in order to increase the sensitivity to lower cross sections) or decrease the energy threshold (which increases sensitivity to lower masses). There are a number of ton scale detectors either in operation or planned, including LZ [211], XENON1T [212], EURECA [213, 214] and DARWIN [215]. With this next generation of detectors, the aim is to achieve sensitivity to the SI WIMP-proton cross section down to $\sigma_{SI}^p = 10^{-48} \text{ cm}^2$.

In addition, there have been a number of proposals for novel methods of directly detecting dark matter. These include using DNA-based detectors

Experiment	Target	Status
CDMS-II (Ge) [172, 173]	Ge	Null result
CDMS-II (Si) [174]	Si	Excess
SuperCDMS [196]	Ge	Null result
CoGeNT [151, 152, 176–178]	Ge	Excess & annual modulation
CRESST-II [175]	CaWO ₄	Excess
EDELWEISS-II [179]	Ge	Null result
ZEPLIN-III [180]	Xe	Null result
XENON100 [181, 210]	Xe	Null result
LUX [154]	Xe	Null result
PICASSO [187]	C ₄ F ₁₀	Null result
SIMPLE-II [186]	C ₂ ClF ₅	Null result
COUPP [185]	CF ₃ I	Null result
DAMA/LIBRA [150, 189, 190]	NaI(Tl)	Annual modulation
NAIAD [192]	NaI(Tl)	Null result
KIMS [191]	CsI(Tl)	Null result

Table 2.1: Summary of current and completed direct detection experiments.

to provide high spatial resolution [216], using nano-scale explosives [217] or charged-coupled devices [218] to achieve very low energy thresholds and using proton-beam experiments as a source for dark matter source for direct detection experiments [219].

2.4 Uncertainties

Calculation of the DM differential event rate dR/dE_R requires not only a knowledge the dark matter parameters m_χ and $\sigma_{SI,SD}$ but a number of other factors which also enter into the calculation. It is important to understand how uncertainties in these different factors and parameters propagates into the event rate in order to ensure that the conclusions we draw from direct detection experiments are unbiased. These uncertainties are typically partitioned into three separate classes: nuclear physics, particle physics and astrophysics.

2.4.1 Nuclear physics uncertainties

It's possible that I keep using n to mean both 'neutron' and 'nucleon'...I'll try and fix that... As we have already seen, nuclear physics enters into

the calculation of the nucleon matrix elements $m_n f_{T_q}^n \equiv \langle n | m_q \bar{q} q | n \rangle$. The factors $f_{T_q}^n$ must be determined experimentally, having values

$$f_{Tu}^p = 0.020 \pm 0.004; f_{Td}^p = 0.026 \pm 0.005; f_{Ts}^p = 0.118 \pm 0.062, \quad (2.31)$$

with $f_{Tu}^p = f_{Td}^n$, $f_{Td}^p = f_{Tu}^n$ and $f_{Ts}^p = f_{Ts}^n$. The main uncertainties stem from determinations of the π -nucleon sigma term, determined either experimentally from low energy pion-nucleon scattering [159, 220, 221] or from lattice QCD calculations [160, 222]. Similarly for the spin contributions Δ_q to the nucleus, values must be obtained experimentally [163, 223–225],

$$\Delta_u^p = 0.77 \pm 0.08; \Delta_d^p = -0.38 \pm 0.08; \Delta_s^p = -0.09 \pm 0.08, \quad (2.32)$$

although efforts are being made to obtain these values directly via calculation [226, 227]. It should be noted that these nucleon matrix elements are only necessary if we wish to deal directly with quark-level couplings and interactions. If, instead, we consider the nucleon-level effective operators (and equivalently the WIMP-nucleon cross sections), these values are not required.

Nuclear physics also enters into the calculation of form factors, describing the internal nucleon and spin structures of the nuclei. For the SI case, the form factor is obtained from the Fourier transform of the nucleon distribution in the nucleus. The form typically used is due to Helm [228]

$$F_{SI}^2(E_R) = \left(\frac{3j_1(qR_1)}{qR_1} \right)^2 e^{-q^2 s^2}, \quad (2.33)$$

where $j_1(x)$ is a spherical bessel function of the first kind,

$$j_1(x) = \frac{\sin x}{x^2} - \frac{\cos x}{x}. \quad (2.34)$$

Typically used are nuclear parameters due to Lewin and Smith [229], based on fits to muon spectroscopy data [230]:

$$R_1 = \sqrt{c^2 + \frac{7}{3}\pi^2 a^2 - 5s^2} \quad (2.35)$$

$$c = 1.23A^{1/3} - 0.60\text{fm} \quad (2.36)$$

$$a = 0.52\text{fm} \quad (2.37)$$

$$s = 0.9\text{fm}. \quad (2.38)$$

Muon spectroscopy and electron scattering data [231] are typically used as a probe of the *charge* distribution in the nucleus. However, detailed Hartree-Fock calculations indicate that the charge distribution can be used as a good proxy for the nucleon distribution (especially in the case $f_p \approx f_n$) and that using the approximate Helm form factor introduces an error of less than $\sim 5\%$ in the total event rate [232]. Studies also indicate that errors due to distortions in nuclear shape away from sphericity are negligible [233].

In the SD case, however, the situation is more complicated. In order to calculate the SD cross section, we require the proton and neutron spin content $\langle S_{p,n} \rangle$ as well as the form factor F_{SD}^2 . The form factor can be written in the form

$$F_{SD}^2(E_R) = S(E_R)/S(0), \quad (2.39)$$

in terms of the response function $S(E_R)$. This response function can in turn be decomposed into three spin-dependent structure functions (SDSFs)

$$S(E_R) = a_0^2 S_{00}(E_R) + a_0 a_1 S_{01}(E_R) + a_1^2 S_{11}(E_R), \quad (2.40)$$

where $a_0 = a_p + a_n$ is the isoscalar coupling and $a_1 = a_p - a_n$ is the isovector coupling. The zero momentum transfer value $S(0)$ is related to the proton and neutron spin expectation values by [234]

$$S(0) = \frac{2J+1}{\pi} \frac{J+1}{J} |a_p \langle S_p \rangle + a_n \langle S_n \rangle|^2. \quad (2.41)$$

We can therefore rearrange the SD cross section of Eq. 2.24 as

$$\frac{d\sigma_{SD}}{dE_R} = \frac{2\pi}{3} \frac{m_N \sigma_{SD}^p}{\mu_{\chi p}^2 v^2} \frac{1}{2J+1} \frac{S(E_R)}{(a_p)^2}. \quad (2.42)$$

The nuclear physics is now encapsulated in a single response function $S(E_R)$ (or equivalently two SDSFs S_{00} and S_{11}).²

The functional form for S_{ij} can be calculated from shell models for the nucleus [235]. However, there are a number of competing models (such as the Odd Group Model [236], Interacting Boson Fermion Model [237] and Independent Single Particle Shell Model [238] among others). These models use different methods for accounting for forces between quarks, leading to different forms for the SDSFs and therefore to significant uncertainty in

²In Ref. [234], it is noted that the SDSFs are not independent and that the function S_{01} can be written in terms of the other two.

the spin-dependent cross section. This issue was explored by Cerd  o et al. [239], who developed a parametrisation for the spin structure functions in terms of the parameter $u = (qb)^2/2$, where q is the momentum transfer and $b = \sqrt{41.467/(45.0A^{-1/3} - 25.0A^{-2/3})}$ is the oscillator size parameter. This parametrisation takes the form

$$S_{ij} = N((1 - \beta)e^{-\alpha u} + \beta), \quad (2.43)$$

where the range of the parameters $\{N, \alpha, \beta\}$ is chosen such that S_{ij} spans the different possible forms presented in the literature. It was shown that this parametrisation was able to mitigate the uncertainties in the SD cross section and accurately recover the remaining particle physics parameters when the true form for the SDSFs was unknown.

2.4.2 Particle physics uncertainties

Apart from the unknown values for the WIMP mass m_χ and cross sections $\sigma_{SI,SD}$, the ratios of proton to neutron couplings are also *a priori* unknown. In the case of SI scattering, the dominant contribution comes from the coupling to strange quarks f_{Ts} , which is equal for protons and neutrons. It is therefore typically assumed that $f^p \approx f^n$, though as we have seen isospin violating dark matter models have been considered [205, 240, 241]. Similarly, for the SD interaction, a specific relation is typically assumed between the proton and neutron couplings, such as $a_p/a_n \approx \pm 1$. While specific models often predict such a relation [], it should be noted that this ratio is *a priori* unknown and fixing it is a model choice.

Further uncertainty is derived from the form of the interaction terms themselves. Here, we have considered the dominant contributions to scattering in the case of non-relativistic contact interactions. Extensions including mediator particles have been considered [242, 243], as well as models in which DM can interact electromagnetically with nuclei [244, 245]. There has also been significant effort towards developing a general non-relativistic field theory for the interaction of WIMPs with nuclei [156, 158, 246, 247]. Current limits can be translated into limits on the couplings associated with a range of effective operators. While this approach significantly widens the parameter space of dark matter direct detection, it is more general and does not rely on (potentially poor) assumptions about DM interactions.

2.4.3 Astrophysical uncertainties

Astrophysical uncertainties enter into the direct detection event rate through the local dark matter density ρ_0 and the speed distribution $f(v)$.

DM density, ρ_0

The DM mass density sets the overall scale of the scattering rate. As we shall discuss in Chapter 4, the DM density is degenerate with the interaction cross section, meaning that an accurate determination is important. One method of obtaining the value of ρ_0 is by mass modelling of the Milky Way (MW). One builds a model for the Galaxy incorporating various sources of mass, including the stellar bulge and disc, dust and a dark matter halo [248]. It is then possible to use various data such as the total MW mass, local surface mass density and the velocities of tracers to fit the parameters of this model and thereby extract ρ_0 . Estimates using this method tend to have a wide uncertainty, typically lying in the range $0.2 - 0.4 \text{ GeV cm}^{-3}$ (e.g. Ref. [248, 249]). A more recent determination using state-of-the-art data obtains a more precise but higher value of $\rho_0 = 0.47_{-0.06}^{+0.05} \text{ GeV cm}^{-3}$ [250] (though this depends on the choice of halo density profile).

An alternative method is to use local stellar kinematic data to constrain the gravitational potential near the Sun and thus obtain an estimate of ρ_0 . Using kinematic data from roughly 2000 K-dwarfs, Garbari et al. [251] obtain the value $\rho_0 = 0.85_{-0.50}^{+0.57} \text{ GeV cm}^{-3}$ while Zhang et al. , using a larger sample of 9000 K-dwarfs, obtain $0.28 \pm 0.08 \text{ GeV cm}^{-3}$. Including microlensing data, the range of allowed values at 1σ is $\rho_0 = 0.20 - 0.56 \text{ GeV cm}^{-3}$ [252]. A further model independent method was proposed by [253]. The advantage of such approaches is that one does not need to assume a particular form for the DM halo density profile. However, they may be more sensitive to assumptions about local equilibrium near the Sun's position.

In 2012, Moni Bidin et al. [254] used the dynamics of thick disk stars to constrain the DM density, finding a result consistent with no dark matter at the Sun's radius. However, a subsequent reanalysis by Bovy and Tremaine [255] showed that this result derived from a poor assumption about the velocity of stellar tracers as a function of galactic radius. Using the same data with more reasonable assumptions, the value $0.3 \pm 0.1 \text{ GeV cm}^{-3}$ was

obtained.

In spite of the large number of determinations, no consistent value appears to be emerging, with values ranging from $0.2\text{--}0.85\text{ GeV cm}^{-3}$. There also remain a number of uncertainties in these determinations, including the shape of the DM halo [] and assumptions about the local equilibrium of the Galaxy []. *Need citations...* The ‘standard’ value assumed in the analysis of direct detection experiments is 0.3 GeV cm^{-3} , though the exact origin of this number is unclear [256].

Probably need to talk about ultra-local distribution and clumpiness...

Speed distribution, $f_1(v)$

The speed distribution enters into the direct detection rate in the integral,

$$\eta(v_{\min}) \equiv \int_{v_{\min}}^{\infty} \frac{f_1(v)}{v} dv, \quad (2.44)$$

which is referred to as the ‘velocity integral’ or the ‘mean inverse speed.’ Direct detection experiments are traditionally analyzed within the framework of the Standard Halo Model (SHM), in which WIMPs are assumed to have a Maxwell-Boltzmann velocity distribution in the Galactic frame. In the Earth’s frame, this takes the form

$$f_{\text{SHM}}(\mathbf{v}) = N \exp\left(-\frac{(\mathbf{v} - \mathbf{v}_{\text{lag}})^2}{2\sigma_v^2}\right) \Theta(v_{\text{esc}} - |\mathbf{v} - \mathbf{v}_{\text{lag}}|), \quad (2.45)$$

where \mathbf{v}_{lag} specifies the velocity of the Earth frame with respect to the galactic rest frame and σ_v the velocity dispersion. The SHM distribution is obtained assuming a spherical, isothermal DM halo with density profile $\rho \sim r^{-2}$ and results in the relation $\sigma_v = v_{\text{lag}}/\sqrt{2}$. We truncate the distribution above the escape speed v_{esc} in the Galactic frame and the factor N is required to satisfy the normalization condition:

$$\int f(\mathbf{v}) d^3\mathbf{v} = 1. \quad (2.46)$$

By integrating over directions we obtain $f(v)$ and the speed distribution is then given by

$$f_1(v) = f(v)v^2 = \int f(\mathbf{v})v^2 d\Omega_v. \quad (2.47)$$

Within the SHM, there is some uncertainty on the parameters describing $f_1(v)$. The parameter v_{lag} is given by the local circular speed $v_c = 218 \pm 7 \text{ km s}^{-1}$ [257, 258] plus a contribution from the peculiar motion of the Sun and the Earth's orbital motion. This lag speed is typically assumed to be close to the local circular speed, though more recent determinations of the solar velocity point towards higher values [259, 260] of $240 - 250 \text{ km s}^{-1}$. The galactic escape velocity can be estimated from the radial velocities of MW stars; the RAVE survey obtain the range $v_{\text{esc}} = 533_{-41}^{+54} \text{ km s}^{-1}$ at 90% confidence [261, 262]. Moreover, it is not known how well the relation $\sigma_v = v_{\text{lag}}/\sqrt{2}$ holds, meaning that σ_v is in reality poorly constrained.

Even taking into account these uncertainties, the SHM is unlikely to be an accurate representation of the DM halo. Observations and N-body simulations indicate that the halo should deviate from a $1/r^2$ profile and may not be spherically symmetric. As a result alternative models have been proposed. Speed distributions associated with triaxial halos [263] or with more realistic density profiles [264] have been suggested, as well as analytic parametrisations which should provide more realistic behaviour at low and high speeds [265]. Self-consistent distribution functions reconstructed from the potential of the Milky Way have also been obtained [266, 267].

It is also possible to extract the speed distribution from N-body simulations. Such distribution functions tend [268–270] to peak at lower speeds than the SHM and have a more populated high speed tail. There are also indications that DM substructure may be significant, causing ‘bumps’ in the speed distribution, or that DM which has not completely phase-mixed - so-called ‘debris flows’ - may have a contribution [271]. It should be noted that N-body simulations do not probe down to the sub-milliparsec scales which are probed by direct detection experiments. This means that N-body speed distributions are averaged over large volumes in order to obtain sufficient statistics. The effect of probing the speed distribution over such large length scales (rather than on the ultra local scale of experiments) is not known.

Another result obtained from N-body simulations is the possibility of a dark disk. When baryons are included in simulations of galaxy formation, this results in the tidal disruption of DM subhaloes which are then preferentially dragged into the disk plane [272, 273]. The resulting dark disk corotates with approximately the same speed as the baryonic matter,

though with a smaller velocity dispersion $\sigma_v^{DD} \sim 50 \text{ km s}^{-1}$. This dark disk is expected to contribute an additional density 0.2-1.0 times the density of the halo (depending on the merger history of the Milky Way). The more recent ERIS results [30], comparing hydrodynamic and DM-only simulations, indicate a smaller density of just 10% that of the DM halo in a Milky Way mass galaxy.

Talk about ultra local distribution - and possibility of streams..?

In Fig. 2.2, we show some examples of possible dark matter speed distributions, each of which will result in different event rates. *Could also plot η for these...?* The impact of uncertainties in the WIMP speed distribution has been much studied (see e.g. Refs. [1, 274, 275]) and it has been shown that poor assumptions about the speed distribution may result in biased reconstructions of the DM mass and cross sections from future direct detection data. *[***Maybe some of this wants to be part of my first ‘results’ chapter***]* It is unknown which, if any, of these distributions best describes the true galactic DM speed distribution and there have therefore been numerous attempts to mitigate these uncertainties.

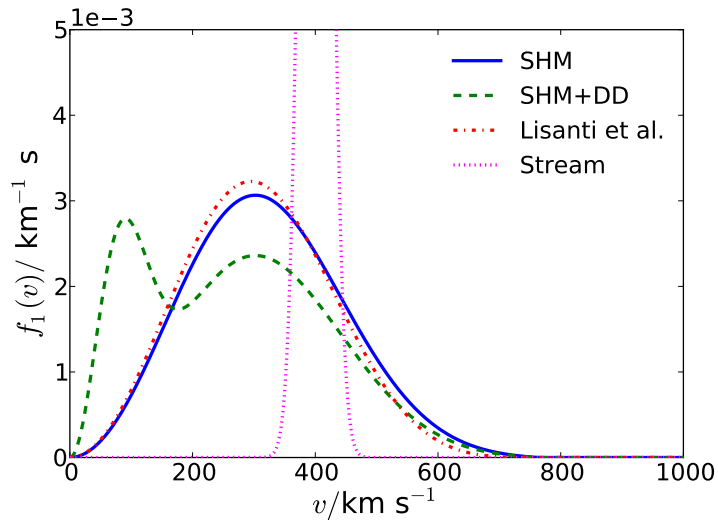


Figure 2.2: Some examples of possible dark matter speed distributions, including the Standard Halo Model (SHM), SHM with a 30% dark disk overdensity (SHM+DD), the distribution function of Lisanti et al. [265] and a stream.

A first step is to extend the SHM to incorporate uncertainties in v_{lag} , σ_v and v_{esc} into reconstructions. Strigari and Trotta [276] introduce a simple model of the Milky Way mass distribution, from which SHM velocity

parameters can be derived. They then use projected stellar kinematics and direct detection data to fit both the model parameters and the dark matter properties. A more direct approach is to directly fit the SHM velocity parameters, incorporating their uncertainties into the fitting likelihood. This method has been considered by Peter [277], and is typically used as a simple model of astrophysical uncertainties (especially in studies which focus on other aspects of direct detection, e.g. Ref. [278]). These methods allow bias in the reconstructed WIMP parameters to be eliminated when the underlying speed distribution is indeed in the SHM form. However, as shown by Peter [1], these methods fail when the distribution function differs from the standard Maxwellian case.

There have also been attempts to incorporate and fit more realistic distribution functions. Pato et al. [279] incorporate astrophysical uncertainties by using the distribution function of Lisanti et al. [265] and fitting the various shape parameters associated with it. In a more recent paper, Pato et al. [280] use projected direct detection data to fit a model of the Milky Way mass distribution, from which they derive a self-consistent distribution function (SCDF) using Eddington's formula. This means that the resulting speed distribution will be consistent with the underlying potentials of the galaxy's bulge, disk and dark matter, incorporating a broader range of shapes than the SHM alone. However, as the authors point out, velocity distributions from cosmological N-body simulations differ significantly from those expected from Eddington's formula. As with the Standard Halo Model, fitting a realistically-motivated distribution function is likely to result in biased reconstructions if the true distribution deviates significantly from the functional form used for fitting.

Methods which make no assumptions about the functional form of the speed distribution have had mixed success. Drees and Shan [281, 282] developed a method for estimating the WIMP mass by calculating moments of the speed distribution. However, this method still introduces a bias into the reconstructed WIMP mass and performs more poorly for heavier WIMPs and when finite energy thresholds are considered. An empirical ansatz for the speed distribution has also been suggested, specifically dividing the WIMP speed into a series of bins, with the distribution being constant within each bin [1]. *Hmmm...I talk about this method in more detail in a later chapter...* However, both of these still result in a significant bias in the reconstructed mass and cross section. A recent proposal by

Feldstein and Kahlhoefer [283] is to fit the velocity *integral* rather than the speed distribution. This proposal is the most promising so far and appears to give an unbiased reconstruction of the mass, though reconstructing the speed distribution itself remains problematic.

Finally, a method for analysing existing data has been developed by various authors [202, 203, 284]. At a given mass, a given experiment is sensitive only to speeds in a fixed range, set by $v_{\min}(E_{\min})$ and $v_{\min}(E_{\max})$. By considering only the range of speeds where two or more experiments overlap, one can ensure that the astrophysical contribution to both experiments is equal. This method has typically been used to assess the compatibility of different data sets and to set more robust limits on the WIMP interaction cross sections. Recently it has also been extended to accomodate more general forms for the WIMP interactions [285].

Understanding the uncertainties in the speed distribution and how they can be overcome is an active field of research

2.5 Conclusion

We have discussed the dark matter direct detection formalism, focussing on the contribution from scalar and axial-vector contact interactions. The non-relativistic speeds involved means that the event rate can be divided into a spin-dependent and spin-independent contribution. A number of sophisticated experiments have been and continue to be developed which should allow the rare nuclear recoils produced by these interactions to be detected. The use of different channels such as scintillation, ionisation and phonons not only allows the energy of these events to be measured but also aids discrimination against electronic recoils which can act as a significant background.

Tentative hints of a signal from the DAMA/LIBRA, CRESST-II and CoGeNT experiments have been interpreted as evidence for a WIMP with mass $m_\chi \sim 10$ GeV and cross section $\sigma_{SI} \sim 10^{-41}$ cm². However, null results from XENON, CDMS and other experiments are in tensions with this claimed signal. The origin of this discrepancy may lie in unidentified backgrounds or in an unconventional model for DM; corroboration from indirect and collider experiments may be needed before such a signal can be confirmed.

Finally, there are a number of uncertainties associated with calculating

direct detection event rates and therefore with interpreting data from these experiments. Nuclear uncertainties are typically more important for the SD rate than for the SI, though the method of Cerdeño et al. may be able to reduce the impact of such uncertainties. Particle physics uncertainties are significant, though the standard contact operator approach should be a good first approximation and effective field theories extending beyond this standard approach are being developed. Uncertainties in the *number* of dark matter particles, embodied in the local DM density ρ_0 , lead to a factor of roughly 2 uncertainty in the total direct detection rate.

In contrast, uncertainties in the speed distribution of dark matter are poorly controlled. Theoretical and computational considerations indicate that the benchmark assumption - the SHM - is not a good description of the WIMP distribution and while a large number of alternatives are available, it is unclear which, if any, of these may be correct. Attempts to treat the speed distribution more generally in data analysis have had mixed success, either leading to a biased reconstruction of the WIMP parameters or requiring additional assumptions or information about the WIMP, such as its mass. The wide range of possibilities for $f(v)$, as well as the consequences for misinterpreting future data, indicate that a more generalised approach is required.

Chapter 3

Parameter Reconstruction

3.1 Introduction

A common problem in physics is attempting to reconstruct the parameters of a model from a set of data. Stated more precisely, this is an attempt to answer the following question: given a set of data \mathcal{D} , what is the probability of a given set of model parameters $\boldsymbol{\theta}$ being the true, underlying parameters? But how do we interpret this question and what do we mean by the ‘probability’ of a given set of parameters?

In general, there are two approaches to parameter estimation. In *frequentist* inference, there is only a single, fixed set of true values for the model parameters $\boldsymbol{\theta}$. We imagine that the experiment (which produced the data \mathcal{D}) can be repeated a large number of times, giving independent results each time. The ‘probability’ associated with each set of parameters $\boldsymbol{\theta}$ is a measure of how frequently our experiment would produce data which looked similar to \mathcal{D} if $\boldsymbol{\theta}$ is the true value. In a frequentist framework, the true model parameters are fixed but unknown and we make statements about how confident we are that these true parameters lie in a particular range.

An alternative approach is *Bayesian* inference. The true parameter value is treated as a random variable and we use Bayes’ theorem to determine its probability distribution from the data:

$$P(\boldsymbol{\theta}|\mathcal{D}) = P(\boldsymbol{\theta}) \frac{P(\mathcal{D}|\boldsymbol{\theta})}{P(\mathcal{D})}. \quad (3.1)$$

In doing so, we need to know $P(\boldsymbol{\theta})$, known as the prior on the model parameters. This is a measure of our beliefs about the true value of $\boldsymbol{\theta}$ and

must be put in ‘by hand’. In a Bayesian framework, we combine the data with information about our prior expectations to make statements about the probability of $\boldsymbol{\theta}$ having a particular value.

These two approaches have different strengths and weaknesses, as we shall explore, and have both been applied to the problem of parameter exploration in physics. In this chapter, we will discuss how both frequentist and Bayesian statistics are used to make parameter estimates and measure the degree of certainty in these estimates. We will describe several methods which are used to explore parameter spaces and therefore make parameter inferences. Finally, we will outline how to calculate the likelihood \mathcal{L} - the probability of obtaining a particular set of data given some underlying model parameters - which is at the core of both the frequentist and Bayesian approaches.

3.2 Frequentist statistics

In frequentist statistics, the most important quantity to consider is the *likelihood* of a given point in parameter space, $\mathcal{L}(\boldsymbol{\theta})$, defined as the probability of obtaining the data \mathcal{D} , assuming that $\boldsymbol{\theta}$ is the true parameter value. The likelihood often takes a very small value (because the probability of obtaining a particular data set out of all possible data sets is typically very small), and so it is convenient to work with the log-likelihood $l(\boldsymbol{\theta}) = \log(\mathcal{L}(\boldsymbol{\theta}))$. The absolute value of $\mathcal{L}(\boldsymbol{\theta})$ carries no significance. However, the likelihood value of a particular point, relative to another, can be interpreted as a measure of the relative goodness of fit of the points. While the likelihood is not a probability distribution, in the limit of a large number of samples $l(\boldsymbol{\theta})$ follows a χ^2 distribution (as we shall discuss shortly) and therefore can have a probabilistic interpretation.

Often, we may not be interested in all of the parameters of $\boldsymbol{\theta}$. For example, we may partition the parameters into parameters of interests $\boldsymbol{\psi}$ and so-called nuisance parameters $\boldsymbol{\phi}$: $\boldsymbol{\theta} = (\boldsymbol{\psi}, \boldsymbol{\phi})$. These nuisance parameters may be parameters which we are not directly interested in, but which must be included in the analysis to account for all the relevant uncertainties. We often want to reduce the dimensionality of $\boldsymbol{\theta}$ to consider only how the likelihood varies as a function of $\boldsymbol{\psi}$.

One method of doing this is by maximizing the full likelihood function

over the nuisance parameters:

$$\mathcal{L}_p(\boldsymbol{\psi}) = \max_{\boldsymbol{\phi}} \mathcal{L}(\boldsymbol{\psi}, \boldsymbol{\phi}). \quad (3.2)$$

That is, for each value of $\boldsymbol{\psi}$, we select the maximum value of \mathcal{L} obtained from all possible values of $\boldsymbol{\phi}$. This projection onto the subset of parameters $\boldsymbol{\psi}$ is referred to as the profile likelihood.

An alternative method of reducing the dimensionality of the full parameter space is to calculate the mean likelihood:

$$\mathcal{L}_m(\boldsymbol{\psi}) = \frac{\int \mathcal{L}(\boldsymbol{\psi}, \boldsymbol{\phi}) d\boldsymbol{\phi}}{\int d\boldsymbol{\phi}}. \quad (3.3)$$

The mean likelihood allows us to take into account the structure of the likelihood function in the nuisance directions. The profile likelihood simply selects the largest likelihood value at each value of $\boldsymbol{\psi}$, even if this value is only realised over a small range of values in $\boldsymbol{\phi}$. By comparison, the mean likelihood receives a greater contribution from wide ranges of $\boldsymbol{\phi}$ which have a moderate likelihood value.

3.2.1 Parameter estimates

In frequentist statistics, the point estimate of a parameter is relatively unambiguous. This point estimate is given by the best fit point, or maximum likelihood estimate (MLE), $\hat{\boldsymbol{\theta}}$, such that:

$$\max \mathcal{L}(\boldsymbol{\theta}) = \mathcal{L}(\hat{\boldsymbol{\theta}}). \quad (3.4)$$

This estimate is the same whether we use the full likelihood or the profile likelihood, while using the mean likelihood may lead to a different value. In parameter inference, it is useful to consider the relative log-likelihood l_r :

$$l_r(\boldsymbol{\theta}) = -\log \left(\frac{\mathcal{L}(\boldsymbol{\theta})}{\mathcal{L}(\hat{\boldsymbol{\theta}})} \right). \quad (3.5)$$

The logarithm is a monotonically increasing function and therefore the maximum in the likelihood and the minimum in the relative log-likelihood are obtained for the same parameter values $\hat{\boldsymbol{\theta}}$. According to Wilks' theorem [286], the l_r is asymptotically χ^2 -distributed as the number of samples N increases,

$$-2l_r \sim \chi_k^2, \quad (3.6)$$

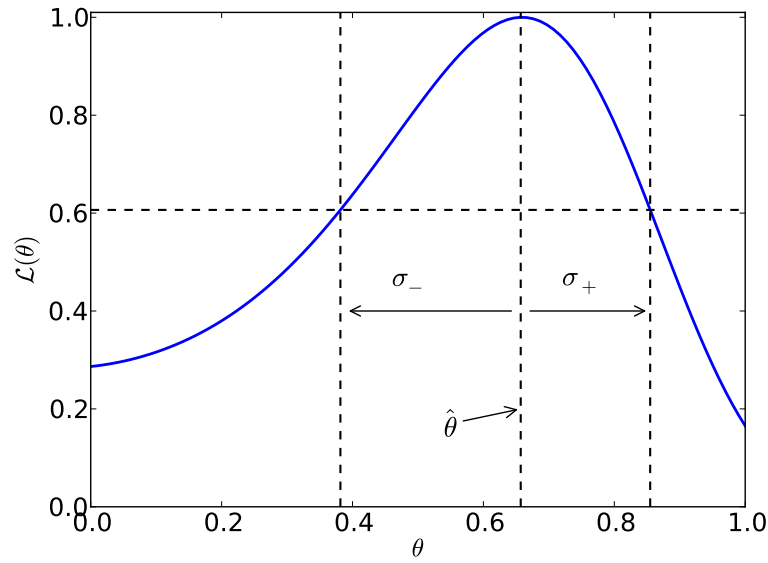


Figure 3.1: Illustration of likelihood-based parameter inference. The point estimate for the parameter θ is given by the best fit point $\hat{\theta}$. The 68% confidence interval is given by $\theta \in [\hat{\theta} - \sigma_-, \hat{\theta} + \sigma_+]$.

where the number of degrees of freedom k is equal to the dimensionality of the space $\boldsymbol{\psi} = (\psi_1, \dots, \psi_k)$. **Check minus signs etc...-everywhere** This asymptotic behaviour applies equally well for the full likelihood and the profile likelihood and allows us to construct confidence intervals. We construct a $p\%$ interval from all values of $\boldsymbol{\psi}$ for which

$$l_r \geq \frac{1}{2} F^{-1}(p\%; k), \quad (3.7)$$

where $F^{-1}(p\%; k)$ is the inverse cumulative distribution of a χ^2 distribution with k degrees of freedom. That is we reject all parameter values for which l_r exceeds the p^{th} percentile of the χ_k^2 distribution. This is essentially a goodness-of-fit test to determine, assuming that $\hat{\boldsymbol{\theta}}$ is the true parameter value, which values of $\boldsymbol{\theta}$ would not be rejected at the $p\%$ level. **Check this carefully...** Equivalently, in terms of the likelihood, we include values of $\boldsymbol{\theta}$ for which

$$\mathcal{L}(\boldsymbol{\theta}) \geq \exp\left(-\frac{1}{2} F^{-1}(p\%; k)\right) \mathcal{L}(\hat{\boldsymbol{\theta}}). \quad (3.8)$$

We illustrate this methodology in Fig. 3.2.

3.3 Bayesian statistics

In bayesian statistics, we wish to obtain the *posterior* probability distribution $\mathcal{P}(\boldsymbol{\theta}) = P(\boldsymbol{\theta}|\mathcal{D})$. This is obtained from Bayes' theorem:

$$\mathcal{P}(\boldsymbol{\theta}) = P(\boldsymbol{\theta}|\mathcal{D}) = P(\boldsymbol{\theta}) \frac{P(\mathcal{D}|\boldsymbol{\theta})}{P(\mathcal{D})}. \quad (3.9)$$

Here $P(\mathcal{D})$ is the probability of obtaining the data \mathcal{D} . However, this does not depend on the theoretical parameters $\boldsymbol{\theta}$ and we can therefore take it as an overall normalising factor for the probability distribution. The likelihood enters into the Bayesian framework as probability of the data given the model parameters $P(\mathcal{D}|\boldsymbol{\theta}) = \mathcal{L}(\boldsymbol{\theta})$. Finally, the prior $P(\boldsymbol{\theta})$ encodes our *a priori* knowledge about the true value of $\boldsymbol{\theta}$. If the value of a parameter, say θ_1 , is known to be approximately $\theta_1 = \hat{\theta}_1 \pm \sigma_\theta$, we may choose a Gaussian prior to reflect this:

$$P(\theta_1) \propto \exp\left(-\frac{(\theta_1 - \hat{\theta}_1)^2}{2\sigma_\theta^2}\right). \quad (3.10)$$

Alternatively, we may have a very limited knowledge of θ_1 and may choose a linear-flat or log-flat prior over some range of values: $P(\theta_1) \propto 1$ or $P(\log(\theta_1)) \propto 1$. In the case of a linear-flat prior, $\mathcal{P}(\boldsymbol{\theta}) = \mathcal{L}(\boldsymbol{\theta})$ and the Bayesian and frequentist frameworks coincide. In contrast to the likelihood, the posterior distribution is considered a probability distribution, even in the case of small numbers of samples.

As in the frequentist case, we may wish to reduce the dimensionality of the parameter space to include only those parameters of interest $\boldsymbol{\psi}$. When dealing with the posterior probability, this is typically done by marginalisation. The marginalised posterior \mathcal{P}_m is obtained by integrating over the nuisance parameters:

$$\mathcal{P}_m(\boldsymbol{\psi}) = \int \mathcal{P}(\boldsymbol{\psi}, \boldsymbol{\phi}) d\boldsymbol{\phi}. \quad (3.11)$$

Just as \mathcal{P} is a probability distribution function for the parameters $\boldsymbol{\theta}$, \mathcal{P}_m is a probability distribution function for the parameters of interest $\boldsymbol{\psi}$ - specifically, the marginalised probability distribution.

3.3.1 Parameter estimates

In contrast to the frequentist case, there are several possibilities for a point parameter estimate **look up the qualities of each (mode/mean/median)**.

Because \mathcal{P} is a probability distribution, it can be described by several location parameters:

Mode - the mode of the probability distribution is the value of θ which maximises \mathcal{P} . This is also known as the maximum a posteriori (MAP) estimate and can be viewed as analogous to the maximum likelihood estimator.

Median - the median value of the parameter θ satisfies

$$\int_{-\infty}^{\theta_{\text{median}}} \mathcal{P}(\theta) d\theta = \frac{1}{2}. \quad (3.12)$$

This means that there is as much probability density below θ_{median} as above.

Mean - the mean value $\langle \theta \rangle$ is given by

$$\langle \theta \rangle = \int \theta \mathcal{P}(\theta) d\theta. \quad (3.13)$$

Each of these will behave differently for different posterior probability distributions. The MAP estimate indicates where the greatest probability density is and may be useful when the posterior is sharply peaked. The mean and median better reflect the global properties of the posterior probability, but may be misleading if the distribution is multimodal.

Talk about multimodality Do a comparison of frequentist and bayesian - when do they coincide?

We also wish to make statements about the possible range of values for parameters. In a Bayesian framework, we define the $p\%$ *credible* interval $\mathcal{C}_{p\%}$, defined such that it encloses $p\%$ of the probability. Again, there are several possibilities for how to define $\mathcal{C}_{p\%} = [\mathcal{C}_{p\%}^{\min}, \mathcal{C}_{p\%}^{\max}]$, such as:

Central interval - the interval which has the mean as its central value.

Equal tails interval - the total probability below the interval is the same as above the interval,

$$\int_{-\infty}^{\mathcal{C}_{p\%}^{\min}} \mathcal{P}(\theta) d\theta = \int_{\mathcal{C}_{p\%}^{\max}}^{\infty} \mathcal{P}(\theta) d\theta. \quad (3.14)$$

Highest density interval - the interval defined by all values $\mathcal{P}(\theta) \geq \gamma$, where γ is defined by

$$\int_{\mathcal{P}(\theta) \geq \gamma} \mathcal{P}(\theta) d\theta = p\%. \quad (3.15)$$

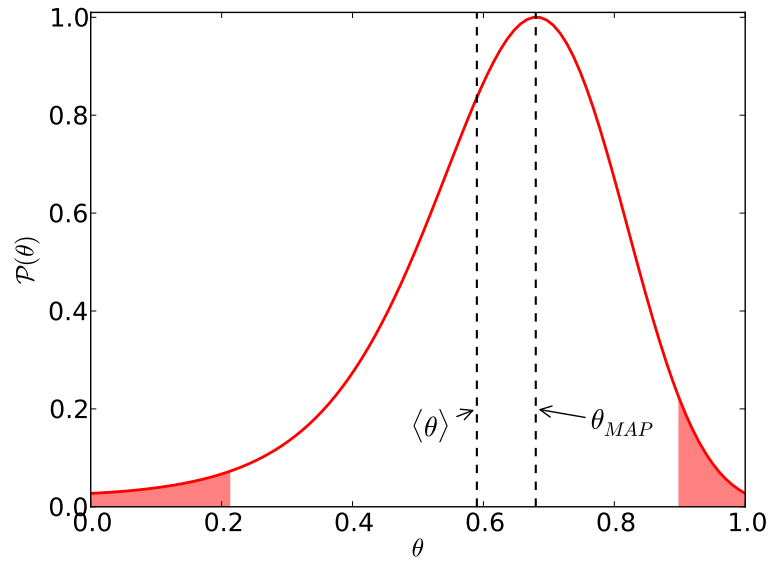


Figure 3.2: Illustration of posterior-based parameter inference. We show the difference between the MAP and mean parameter estimates. We also show one possible 95% credible interval - the probability in the shaded tails is equal.

Again, when we specify a credible interval, we must specify which definition we are using. These definitions can also be extended simply to the case where the parameter space of interest has a higher dimension. In Fig. ??, we illustrate the MAP estimate and mean for a hypothetical posterior distribution. We also show the 95% credible interval obtained using the equal tails method.

3.4 Exploring the parameter space

So far we have considered how, given $\mathcal{L}(\theta)$ or $\mathcal{P}(\theta)$, we can make parameter inferences about θ . However, we have not so far considered how we can evaluate these functions. We do not typically know *a priori* where $\mathcal{L}(\theta)$ or $\mathcal{P}(\theta)$ are maximised or what shape they have. In this section, we will briefly discuss two methodologies for mapping out these functions: Markov Chain Monte Carlo and Nested Sampling.

3.4.1 Markov chain monte carlo

In the Markov chain monte carlo (MCMC) method [287] **Need original citations as well**, we generate a chain of points in the parameter

space $\{\boldsymbol{\theta}_i\}$. A new point $\boldsymbol{\theta}_{j+1}$ in the chain is generated from the current point $\boldsymbol{\theta}_j$ by picking from some proposal distribution $P(\boldsymbol{\theta}_j; \boldsymbol{\theta}_{j+1})$. Under the Metropolis-Hastings algorithm [288], the new point is accepted with probability

$$\min \left\{ 1, \frac{\mathcal{L}(\boldsymbol{\theta}_{j+1})Pr(\boldsymbol{\theta}_{j+1})}{\mathcal{L}(\boldsymbol{\theta}_j)Pr(\boldsymbol{\theta}_j)} \right\}, \quad (3.16)$$

as long as the proposal distribution is symmetric. Over a large number of points, the chain should converge and eventually the number density of chain positions should be proportional to the posterior $n(\boldsymbol{\theta}) \propto \mathcal{P}(\boldsymbol{\theta})$. In addition, we will also have the value of the likelihood $\mathcal{L}(\boldsymbol{\theta})$ evaluated at all of the points in the chain.

Care must be taken to ensure that the chain has converged before the results can be interpreted. Typically some initial set of points is discarded as ‘burn-in’, after which the chain is deemed to have converged. However, it is often unclear when convergence has been reached. Moreover, each chain position will dependent slightly on the previous position. However, we want to obtain independent samples from the posterior distribution. Therefore, the chain is typically thinned (by some factor of order 25-50) [289], with only some of the positions being retained. Finally, we must select how many positions we want to obtain in the chain before we stop the random walk, in the hopes that the chain has adequately explored the parameter space. **Talk about R-tests...?**

When $\mathcal{P}(\boldsymbol{\theta})$ is multimodal, sharply peaked or has strong degeneracies among the parameters, exploration by the chain can be slow. It can be unclear whether convergence has been achieved, especially if the chain becomes trapped in one of the modes of the distribution. One way to improve the rate of convergence is to use high temperature MCMC [287, 290]. We employ a ‘heated’ chain with temperature $T = 2$, meaning that we accept new points with probability

$$\min \left\{ 1, \left(\frac{\mathcal{L}(\boldsymbol{\theta}_{j+1})Pr(\boldsymbol{\theta}_{j+1})}{\mathcal{L}(\boldsymbol{\theta}_j)Pr(\boldsymbol{\theta}_j)} \right)^{1/T} \right\}. \quad (3.17)$$

We are now effectively sampling from a flatter posterior distribution, which allows a more rapid mixing and convergence of the chain. However, to achieve the same precision as in the $T = 1$ case, we require a larger number of samples. The distribution of chain positions obtained at the higher temperature is then $n_T(\boldsymbol{\theta}) \propto \mathcal{P}^{1/T}(\boldsymbol{\theta})$. We recover the distribution of

positions at $T = 1$ by ‘cooling’ the chain:

$$n(\boldsymbol{\theta}) = n_T(\boldsymbol{\theta}) (\mathcal{P}(\boldsymbol{\theta}))^{1-1/T}. \quad (3.18)$$

Pros and cons? Good at finding the best fit?

One popular, publicly available MCMC code is COSMOMC [289]. This was developed in the context of cosmological parameter estimation, but can be used as a generic MCMC sampler. **Anything else...?** When the parameter space is of a high dimension or has a number of modes, MCMC methods may prove slow. Such methods also rely on a suitable choice of burn-in and thinning factors, as well as a determination of whether convergence has occurred. Next, we explore an alternative method for efficiently obtaining samples from the posterior distribution.

3.4.2 Nested sampling

The nested sampling method [291] was originally proposed as a method of calculating the overall normalising factor which appears in Bayes’ theorem, $P(\mathcal{D})$. However, it produces as a by-product samples from the posterior distribution and values of the likelihood function. In nested sampling, we take an initial sample of points (so-called ‘live’ points) from the parameter space and evaluate the likelihood at each point. The live point with the lowest likelihood \mathcal{L}_0 is removed from the sample and replaced with another point sampled from the parameter space with $\mathcal{L}_i > \mathcal{L}_0$. Thus, the algorithm explores the prior in concentric shells of \mathcal{L} . Each new live point can be assigned a weight w_i , obtained from an estimate of change in prior volume between concentric shells. Finally, each point can then be assigned a posterior density

$$p_i = \frac{w_i \mathcal{L}_i}{\mathcal{Z}}. \quad (3.19)$$

The Bayesian evidence $\mathcal{Z} \equiv P(\mathcal{D})$ is obtained by summing $\sum_i w_i \mathcal{L}_i$ and the algorithm continues until this is determined to some desired precision.

In order to continue, we must be able to select points from the prior subject to the hard constraint $\mathcal{L}_i > \mathcal{L}_0$. As the algorithm moves to higher values of \mathcal{L}_0 , points with a higher likelihood than this tend to become localised in very small regions of the parameter space. In addition, if the likelihood is multimodal or has pronounced degeneracies, the sampling of

points subject to this constraint becomes highly inefficient. The MULTINEST algorithm [292–294] uses multimodal, ellipsoidal nested sampling to improve performance. As \mathcal{L}_0 increases during the calculation, MULTINEST uses the current live points to approximate the isolikelihood contour by a series of ellipsoidal surfaces. New points are drawn only from within these ellipsoids, increasing the efficiency of the sampling but still ensuring that the constraint $\mathcal{L}_i > \mathcal{L}_0$ is satisfied. The algorithm can also accomodate multiple modes in the posterior which can be explored independently.

In utilising the MultiNest algorithm, we must decide how many live point to use N_{live} . This determines how closely the isolikelihood contours can be followed, how dense the posterior samples will be and, in the case where there are highly localised modes, how well explored the prior will be. We must also decide the tolerance of the algorithm `tol`. This determines the precision with which \mathcal{Z} should be determined and therefore how high up the likelihood surface the algorithm should explore. Finally, we can introduce an efficiency `eff`, which is the desired sampling efficiency. In order to (attempt to) achieve this, the algorithm rescales the volume of the bounding ellipsoids to incorporate more or less of the prior volume, as desired.

Model selection...? - Leave this until later...

Could look at event generation...

3.5 Likelihood examples

We have discussed how, given the likelihood and posterior, we can make parameter inferences. We have also explored methods by which these functions can be efficiently explored. Finally, we look at how to evaluate the likelihood for a given data set.

The simplest signal which can be observed is a number of events N_o . We can calculate from the model parameters θ the expected number of events N_e following Sec. ???. The probability of obtaining the data given the model parameters is then given by the Poisson likelihood:

$$\mathcal{L}(N_o|N_e) = \frac{N_e^{N_o}}{N_o!} e^{-N_e}. \quad (3.20)$$

We can extend this definition to incorporate data which has been divided

into bins with $N_e^{(i)}$ events expected and $N_o^{(i)}$ observed in the i^{th} bin:

$$\mathcal{L}(\{N_o^{(i)}\}|\{N_e^{(i)}\}) = \prod_{i=1, N_{\text{bins}}} \frac{(N_e^{(i)})^{N_o^{(i)}}}{(N_o^{(i)})!} e^{-N_e^{(i)}}. \quad (3.21)$$

We can also consider the unbinned likelihood by taking the limit as the bin width tends to zero,

$$\mathcal{L}(\mathcal{D}|\boldsymbol{\theta}) = \frac{N_e^{N_0}}{N_0!} e^{-N_e} \prod_{i=1, N_e} P(E_i), \quad (3.22)$$

where N_e and N_o are the number of events expected and observed across the whole experiment. We have assumed here that each event has an associated measurement, the energy E_i , and we take the product over the normalised event rates:

$$P(E) = \frac{dR}{dE_R}(E) \left[\int_0^\infty \frac{dR}{dE_R}(E') dE' \right]^{-1}. \quad (3.23)$$

Finally, we may wish to include the effects of background in the analysis. Then, we must take into account the fact that we do not know whether a given even is due to the signal or background. It will derive from the signal with probability

$$f_S = \frac{N_{\text{signal}}}{N_{\text{signal}} + N_{\text{background}}}, \quad (3.24)$$

and from the background with probability $f_{BG} = 1 - f_S$. Thus, we obtain the full likelihood

$$\mathcal{L}(\mathcal{D}|\boldsymbol{\theta}) = \frac{N_e^{N_0}}{N_0!} e^{-N_e} \prod_{i=1, N_e} (P_S(E_i))^{f_S} (P_{BG}(E_i))^{f_{BG}}. \quad (3.25)$$

Here, N_e and N_o are the total number of expected events including both signal and background. We must also take into account the normalised spectra of the signal $P_S(E)$ and the background $P_{BG}(E)$ separately, multiplying the contributions of both.

What else do I need?

ASIMOV!!!

3.6 Conclusions

In this chapter, we have described two frameworks for parameter inference - frequentist and Bayesian statistics. We have described various possibilities

for point and spread estimates of parameters in both cases, as well as how these should be interpreted. While both methodologies present different viewpoints on the problem of parameter estimation, they can be used in a complementary fashion and can, in the case of flat priors, coincide.

The MCMC and MultiNest algorithms can be used to efficiently sample from both the likelihood and posterior distribution, even in the case of highly complicated parameter spaces with multiple modes or pronounced degeneracies. We have also detailed a number of relevant cases for the explicit form of the likelihood function in binned and unbinned scenarios.

These techniques are essential for the later work presented in this thesis. In attempting to parametrise the dark matter velocity distribution a large number of parameters are needed to capture a range of possible features. In addition to particle physics and experimental nuisance parameters, this leads to a large parameter space which is a challenge to explore. However, as we will show, these techniques allow us to make concrete and unbiased estimates of both particle physics and astrophysical parameters based on future data sets.

Chapter 4

Parametrising the speed distribution

As we have explored in Chapter 2, there are a number of uncertainties associated with calculating the direct detection event rate. These translate directly into uncertainties in the analysis of direct detection results, present and future. If these uncertainties are properly accounted for, they can provide a more realistic estimates of uncertainties on the WIMP cross sections σ_p^{SI} and σ_p^{SD} and WIMP mass m_χ . If, however, our assumptions do not reflect the underlying nuclear physics, particle physics or astrophysics of dark matter, this can lead to a bias in the WIMP parameters. Understanding these uncertainties and how to mitigate them is therefore of great importance.

The WIMP speed distribution $f(v)$ enters into the direct detection event rate as it influences both the typical flux of dark matter particles and the typical recoil energy imparted during a scattering event. Unfortunately, the typical flux and recoil energy are also strongly dependent on the WIMP mass m_χ . This leads to a strong degeneracy between m_χ and $f(v)$ and, as discussed in Sec. ??, the possibility of significant bias in the reconstruction of the WIMP mass (see e.g. Ref [1]). **Maybe move some of the DD background chapter stuff to here...** In Sec. ??, we revisit the problem of reconstructing the WIMP mass and how it can be influenced by poor assumptions about $f(v)$.

Because the speed distribution is so poorly constrained, an ideal goal would be to construct the most general parametrisation for $f(v)$ which can accommodate a wide range of possibilities for the true functional form.

This approach has previously been explored by Peter [1], who wrote down an empirical parametrisation for $f(v)$ as a series of constant bins in v . However, this still resulted in a bias in the reconstructed WIMP parameters. In Sec. ??, we analyse in more detail the performance of this method and attempt to explain where this bias comes from.

In Sec. ??, we discuss a method analogous to that of Peter but for parametrising the WIMP *momentum* distribution in terms of a series of constant bins. This transformation helps remove some of the degeneracy between the WIMP mass and distribution function and improves reconstructions of the mass compared to binning in $f(v)$. However, this method is not generally applicable and begins to fail for low mass WIMPs.

Finally, we compare these different parametrisations in Sec. ?? and discuss how they relate to alternative methods of accounting for astrophysical uncertainties in direct detection experiments. We will also discuss the weaknesses of the momentum parametrisation, highlighting where remaining work is needed.

4.1 Uncertainties in $f(v)$

Dark matter direct detection experiments simultaneously probe the WIMP speed distribution and WIMP mass. As described in Chapter 2, the differential event rate relevant for direct detection experiments is

$$\frac{dR}{dE_R} = \frac{\rho_0}{2\mu_{\chi p}^2 m_x} \sigma_{SI}^p A^2 F_{SI}^2(E_R) \int_{v_{\min}}^{\infty} \frac{f(v)}{v} dv, \quad (4.1)$$

where for simplicity we have assumed that the coupling to protons and neutrons is the same ($f_p \approx f_n$) and we consider only the spin-independent (SI) contribution to the rate. Not also is the SI contribution expected to dominate for heavy nuclei (due to the A^2 enhancement), but considering only a single contribution allows us to focus on the degeneracies between m_χ , σ_p^{SI} and $f(v)$.

We have previously outlined in Chapter 2 that there are various possibilities for the form of the WIMP speed distribution and that poor assumptions about this form may lead to biased reconstructions of the WIMP parameters. This has been demonstrated, for example, by Peter [1], who attempted to reconstruct the WIMP mass and SI cross section from mock data sets based on future direct detection experiments. In order to gener-

ate the data, an SHM distribution function with an additional contribution from a dark disk was assumed. However, the posterior distribution for m_χ and σ_p^{SI} was obtained assuming that $f(v)$ could be well described by a single Maxwell-Boltzmann (MB) distribution (with average speed and speed dispersion included as nuisance parameters). The resulting marginalised 68% and 95% contours for m_χ and σ_p^{SI} are shown in Fig. 4.1, with the true parameter values given by the black crosses.

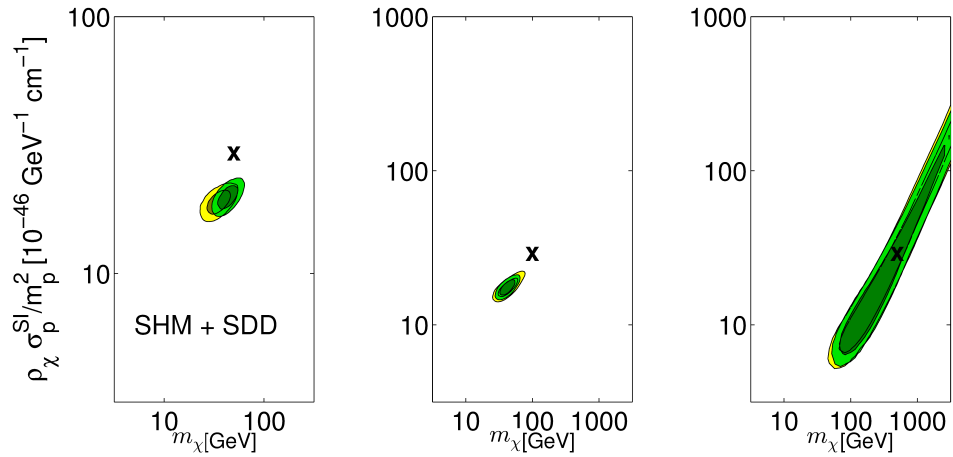


Figure 4.1: **Need caption...** Reproduced from Ref. [1]

Even including some uncertainties in the shape of the MB speed distribution, there is still a clear bias in the reconstructed WIMP parameters. The MB speed distribution cannot reproduce the shape of the event spectrum closely and the WIMP mass and cross section move to different values to compensate and improve the fit. Not only is there a bias, but the resulting contours are relatively small. In this case, if we trust the ansatz of a MB distribution, we would mistakenly believe that we had reconstructed the WIMP parameters accurately with a high precision. Thus, there is a need for a more general approach which allows a broad range of speed distributions to be probed. We discuss the consequences of such an approach now. *Improve flow...*

We can write the integral over the speed distribution as

$$\eta(v_{\min}) \equiv \int_{v_{\min}}^{\infty} \frac{f(v)}{v} dv, \quad (4.2)$$

where v_{\min} is given by

$$v_{\min} = v_{\min}(E_R, m_\chi, m_N) = \sqrt{\frac{m_N E_R}{2\mu_{\chi N}^2}}. \quad (4.3)$$

If we treat $f(v)$ as a free function (subject to the condition that it be normalised to unity and everywhere positive), this is equivalent to treating $\eta(v_{\min})$ as a free function (subject to the equivalent condition that η be a monotonically decreasing function of v_{\min}). This represents an entirely agnostic approach to $f(v)$, assuming that we know nothing at all about its functional form. Unfortunately, if we fix m_N , any change in the form of η can be counteracted by a change in m_χ (and a resulting change in v_{\min}) leading to the same spectral shape $\eta(E_R)$. This means that for a single experiment, the WIMP mass and $f(v)$ are exactly degenerate and we need multiple experiments to disentangle the two [282]. We will phrase this in more concrete terms later in Sec. ??.

Another consideration when parametrising $f(v)$ is the range of sensitivity of the experiments. Each experiment will have a window recoil energies to which it is sensitive $[E_{\min}, E_{\max}]$ (though the recoil detection efficiency may vary across this window). This means that for a given WIMP mass, each experiment will be sensitive only a range of WIMP speeds $[v_{\min}(E_{\min}), v_{\min}(E_{\max})]$. WIMPs with speeds smaller than $v_{\min}(E_{\min})$ do not contribute to the velocity integral defined in Eq. 4.2. WIMPs with speeds above $v_{\min}(E_{\max})$ can contribute to the overall spectrum, but they contribute only a constant, additive rate; the experiment is not sensitive to the *shape* of the speed distribution above this maximum speed. Thus, each experiment has a range of speeds to which it is sensitive. If we wish to probe the shape of $f(v)$, these ranges must have some overlap between the different experiments. Otherwise, the $f(v)$ can be varied independently across each speed range and the degeneracy between m_χ and $f(v)$ remains.

Insert and explain plot...

In order to get a handle on $f(v)$ and therefore the WIMP mass we therefore need several direct detection experiments, which use different target materials but which probe overlapping WIMP speeds. However, we must come up with a way of writing our general function $f(v)$ which allows us to reconstruct it by fitting to the data. Such a parametrisation should correspond to a physical distribution function; it should be normalised and should be everywhere positive. We should try to write down a parametri-

sation which spans a wide range of underlying distribution functions and which does not introduce any additional bias into attempts to reconstruct the WIMP parameters. For this reason, it is necessary to carefully test any proposed parametrisation. We now explore in more detail several proposals for what such a general parametrisation should look like.

Talk about the transformation from the Galactic to Earth frame...

4.2 Binned speed distribution

Peter proposed using an empirical speed distribution in the form of series of bins in speed v in order to fit to data. Explicitly, we write the WIMP speed distribution (in the Earth frame), as a series of N bins of constant value, with bin edges $\{\tilde{v}_i\}$: **This is the directionally averaged velocity distribution...**

$$f(v) = \sum_{i=1}^N g_i W(v; \tilde{v}_i, \Delta v), \quad (4.4)$$

where the top-hat function, W , is defined as:

$$W(v; \tilde{v}_i, \Delta v) = \begin{cases} 1 & v \in [\tilde{v}_i, \tilde{v}_i + \Delta v] \\ 0 & \text{otherwise} \end{cases}. \quad (4.5)$$

We must choose a maximum speed $v_{\max} = N\Delta v$ up to which we parametrise. Beyond this speed, we set $f(v)$ to zero, so we should choose a conservative value which does not risk truncating the speed distribution prematurely. Based on the results of the RAVE surveys [261, 262], the Galactic escape speed is estimated to be $v_{\text{esc}} < 587$ at the 90% confidence level. Assuming a local circular speed of $v_c \sim 220 \text{ km s}^{-1}$ [257, 258], this means that in the Earth frame, particles with speeds significantly higher than $v_c + v_{\text{esc}} \sim 800 \text{ km s}^{-1}$ should not be gravitationally bound. This is consistent with results for the local escape speed obtained in N-body simulations [269]. We therefore choose a value $v_{\max} = 1000 \text{ km s}^{-1}$ as a conservative upper limit for the parametrisation.

The form for the distribution function given in Eq. 4.4 is the directionally-averaged WIMP velocity distribution, $f(v)$. The WIMP *speed* distribution

is then given by

$$f_1(v) = \sum_{i=1}^N g_i v^2 W(v; \tilde{v}_i, \Delta v). \quad (4.6)$$

Imposing normalisation of the speed distribution, we obtain the following constraint on the $\{g_i\}$:

$$\sum_{i=1}^N g_i [(\tilde{v}_i + \Delta v)^3 - \tilde{v}_i^3] / 3 = 1. \quad (4.7)$$

For notational convenience, we also define

$$\hat{g}_i = g_i [(\tilde{v}_i + \Delta v)^3 - \tilde{v}_i^3] / 3, \quad (4.8)$$

such that the normalisation condition becomes

$$\sum_{i=1}^N \hat{g}_i = 1. \quad (4.9)$$

Distinguish between f_1 and f ...

Earth frame

We illustrate the form of this binned distribution for $f(v)$ in Fig. 4.2. We show the Standard Halo Model in the Earth frame (blue line) as well as the binned approximation to the SHM (red line). This approximation is obtained by integrating the WIMP speed distribution over each of the bins:

$$\hat{g}_i^{\text{approx}} = \int_{\tilde{v}_i}^{\tilde{v}_i + \Delta v} f_1^{\text{SHM}}(v) dv. \quad (4.10)$$

This allows us to examine how closely the binned parametrisation can be used to approximate the SHM. However, in a realistic scenario, these bin parameters $\{\hat{g}_i\}$ would form part of the parameter space, along with m_χ and $\sigma_{\text{p}}^{\text{SI}}$, which must be explored based on the data. **Also plot the approximate form for η here!**

In Ref. [1], Peter found evidence that this method still lead to a bias in the reconstructed WIMP mass and cross section, despite the apparent generality of this binned distribution function. Here, we explore this method further. In particular, we consider a large number of realisations of data sets from hypothetical future experiments, assuming some fiducial benchmark model. We then attempt to reconstruct the WIMP mass for

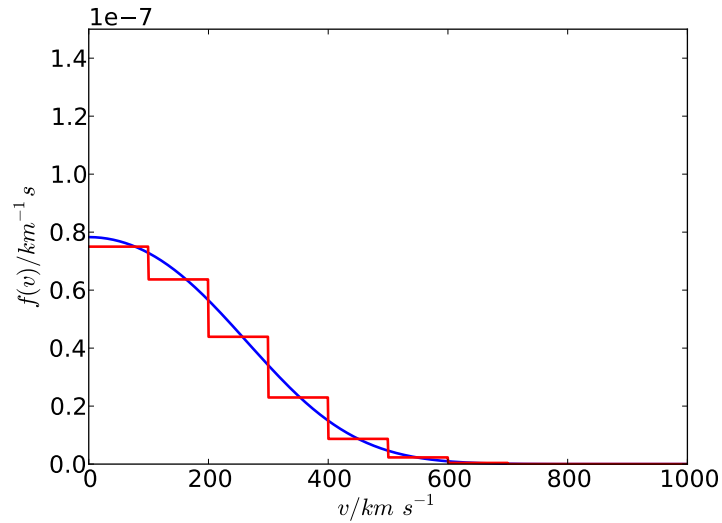


Figure 4.2: Binned approximation to the SHM in the Earth frame. The bin heights are obtained from Eq. 4.10. We note that shown here is $f(v)$, the directionally-averaged velocity distribution. We must multiply by v^2 to obtain the speed distribution $f_1(v)$.

each realisation, allowing us to determine how the method performs statistically and whether the bias found by Peter is present in all data sets or only in a small number of Poissonian realisations.

4.2.1 Benchmark Parameters and Experiments

As noted in Sec. 4.1, it is impossible to estimate the WIMP mass from a single experiment if no assumptions are made about $f(v)$, so we consider three next-generation detectors, modelled on experiments which are currently in development. Each experiment is characterised by a single (suitably averaged) target nucleus mass, m_N , a total detector mass, m_{det} , an effective exposure time, t_{exp} , and a pair of energies, E_{min} and E_{max} , which mark the extent of the signal region. We focus on a particular set of experimental parameters in order to provide a concrete example of how the WIMP parameters can be estimated accurately. Table 4.1 shows the experimental parameters used in this work, which are chosen to approximately match those used by Peter [1].

We assume perfect and uniform detection efficiency - that is, all signal events and no background events survive analysis cuts. We also assume perfect energy resolution. For a real experiment, these assumptions will almost certainly not hold, for example due to variations in the relative

	XENON1T	SuperCDMS	WArP
	[295]	[296]	[297]
Detector Target	Xe	Ge	Ar
Nuclear Mass, m_N/amu	131	73	40
Detector Mass, m_{det}/kg	1000	100	1000
Exposure Time, $t_{\text{exp}}/\text{days}$	60.8	109.5	365
Energy Range, $[E_{\text{min}}, E_{\text{max}}]/\text{keV}$	[2,30]	[10,100]	[30,130]

Table 4.1: Parameter values for the three mock experiments used in this work, chosen to closely match those used in Ref. [1]. The meanings of the experimental parameters are described in Sec. 4.2.1.

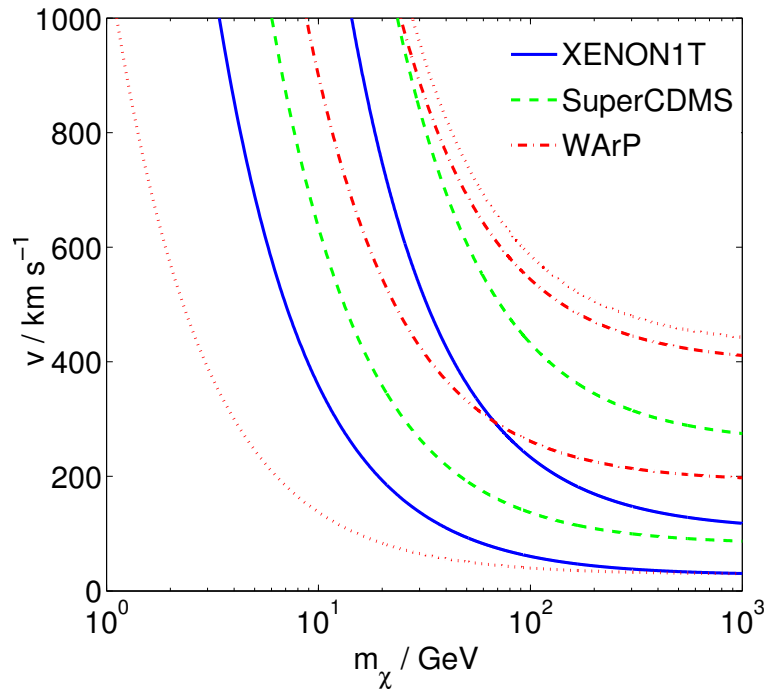


Figure 4.3: Range of accessible WIMP speeds for each of the three mock experiments: XENON1T-like (solid blue), SuperCDMS-like (dashed green) and WArP-like (dot-dashed red). Each pair of lines corresponds to the maximum and minimum accessible WIMP speeds for a given experiment. The outermost dotted red lines show the accessible speeds for the adjusted parametrisation range described in Sec. ??.

scintillation efficiency of Xenon [298], but the results presented here should be viewed as a proof of principle in the ideal case.

Figure 4.3 shows the minimum and maximum accessible WIMP speeds for each experiment. All three experiments rapidly become insensitive to WIMPs with speeds less than $\sim 1000 \text{ km s}^{-1}$ as the WIMP mass drops below $m_\chi \sim 10 \text{ GeV}$. This suggests that the experiments considered here

generically have a low sensitivity to such light WIMPs, producing too few events for accurate parameter reconstruction. **So what...?**

For comparison with later methods, we consider here a single benchmark model: $m_\chi = 50$ GeV, $\sigma_p^{\text{SI}} = 10^{-44} \text{cm}^2$ and the SHM. We assume a fixed value for the local DM density $\rho_0 = 0.3 \text{ GeV cm}^{-3}$. As will be explained in Sec. ??, the precise values of σ_p^{SI} and ρ_0 are not particularly important due to the degeneracy between these two parameters. The total number of events from all three detectors combined typically ranges from around 300 to 600 for the different benchmark parameters which will be considered in this chapter.

4.2.2 Parameter reconstruction

We generate 250 mock data sets using the experiments described above. We then use the Markov Chain Monte Carlo (MCMC) package CosmoMC [] to make parameter inferences on the parameters $m_\chi, \sigma_p^{\text{SI}}, \{\hat{g}_i\}$, where \hat{g}_i are the bin parameters for a 5 bin speed distribution function. We sample the WIMP mass and cross-section logarithmically in the ranges $[10, 1000]$ GeV and $[10, 10000] \times 10^{-47} \text{ cm}^2$ respectively, with log-flat priors on both. We sample the \hat{g}_i linearly in the range $[0, 1]$, subject to the normalisation constraint of Eq. [?]. We perform the MCMC at a temperature $T = 2$ to ensure adequate exploration of the parameter space.

In order to obtain an estimate of parameters, we use the mean likelihood, as described in Chapter 3. We bin the parameter of interest and average the likelihood of all points within each bin. This mean likelihood is then smoothed on the width of the bins and the parameter value which maximises the mean likelihood is taken as a best estimate of the underlying parameter. In order to obtain parameter limits, we construct minimal credible intervals for the parameters of interest at the $p\%$ level. **This is all shite...Wait, am I actually using the marginalised PDF - yes, yes I am - rewrite!!! I'm using MAP! Why change?**

4.2.3 Results

Figure ?? shows the fitted values for the WIMP mass, m_{rec} , obtained from 250 mock datasets. This distribution shows a peak around 45 GeV, as well as a significant number of datasets reconstructed at ~ 100 GeV. As pointed out by Ref. [299], some mock datasets will not be representative

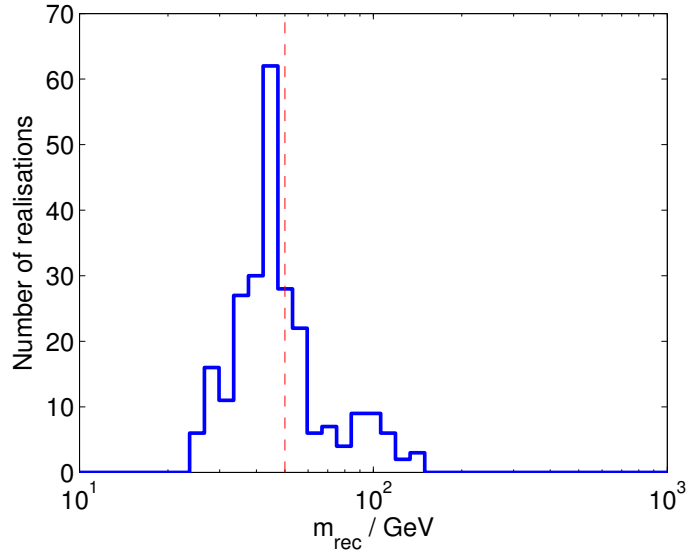


Figure 4.4: WIMP masses reconstructed using the binned speed parametrisation method from 250 realisations. The benchmark speed distribution is the SHM. The true mass of 50 GeV is shown as a dashed vertical line.

of the underlying benchmark parameters, having more events at high energies than expected, for example. This can lead to ‘bad’ reconstructions with a fitted WIMP mass higher than the benchmark value. Thus, the reconstructions near 100 GeV do not necessarily signify a failure of the reconstruction method.

However, a coverage study of 68% and 95% confidence intervals for this method shows significant under-coverage: $36 \pm 3\%$ coverage and $63 \pm 3\%$ coverage respectively for the two intervals. This indicates that while the mass reconstructions appear to be distributed close to the true value, the corresponding error estimates must be too small. *Actually write the coverage section in Chapter 3 - or just get rid of chapter 3 all together...?*

We can also assess the performance of the method by calculating the ‘pull’ statistic Δ (see e.g. Ref. [300]),

$$\Delta = \frac{m_{\text{rec}} - m_{\text{true}}}{\sigma}, \quad (4.11)$$

where m_{rec} and m_{true} are the reconstructed and true values of the WIMP mass respectively. An estimate of the uncertainty on m_χ is given by σ , which we estimate from the standard deviation of m_χ within a chain. The Δ statistic quantifies the statistical deviation of the reconstruction from the true value. For a large number of mock datasets, the distribution of

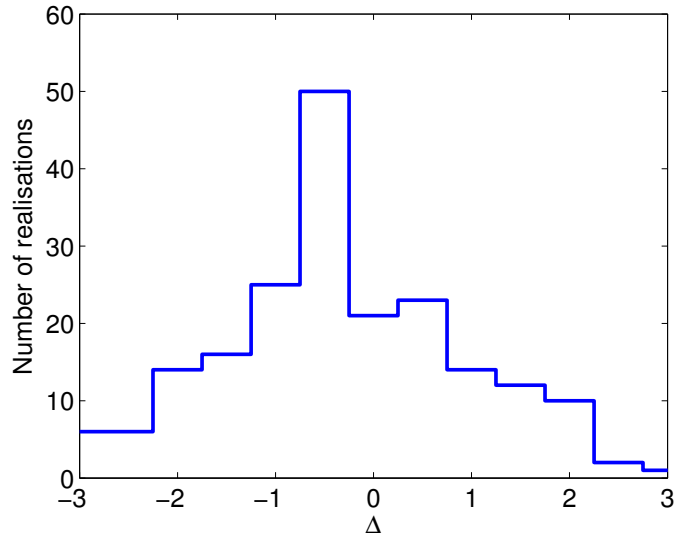


Figure 4.5: Distribution of the Δ statistic, defined in the text, for 250 realisations using the speed parametrisation method. The benchmark speed distribution is the SHM, with a 50 GeV WIMP.

Δ should have a mean of zero and a standard deviation of unity. **I'm actually using the marginalised distributions, am I?**

Figure 4.5 shows the Δ distribution for the 250 realisations of this method. The standard deviation of Δ is $\sigma_{\Delta} = 3.5$, which is significantly greater than unity, showing that the speed parametrisation method significantly underestimates the errors on reconstructed values. As demonstrated in Ref. [1], the problem of poor reconstructions using this method does not appear to be significantly improved by increasing the number of bins in the speed parametrisation and worsens for more complicated speed distributions.

Figure 4.6 shows the reconstructed speed distribution for a typical realisation using this method. The reconstructed mass value is $\log_{10}(m_{\text{rec}}/\text{GeV}) = 1.48 \pm 0.06$, compared to the benchmark value $\log_{10}(m_{\chi}/\text{GeV}) = 1.699$. The mean inverse speed is under-estimated in the range $0 - 200 \text{ km s}^{-1}$ and slightly over-estimated at higher speeds. However, the reduced m_{rec} increases the minimum accessible speed of the experiments, meaning that the experiments are less sensitive to the shape of the speed distribution at low speeds. Moreover, a reduced value of the reconstructed mass serves to steepen the spectrum, reconciling the flattened $\eta(v_{\text{min}})$ at high speeds with the data. This is because varying the mass of the WIMP ‘rescales’ the spectrum, due to the relation $E_{\text{R}} \propto \mu_{\chi N}^2 v_{\text{min}}^2$.

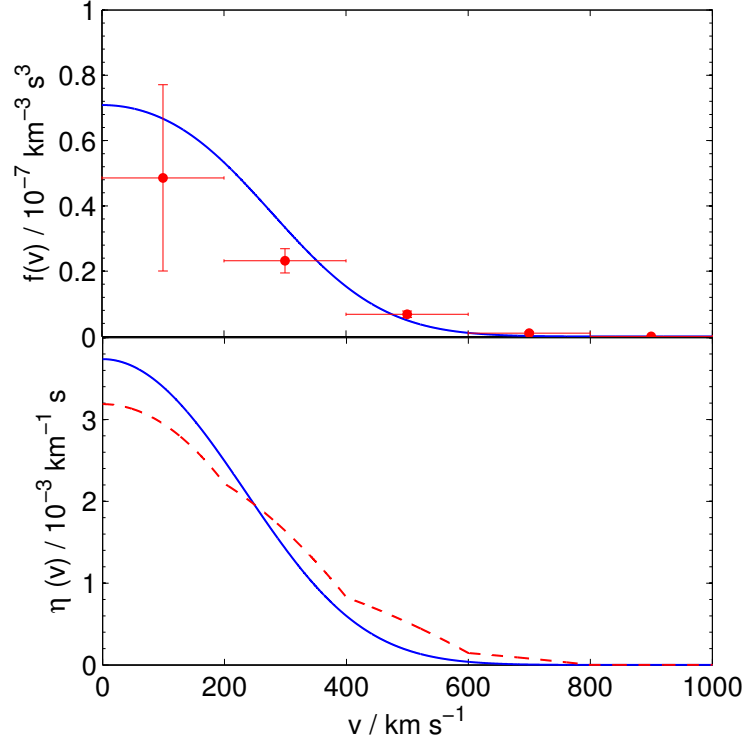


Figure 4.6: Reconstructed speed distribution, $f(v)$, and mean inverse speed, $\eta(v)$, using the speed parametrisation method. The benchmark model used was a 50 GeV WIMP with an SHM speed distribution. The upper pane shows the underlying SHM speed distribution (solid blue) and the fitted values of the speed bin parameters (red points). The errors on the bin values are within-chain standard deviations as described in the text. The lower pane shows the mean inverse speed corresponding to these fitted values (dashed red line) and the true mean inverse speed (solid blue).

In Fig. 4.7, we plot η/m_χ as a function of recoil energy, E_R , for the SuperCDMS-like experiment. We rescale η by $1/m_\chi$ because this factor appears in the event rate and we are then able to compare the spectra of events from different models. The solid line shows the mean inverse speed in the SHM, using the true WIMP mass of 50 GeV. We also show a binned approximation to the SHM (dashed line) obtained using the ‘true’ values of the bin parameters $\{g_i^{\text{approx}}\}$ and the true WIMP mass. Finally, we show the reconstructed mean inverse speed (dot-dashed line) using the reconstructed WIMP mass of 30 GeV. We see that the binned approximation to the SHM, which should represent a ‘good’ reconstruction, actually recovers the spectrum poorly compared to the reconstructed values. In particular, we note the energy range of the experiment spans two bins in the binned

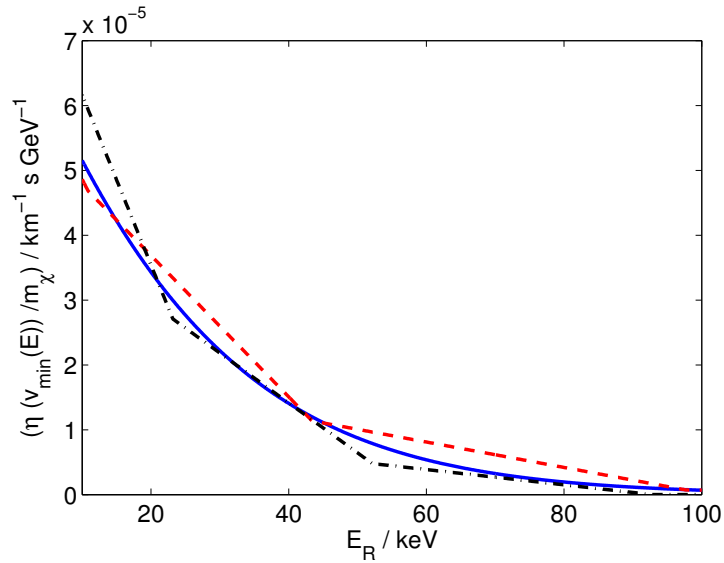


Figure 4.7: The rescaled mean inverse speed, η/m_χ , measured in the SuperCDMS-like experiment as a function of recoil energy, E_R . The same mock dataset was used as in Fig. 4.6. The underlying Standard Halo Model distribution (solid blue) uses the true WIMP mass of 50 GeV, as does the binned approximation to the SHM (dashed red). The reconstructed mean inverse speed (dot-dashed black) uses the reconstructed value of 30 GeV.

approximation to the SHM, but three bins in the MCMC reconstruction, allowing a closer approximation to the true spectrum.

Thus, the speed distribution parameters can be explored to provide a good fit to the data, with the reconstructed mass varying to compensate. As can be seen from Fig. 4.7, for a fixed bin width in velocity space, the size of bins in energy space can be reduced by moving to lower masses. This should allow a closer fit to the data and may explain why there appears to be a bias towards lower mass values.

4.3 Momentum parametrisation for a single experiment

When considering the speed distribution of the WIMPs, we see that each experiment has a different range of sensitivity and that varying the WIMP mass changes this range. However, we can instead consider a ‘reduced WIMP-nucleus momentum,’

$$\mathbf{p}_N = \mu_{\chi N} \mathbf{v}, \quad (4.12)$$

defined separately for each target nucleus. We now note that the accessible range in \mathbf{p}_N for each experiment is independent of the WIMP mass:

$$p_{\min}(E_R) = \mu_{\chi N} v_{\min}(E_R) = \sqrt{\frac{m_N E_R}{2}}. \quad (4.13)$$

We therefore rewrite the differential event rate in terms of the new momentum variable:

$$\frac{dR}{dE_R} = \frac{\rho_0 \sigma_p \mu_{\chi N}}{2 \mu_{\chi p}^2 m_\chi} A^2 F^2(E_R) \tilde{\eta}(p_{\min}), \quad (4.14)$$

where $\tilde{\eta}$ is the mean inverse *momentum* associated with the reduced momentum distribution, $\tilde{f}(\mathbf{p})$:

$$\tilde{\eta}(p_{\min}) = \int_{p_{\min}}^{\infty} \frac{\tilde{f}(\mathbf{p})}{p} d^3\mathbf{p} = \frac{1}{\mu_{\chi N}} \eta(p_{\min}/\mu_{\chi N}). \quad (4.15)$$

The event rate can be rewritten as:

$$\frac{dR}{dE_R} = \frac{\rho_0}{2} D(\sigma_p, m_\chi, m_N) A^2 F^2(E_R) \tilde{\eta}(p_{\min}), \quad (4.16)$$

where we have defined

$$D(\sigma_p, m_\chi, m_N) = \frac{\sigma_p \mu_{\chi N}}{\mu_{\chi p}^2 m_\chi}, \quad (4.17)$$

which encodes all information about the WIMP mass and cross-section and controls the overall scale of the event rate.

We can again define a directionally averaged momentum distribution, $\tilde{f}(p) = f(p/\mu_{\chi N})/\mu_{\chi N}^3$, and parametrise this in terms of 5 constant bins, with bin values $\{h_i\}$. We parametrise $\tilde{f}(p)$ only over the range of sensitivity of the experiment: $p \in [p_a, p_b]$, where $p_{a,b} = p_{\min}(E_{\min, \max})$. This means that we need not make any assumptions about the distribution function outside the range of sensitivity of the experiment. However, we still wish to impose some normalisation constraint on the momentum distribution parameters. Each experiment now probes a well-defined (but unknown) fraction of WIMPs, α_N , given by

$$\alpha_N = \int_{p_a}^{p_b} f(p) p^2 dp. \quad (4.18)$$

The momentum parameters are therefore normalised according to

$$\sum_{i=1}^N \hat{h}_i = \alpha_N, \quad (4.19)$$

where \hat{h}_i is defined analogously to \hat{g}_i in Eq. ???. We absorb the unknown α_N into D , such that the momentum distribution parameters, $\{\hat{h}_i/\alpha_N\}$, are normalised to unity and

$$D(\sigma_p, m_\chi, m_N) = \alpha_N \frac{\sigma_p \mu_{\chi N}}{\mu_{\chi p}^2 m_\chi}. \quad (4.20)$$

Finally, it is necessary to introduce a parameter A which models the constant contribution to η from WIMPs with momenta greater than p_b :

$$A = \int_{p_{\min}(E_{\max})}^{\infty} \frac{\tilde{f}(\mathbf{p})}{p} d^3\mathbf{p}. \quad (4.21)$$

Because the precise form of $\tilde{f}(p)$ above the upper energy threshold is undetermined by the experiment, the contribution of A to the normalisation, α_N , cannot be calculated and is therefore not considered. Instead, we include conservative constraints on A such that its contribution alone cannot exceed the normalisation of $\tilde{f}(p)$:

$$A < (p_{\min}(E_{\max}))^{-1}. \quad (4.22)$$

We also note that

$$\int_{p_a}^{p_b} \frac{\tilde{f}(\mathbf{p})}{p} d^3\mathbf{p} \leq \frac{\alpha_N}{p_b}, \quad (4.23)$$

and thus impose the following additional constraint on the parameters:

$$\frac{1}{\alpha_N} [\eta(p_a) - \eta(p_b)] \leq \frac{1}{p_b}. \quad (4.24)$$

We therefore perform parameter reconstructions using the parameters D , $\{h_i/\alpha_N\}$ and A/α_N . Because the fraction of high momentum WIMPs is expected to be relatively low, we sample the parameter A logarithmically, with a log-flat prior.

4.3.1 Results

We consider again a single set of benchmark parameters, namely a 50 GeV WIMP with an SHM speed distribution. We apply the momentum parametrisation to mock datasets from the WArP-like Argon experiment. The reconstructed D values, D_{rec} , are shown in Fig. ?? in units of $10^7 \text{ cm}^2 \text{ kg}^{-2}$. In all reconstructions, the posterior distribution is unimodal, having separate parameters to describe the scale (D) and shape ($\{h_i\}$) of the event rate. The number of reconstructions is peaked at the correct value, however, the

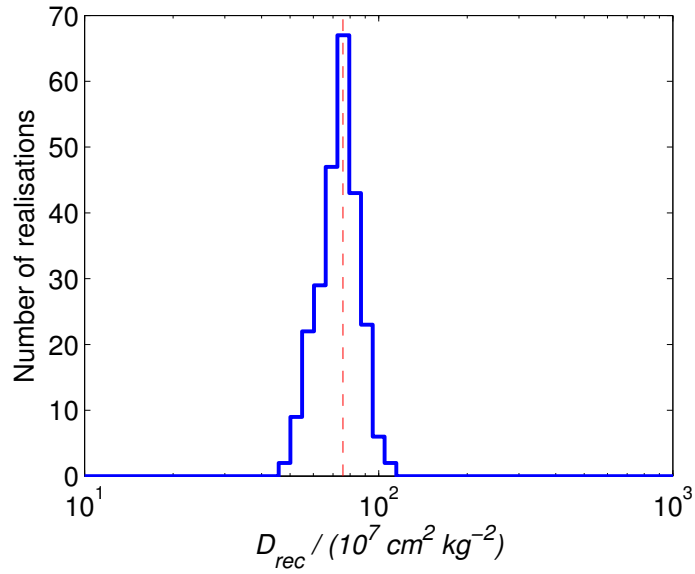


Figure 4.8: Reconstructed values for the scale parameter, D_{rec} , for the Argon experiment using the momentum parametrisation method from 250 realisations. The benchmark speed distribution is the SHM. The value of $D_{\text{true}} = 75.6 \times 10^7 \text{ cm}^2 \text{ kg}^{-2}$ is shown as a dashed vertical line.

distribution does not appear to be symmetric. In fact, the average reconstructed value is $\log_{10}(D)_{\text{rec}} = 1.865 \pm 0.004$, compared to the input value of $\log_{10}(D)_{\text{true}} = 1.878$. This represents a slight bias (of less than 1%) towards smaller values of $\log_{10}(D)$.

However, this is smaller than the typical statistical uncertainty in a single reconstruction, which is $\sim 4\%$. In addition, this method results in *overcoverage* of the true parameter, with values of $76 \pm 2\%$ and $98 \pm 1\%$ respectively for the 68% and 95% confidence intervals. This method therefore allows us to place reliable conservative estimates on the parameter D .

We show in Fig. ?? the reconstructed momentum distribution and mean inverse momentum for a typical realisation, for which the reconstructed D value is $1.81^{+0.09}_{-0.05}$. The underlying momentum distribution has been rescaled by $1/\alpha_{\text{Ar}}$ to allow a comparison to the reconstructed values. We see that the the momentum distribution is well reconstructed and the mean inverse momentum is accurately recovered at low and high momenta. In the middle of the momentum range, however, $\tilde{\eta}(p_{\text{min}})$ exceeds the true value. Because only a single experiment is being used, the measured spectrum is particularly susceptible to Poisson fluctuations. The mock dataset used here has a slight excess of events around $E_{\text{R}} \approx 60 \text{ keV}$, corresponding to

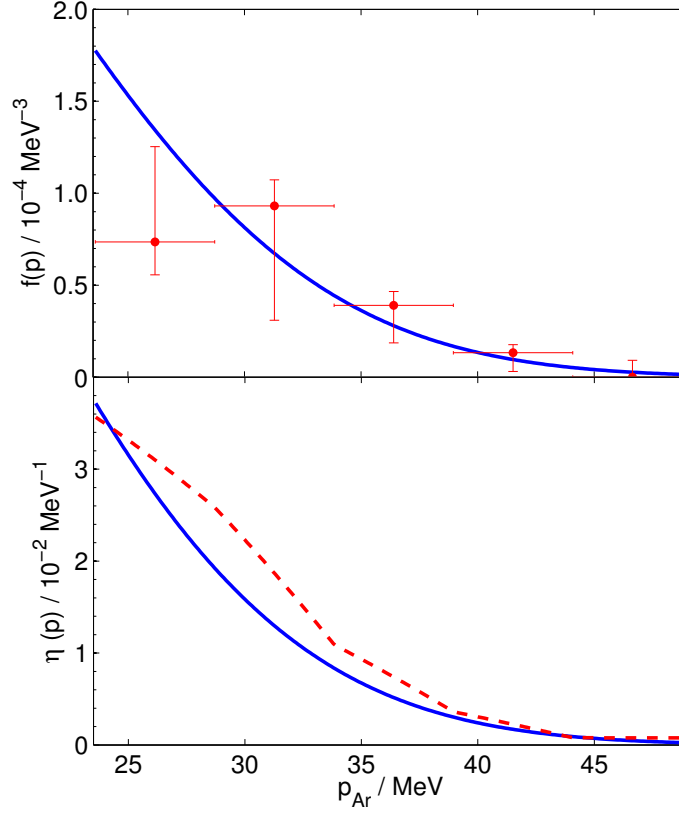


Figure 4.9: Reconstructed momentum distribution for a single Argon experiment using a benchmark of a 50 GeV WIMP and the SHM. The upper pane shows the SHM momentum distribution (solid blue) and reconstructed bin values (red points). Because the posterior is unimodal, we also display vertical errorbars showing the extent of the 68% confidence region for each bin. Note that these errors are strongly correlated. The lower pane shows the corresponding reconstructed mean inverse momentum (dashed red) and the mean inverse momentum in the SHM (solid blue). The underlying distribution has been rescaled by $1/\alpha_{\text{Ar}}$ for comparison to the reconstructed values.

$p_{\text{Ar}} \approx 30$ MeV, which may explain the reconstructed excess.

In addition, this may be a consequence of the particular parametrisation. The constant-bin parametrisation of $\tilde{f}(p)$ leads to a parametrised $\tilde{\eta}(p_{\min})$ which is concave downwards in each bin, while the underlying function is strictly convex downwards in this region. Thus, $\tilde{\eta}(p_{\min})$ tends to be slightly overestimated, leading the scale parameter D to be reduced to compensate for this. With datasets containing more events, the number of bins could be increased, in order to reduce this bias on D and maintain it at below the level of the statistical uncertainty.

4.4 Momentum parametrisation for several experiments

The reduced momentum method allows us to extract information from a single experiment, making no assumptions about the underlying velocity (or momentum) distribution. However, information about the mass and cross-section are encoded in the parameter, D , and cannot be extracted using a single experiment alone.

Because a different momentum variable p_N can be defined for each experiment, it is necessary to choose a single experiment and parametrise the momentum distribution defined with respect to that experiment. It may be necessary to adjust the lower and upper limits of the parametrisation (beyond the values of E_{\min} and E_{\max} used in the experiment) to accommodate as much of the data as possible from all experiments. In the single experiment considered in Section ??, the WIMP-Ar momentum was parametrised in the range $p_{\text{Ar}} \in [23.6, 49.2]$ MeV, to match the sensitivity of the Argon experiment. However, as can be seen in Fig. ??, this sensitivity window does not match that of the other experiments. If we extend this interval, and parametrise in the range $p_{\text{Ar}} \in [3.6, 53.0]$ MeV, we can enclose the sensitivity regions of all three experiments as closely as possible, as shown by the dotted curves in Fig. ?. We again use 5 bins in momentum space, with an additional parameter to control a constant offset.

In theory, any of the three experiments could have been chosen to define the momentum variable. However, some choices of experiment are less practical. For example, in order to use the XENON1T-like experiment, it would be necessary to parametrise the momentum over the range $p_{\text{Xe}} \in [11, 162]$ MeV. This is because at high WIMP masses the remaining two experiments have maximum accessible speeds of $\sim 500 \text{ km s}^{-1}$. This corresponds to very high values of the WIMP-Xe reduced momentum because of Xenon's comparatively higher mass. A large number of bins would be required to cover this wide momentum range and accurately model structures in the distribution function. Owing to the Galactic escape speed, many of these bins would have a value of zero, making parametrisation with respect to the XENON1T-like experiment a poor choice.

By comparison, using the WArP-like Argon experiment allows us to parametrise only as much of the momentum space as required to accom-

modate data from all three experiments. In the speed parametrisation method, the WIMP mass could be varied to adjust the range of speeds accessible to the experiments. This reduces the sensitivity of the likelihood to some of the speed bin parameters, meaning that these parameters can be adjusted with little effect on the likelihood value. This results in a spurious freedom in the remaining bin parameters, which can be varied to achieve a good fit to the data. As demonstrated in Sec. ??, this results in a bias towards lower values of the reconstructed WIMP mass in order to reduce the size of the bins in energy space. Using the momentum parametrisation method, we reduce this effect by ensuring that the likelihood is sensitive to all momentum bin parameters as much as possible, as the accessible speed range of the analysis tracks more closely the accessible speed range of the experiments. In addition, for a fixed bin width in momentum space, the bin width in energy space is much less sensitive to the WIMP mass.

Unfortunately, this method does not allow the WIMP-nucleon cross-section to be extracted; because the contributing WIMP fraction, α , is unknown, we can only obtain a lower bound. This is a fundamental limitation of any method which makes no assumptions about the underlying speed distribution. Without knowing the fraction of WIMPs with speeds within the signal window of the experiment, we cannot determine the cross-section. However, the cross-section appears in the event rate only through the degenerate combination $\sigma_p \rho_0$. As discussed in Sec. ??, estimates of ρ_0 typically carry a factor of around 2 uncertainty. Thus, any estimate of the WIMP-nucleon interaction cross-section would have an inherent uncertainty in any case.

4.4.1 Results

We first compare results for the momentum method to the speed parametrisation method presented in Section ??. We use the same mock datasets generated for the 50 GeV, SHM benchmark presented previously. The results of both the momentum and speed methods are shown in Fig. 4.10. In the case of the momentum method, the distribution of realisations is now more closely peaked around the true mass of 50 GeV. Furthermore, the momentum method produces substantially improved coverage properties, as summarised in Table 4.2. It should be noted that compared to the speed method, the momentum method leads to a larger number of reconstruc-

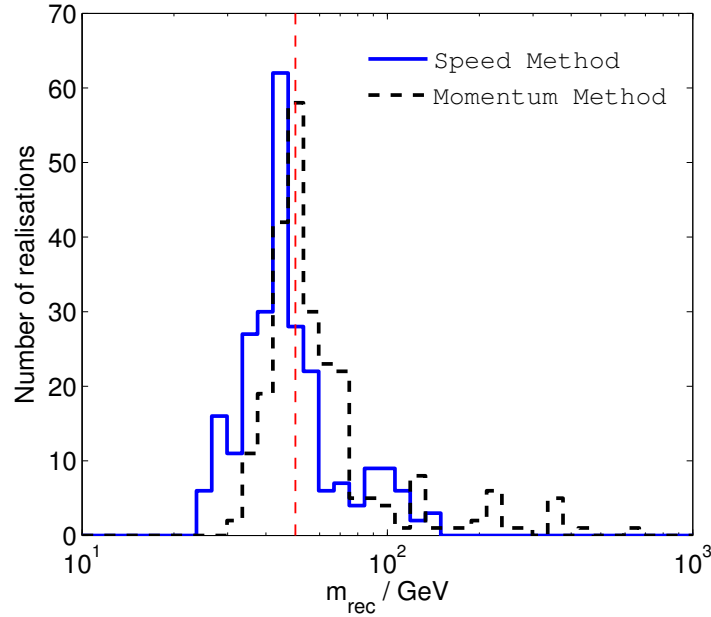


Figure 4.10: WIMP masses reconstructed using the speed and momentum parametrisation methods from 250 realisation. The benchmark speed distribution is the SHM. The true mass of 50 GeV is shown as a dashed vertical line.

tions at high WIMP mass. It is not clear whether this signals a failure of the momentum method in certain cases or whether these are representative of ‘bad’ reconstructions, as will be discussed shortly.

Fig. 4.11 shows the reconstructed WIMP-Argon momentum distribution using the same mock dataset as used for Fig. 4.6. The benchmark distributions have been rescaled by α so that they can be compared to the reconstructed values. In this case, $\alpha = 0.995$, so we can reconstruct both the mass and cross section accurately: $\log_{10}(m_{\text{rec}}/\text{GeV}) = 1.62 \pm 0.31$ and $\log_{10}(\sigma_p/10^{-47}\text{ cm}^2) = 2.99 \pm 0.18$, compared to the true values of $\log_{10}(m_{\text{true}}/\text{GeV}) = 1.699$ and $\log_{10}(\sigma_p/10^{-47}\text{ cm}^2) = 3.0$. While there is no way to know *a priori* whether α will be close to unity, the accurate reconstruction of the mass, cross-section and momentum distribution show that momentum parametrisation can offer a significant improvement over the speed parametrisation method.

We now present the results of the momentum method for a wider range of benchmarks. In order to ensure the robustness of the method, we use two possible WIMP masses of 50 GeV and 100 GeV **justify these values...**, as well as three benchmark models for the velocity distribution:

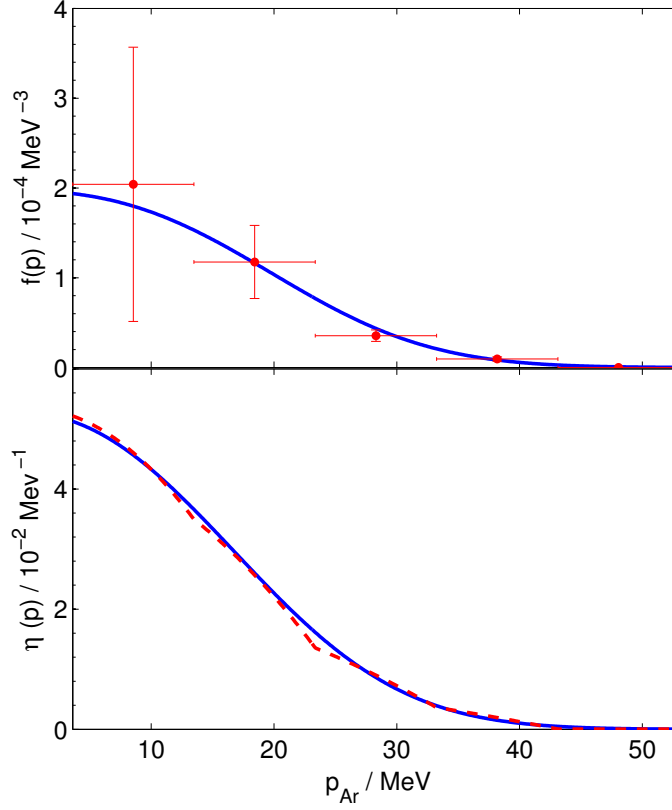


Figure 4.11: Reconstructed momentum distribution from all three mock experiments using a benchmark of a 50 GeV WIMP and the SHM. The upper pane shows the SHM momentum distribution (solid blue) and reconstructed bin values (red points). The errors on the bin values are within-chain standard deviations as described in Sec. ???. The lower pane shows the corresponding reconstructed mean inverse momentum (dashed red) and the mean inverse momentum in the SHM (solid blue). The reconstructed values have been rescaled by α for comparison to the true distribution.

	Speed Method	Momentum Method
68% Coverage	$36 \pm 3\%$	$71 \pm 3\%$
95% Coverage	$63 \pm 3\%$	$92 \pm 2\%$

Table 4.2: Coverage statistics for the speed and momentum parametrisation methods for a 50 GeV SHM benchmark model.

- (i) the Standard Halo Model (SHM), with $\sigma = 156 \text{ km s}^{-1}$ and $v_{\text{lag}} = 230 \text{ km s}^{-1}$;
- (ii) a 50% Standard Halo Model with a 50% contribution from a dark disk (DD);

(iii) rescaled Via Lactea II data (VL-2).

We model the dark disk velocity distribution as a Maxwellian with $\sigma = 50 \text{ km s}^{-1}$ and $v_{\text{lag}} = 60 \text{ km s}^{-1}$, similar to the typical values obtained by Ref. [301]. A 50% contribution from the dark disk is at the upper limit of the range presented by Ref. [?] and we consider this as an extreme case. The third benchmark is the distribution function as extracted from the Via Lactea 2 (VL-2) N-body simulation [302] and presented in Ref. [269]. It is averaged over galactic radius in the range $7.5 < R < 9.5 \text{ kpc}$ and measured in bins of width 10 m s^{-1} . VL-2 is a DM-only simulation and thus leads to a lower peak speed than the SHM. Including the effects of baryons should deepen the galactic potential and raise this peak speed closer to that observed in the Milky Way. In order for a fairer comparison, we therefore rescale the VL-2 data such that $f_3(v)$ peaks at the same speed as in the SHM, allowing us to probe the departures from Maxwellian form which appear in N-body simulations.

These benchmark velocity distributions are illustrated in Fig. 4.12. The VL-2 data has the flattest velocity distribution with a tail extending beyond 800 km s^{-1} . This leads to a flatter spectrum and a larger number of events at higher energies than for the other two benchmark models. The SHM distribution produces roughly the same number of events as the VL-2 distribution, but with fewer events at high energy. In the dark disk model, however, the value of v_{lag} is much smaller. This means that WIMPs typically have much lower speeds and many have insufficient energy to overcome the thresholds of the detector. This results in fewer observed events and a steeper recoil spectrum.

The distributions of reconstructed masses are shown in Fig. 4.13 for the 50 GeV WIMP and Fig. 4.14 for the 100 GeV WIMP. For the 50 GeV benchmark, the distribution of reconstructions is peaked at the true value, though in all three cases there are a number of datasets reconstructed at higher masses. For some of the mock datasets, the posterior distribution for the WIMP mass is multimodal, with a peak near the true value as well as a peak above $\sim 100 \text{ GeV}$. For reconstructions using a fixed speed (or momentum) distribution, these may correspond to ‘bad’ reconstructions, as mentioned previously, in which the spectrum of events is flatter than expected. When the momentum distribution is allowed to vary, as here, the event rate can be well fit by more than one region of the mass parameter

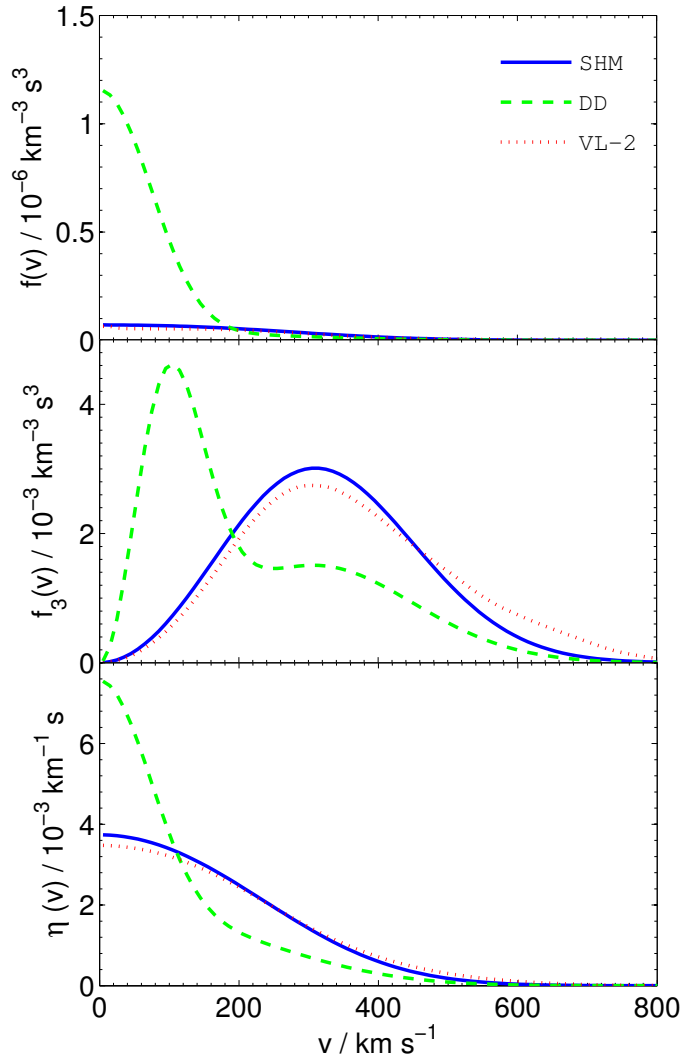


Figure 4.12: 1-D and 3-D speed distributions, $f(v)$ and $f_3(v)$, **Fix...** and mean inverse speed, $\eta(v)$, for the 3 benchmark speed models with parameter values as given in Sec. ?? : Standard Halo Model (SHM - solid blue), Standard Halo Model + Dark Disk (DD - dashed green) and Via Lactea 2 (VL-2 - dotted red). **Fix this notation...**

space. We also note a larger number of reconstructions at high masses in the case of the VL-2 benchmark. This is because of the flatter recoil spectrum in this case, which is more easily mimicked by a higher WIMP mass.

For the 100 GeV benchmark, the SHM and VL-2 models show similar structures, with a broad peak of reconstructions at or near the correct values, as well as a smaller tail up to masses of 1000 GeV, the upper limit of the prior. The 100 GeV datasets contain fewer events than their 50

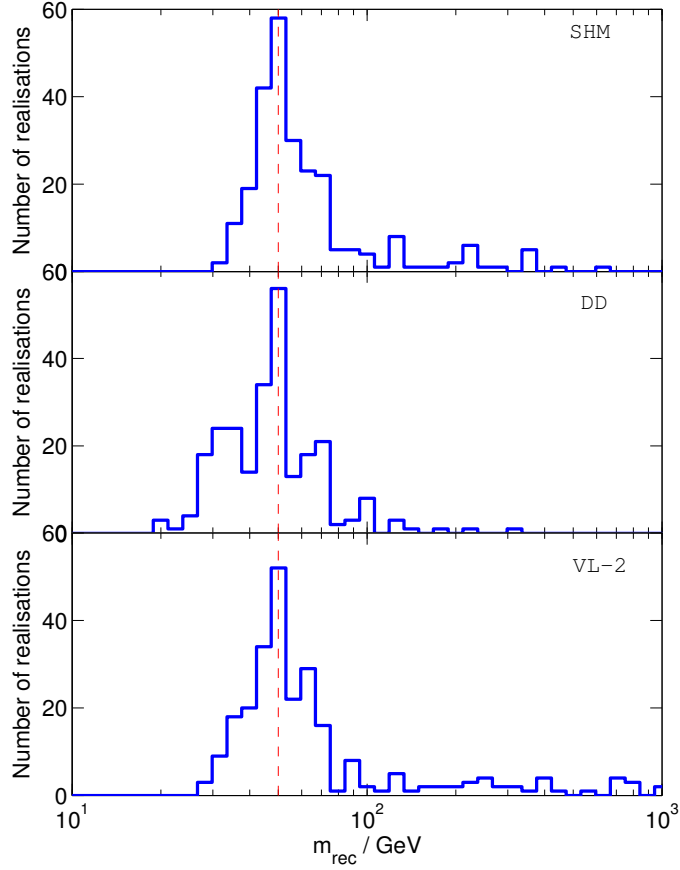


Figure 4.13: Distribution of reconstructed masses, m_{rec} , using the momentum method for 250 reconstructions. The true mass of 50 GeV is shown as a dashed vertical line.

GeV counterparts, so we would expect the spread of reconstructed values to be broader. Also, as previously noted, as the WIMP mass exceeds the mass of the target nucleus, the shape of the event spectrum becomes roughly independent of the WIMP mass. The largest nuclear mass used here is $A_{\text{Xe}} = 131$, meaning that for values of m_{rec} significantly above $m_{\chi} \approx 131 \text{ amu} \approx 122 \text{ GeV}$, the posterior distribution becomes roughly flat. Reconstructions in the high-mass tail occur when the maximum of the posterior occurs in this approximately flat region, and we expect the tail to extend up to arbitrarily high masses. In this case, we can only place a lower bound on the WIMP mass and when calculating coverage statistics, we use 1-tailed limits (i.e. a $p\%$ confidence limit encloses $\frac{1}{2}(1+p)\%$ of the marginalised posterior).

We report coverage statistics for the various benchmark parameters in Table 4.3. For the Standard Halo Model, there is approximately exact

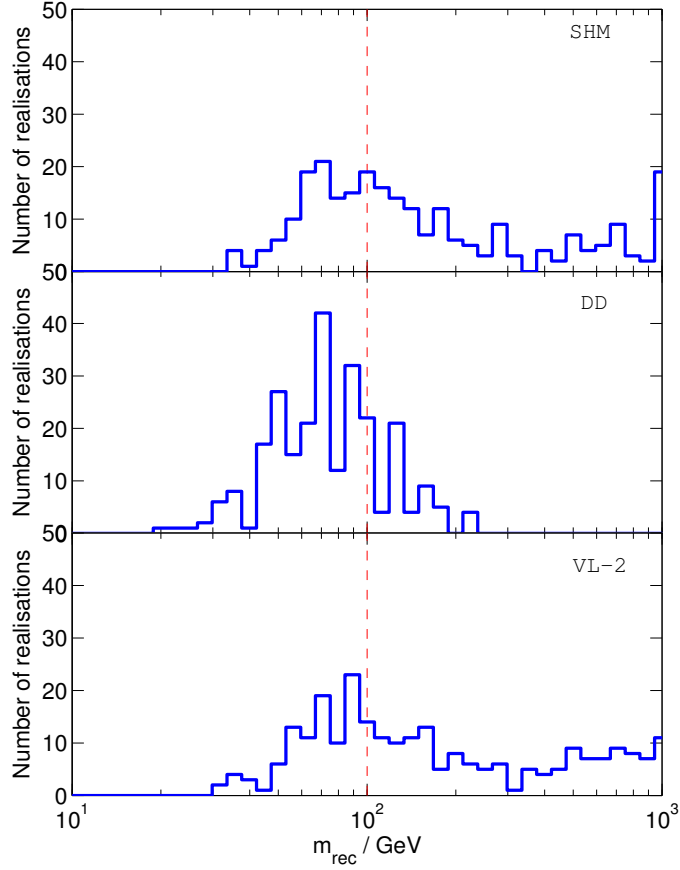


Figure 4.14: As Fig. 4.13 for $m_\chi = 100$ GeV.

coverage for both 50 and 100 GeV WIMPs, while for the VL-2 benchmark exact coverage is observed for the 100 GeV WIMP. The remaining benchmark parameters display some undercoverage, though still much improved over that achieved by the speed parametrisation method. The poorest coverage is achieved for the 100 GeV DD benchmark, for which the 68% confidence interval has a coverage of $58 \pm 3\%$. This is to be expected from the poorly distributed reconstructions shown in Fig. ???. For the 100 GeV dark disk benchmark, there appears to be a significant bias in the distribution of reconstructed values, which peaks around 70 GeV. We explore the origin of this bias in the next section, where we examine the speed distributions reconstructed using this method.

4.4.2 Recovering the speed distribution

We will now consider how the speed distribution can be reconstructed from the momentum parametrisation. For a set of constant bins in momentum

	WIMP Mass	
	50 GeV	100 GeV
SHM	$71 \pm 3\%$	$65 \pm 3\%$
	$92 \pm 2\%$	$94 \pm 1\%$
DD	$61 \pm 3\%$	$58 \pm 3\%$
	$94 \pm 1\%$	$91 \pm 2\%$
VL-2	$72 \pm 3\%$	$65 \pm 3\%$
	$90 \pm 2\%$	$94 \pm 2\%$

Table 4.3: 68% and 95% confidence interval coverage results for the momentum parametrisation method using a variety of benchmark parameters, as defined in Sec. ??.

space, the positions and widths of bins in velocity space is dependent on the WIMP mass. It is therefore difficult to extract precise statistical information on the speed distribution, as the bin values will be very strongly correlated with the WIMP mass. Instead, we take the reconstructed WIMP mass as fixed and use this to obtain a speed distribution from the momentum distribution parameters. Without treating the covariance of the WIMP mass and the bin parameters in full, the reconstructed speed distribution will depend strongly on the reconstructed mass value. However, this naive approach should give an indication of whether accurate reconstructions are possible.

First, we consider a 50 GeV WIMP with SHM distribution, as an archetypal WIMP model with a well-behaved distribution function. We show a typical reconstructed speed distribution in Fig. 4.15, using the same mock dataset as Fig. 4.11. In this case, the reconstructed value of m_{rec} is 42 GeV and the speed distribution appears to be accurately reconstructed within the error estimates.

Next, we consider a reconstruction for a 100 GeV WIMP with DD distribution function. One example is shown in the left-hand panes of Fig. 4.16, for a dataset with reconstructed mass $\log_{10}(m_{\text{rec}}/\text{GeV}) = 1.83 \pm 0.15$, compared to the true value of $\log_{10}(m_{\chi}/\text{GeV}) = 2$. The speed distribution appears to be well recovered at all speeds. However, there is a significant discrepancy in the mean inverse speed below $\sim 150 \text{ km s}^{-1}$. This is because the DD distribution function is very rapidly varying at low v , meaning that the ansatz of constant bins can no longer be applied. As observed in the

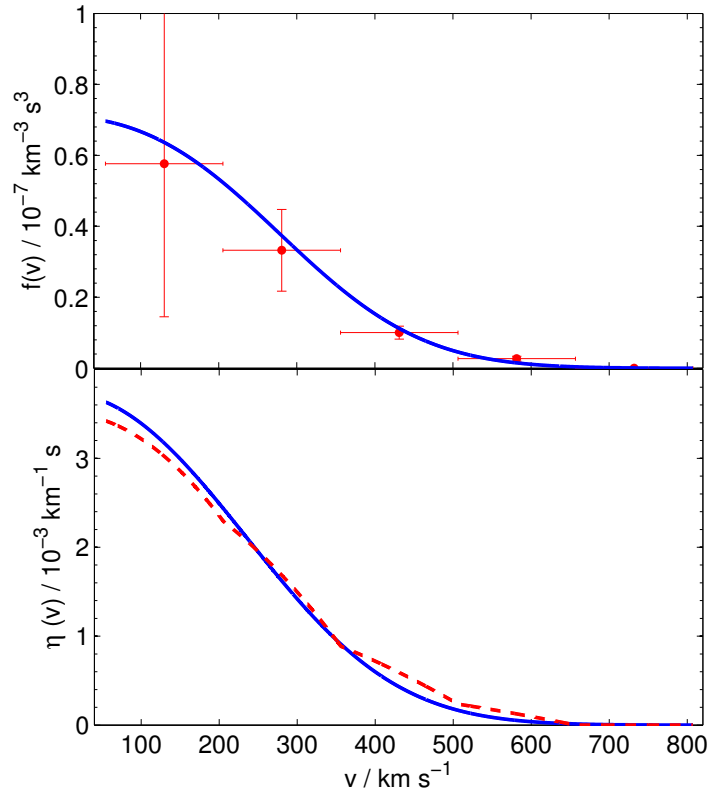


Figure 4.15: Reconstructed speed distribution from all three mock experiments using the momentum parametrisation method. The benchmark is a 50 GeV WIMP and the SHM distribution function. The upper pane shows the underlying SHM speed distribution (solid blue) and the fitted values of the speed bin parameters (red points). The errors on the bin values are within-chain standard deviations as described in Sec. ???. The lower pane shows the mean inverse speed corresponding to these fitted values (dashed red line) and the true mean inverse speed (solid blue). The underlying distributions have been rescaled by α for comparison to the reconstructions.

speed parametrisation method, the event spectrum can be steepened by moving to lower mass values and this may explain why there is significant bias and poor coverage for this set of benchmark parameters.

In the right-hand panes of Fig. 4.16, we show results from the same mock dataset reconstructed using 7 bins in momentum space. The reconstructed mass is now $\log_{10}(m_{\text{rec}}/\text{GeV}) = 2.21 \pm 0.27$, with the mean inverse momentum more closely reconstructed than for the 5 bin case. Figure 4.17 shows the distribution of reconstructed masses for a 100 GeV WIMP with a DD distribution function using 7 bins in momentum space. The reconstructed masses are now more broadly distributed around the benchmark

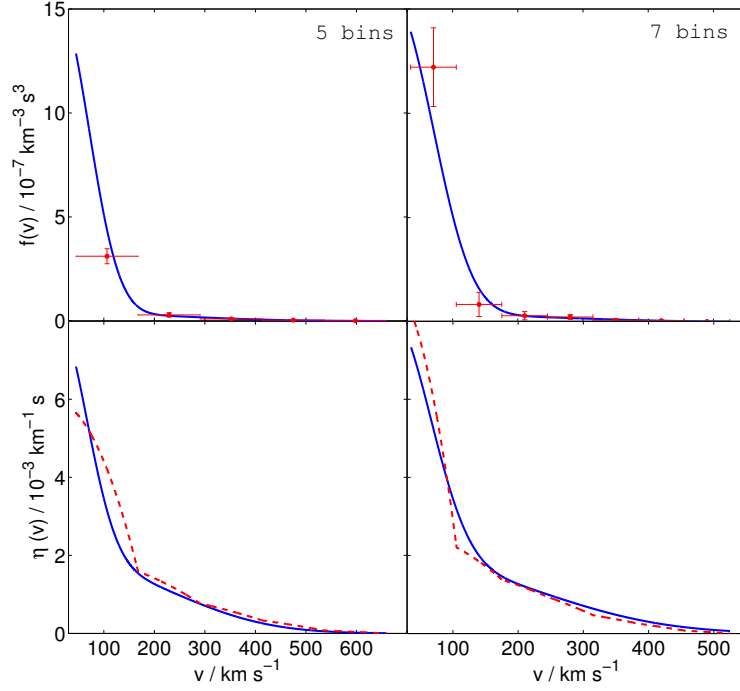


Figure 4.16: As Fig. 4.15 for a 100 GeV WIMP with DD distribution function using 5 momentum bins (left panes) and 7 momentum bins (right panes).

value, with improved coverage compared to the 5 bin case: $67 \pm 3\%$ and $94 \pm 1\%$. We have found that increasing the number of bins for the 50 GeV SHM benchmark leaves the coverage properties and distribution of reconstructions largely unchanged, indicating that increasing the number of bins can be used to check the robustness of the reconstructions.

Finally, we consider the discriminatory power of the reconstructions. Returning to the 50 GeV SHM benchmark, we plot a single speed distribution reconstruction in Fig. 4.18, as well as all three benchmark speed distributions for comparison. The reconstruction is reasonably consistent with both the SHM and VL-2 models and displays only mild tension with the DD model. In addition, the benchmark distributions in Fig. 4.18 have been rescaled by the true value of α for comparison with the reconstructed values. In a real experiment, the value of α is unknown, further reducing the potential to discriminate between different models. Only in the case of more extreme distribution functions, such as a dark disk, might it be possible to make a distinction between the many possible underlying models. Thus, while the momentum parametrisation method can provide good constraints on the mass of the WIMP, it remains difficult to probe

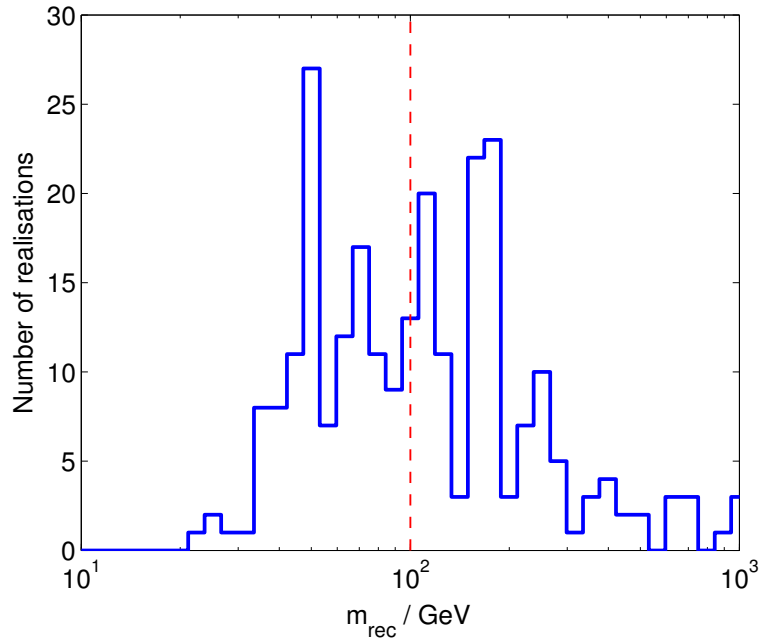


Figure 4.17: Distribution of reconstructed masses using the 7-bin momentum method for 250 reconstructions for a DD benchmark distribution. The true mass of 100 GeV is shown as a dashed vertical line.

the speed distribution function.

Need to include the section about spreading for $m_\chi \gg m_N$...

4.5 Discussion

We have explored the simple, empirical parametrisation proposed by Peter and showed that it produces a significant bias and underestimates the errors on m_χ , even for simple benchmarks. **Lower m_χ leads to higher v_{\min} - we can sort of stop that using the momentum method...** This appears to be due to the dependence of $\eta(E_R)$ on m_χ . For a fixed bin width in v , reducing the WIMP mass produces leads to smaller bins in E_R . This means that $\eta(E_R)$ can provide a better fit to the observed data.

As an alternative we have proposed binning the *momentum* distribution. For a single experiment, the inverse momentum distribution $\tilde{\eta}(E_R)$ is independent of the WIMP mass and the scale (controlled by the parameter D of Eq. ??) and shape of the recoil distribution can be effectively decoupled. This allows D to be reconstructed with minimal bias. The D values from many different experiments can then potentially be used to place bounds on the values of the WIMP mass and cross-section.

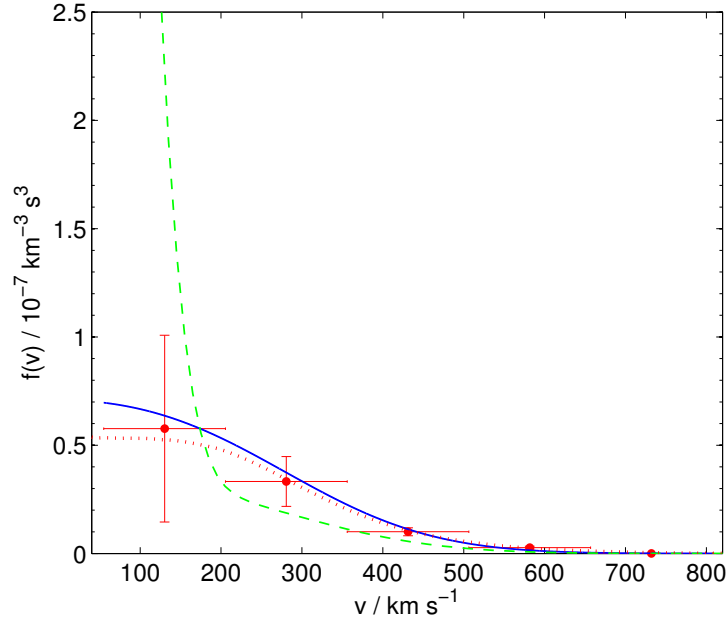


Figure 4.18: Reconstructed speed distribution from all three mock experiments using a benchmark of a 50 GeV WIMP with SHM distribution. The reconstructed values have been rescaled by α for comparison to the true distribution. The three different benchmark speed distributions defined in Sec. ?? have been overlaid: SHM (solid blue), DD (dashed green) and VL-2 (dotted red).

However, to directly constrain the WIMP mass, it is necessary to combine data from multiple experiments simultaneously. This is done by parametrising the reduced momentum distribution of the WIMPs with respect to only one of the experiments. In this work, we choose to parametrise $p_{\chi Ar}$. The result is that the shape of the recoil spectrum depends only weakly on the WIMP mass. This is because the recoil energy can now be written as

$$E_R = \frac{2p_{\chi Ar}^2}{m_N} \left(\frac{\mu_{\chi N}}{\mu_{\chi Ar}} \right)^2. \quad (4.25)$$

For a fixed bin width in $p_{\chi Ar}$, the bin width in recoil energy now scales with $\mu_{\chi N}^2/\mu_{\chi Ar}^2$, which has a weaker dependence on m_χ than when we consider fixed bins in v . This reduces the bias induced in the reconstructed WIMP mass. **Plot?**

The momentum method also allows us to probe a more constrained range of speeds. This is done by parametrising $p_{\chi Ar}$ only over the range to which the experiments are sensitive. While this cannot be done exactly

for more than one experiment, it means that as many of the momentum bin parameters as possible contribute to the rate. This reduces the spurious freedom which comes from varying bin parameters which lie below (or above) the sensitivity range of the experiment and therefore do not contribute to the rate. **Improve explanation...** This is similar to the method of Drees and Shan [282], which uses an algorithm to attempt to match the sensitivity ranges of multiple experiments.

Unfortunately, for low WIMP masses the range of speeds (and therefore momenta) probed by each experiment grows rapidly (see Fig. 4.3). A significant portion of this range is expected to be significantly higher than the maximum expected WIMP speed of $\sim 800 \text{ km s}^{-1}$. If we hope to parametrise the entire range of sensitivity of the experiments, this means that only a very small fraction of this range will be non-zero. A very large number of bins would be required to capture this ‘low’ momentum population (as discussed briefly in Sec. 4.4 for the case of a Xenon experiment). Thus, the momentum binning method appears not to be feasible for low mass WIMPs.

You can’t really apply the momentum distribution to other things, like IceCube...

Finally, while the momentum bin parametrisation provides significant improvements in coverage and reduced bias over the speed bin parametrisation, it does not work in every scenario. For example, the method still suffers from some under-coverage for more extreme distribution functions, such as the dark disk. This can be improved by increasing the number of bins, at the cost of significantly widening the range of reconstructed masses. These residual problems mean that the momentum binning method should be applied with caution. **Improve...**

4.6 Conclusion

We have presented a new method of analysing direct detection data sets which aims to reconstruct as much information as possible about the WIMP mass, cross-section and distribution function while making no assumptions about the shape of the underlying speed distribution. To do this, we parametrise the WIMP momentum distribution using a simple empirical parametrisation. This ensures that we do not parametrise those regions of velocity space to which the experiments are not sensitive, thus preventing

spurious reconstructions, as seen previously in the use of speed parametrisation methods. We have also seen that the binned speed parametrisation introduces a fixed scale (the bin width) into the distribution function. Converting from speed bins to energy bins depends on the WIMP mass, introducing a bias into the analysis. The momentum parametrisation should reduce this dependence and consequently reduce the bias introduced.

In the case of a single experiment, this method can be applied exactly and allows one to extract information about the shape of the distribution function, at the cost of losing access to information about either the WIMP mass or cross-section separately. For multiple experiments, the range of the parametrisation must be extended to cover the sensitivity regions of all experiments. For estimation of the WIMP mass, this allows us to achieve significant improvements in coverage and reduction in bias over previous methods. Without making any assumptions about the WIMP speed distribution, however, we cannot estimate the interaction cross-section due to its degeneracy with the fraction of WIMPs accessible to the experiments. This is an unavoidable problem, but is rendered somewhat irrelevant by large uncertainties in the local DM density.

Reconstruction of the WIMP speed distribution remains difficult. The finite sensitivity window of direct detection experiments means that information on the normalisation of $f(v)$ is lost, making comparison to theoretical models difficult. At the event rates studied here, it does not appear to be possible to distinguish between different distribution functions.

This technique represents a significant step towards developing model-independent methods for determining the WIMP mass. However, caution must be exercised, as the method is expected to perform poorly for low mass WIMPs, where the range of momenta probed by the experiments is large. There is also evidence that residual bias may remain, especially in the case of more extreme distribution functions.

Try not to repeat yourself...

Chapter 5

A polynomial parametrisation of the speed distribution

Include some plots that explicitly show the cross section degeneracy...

In an attempt to mitigate astrophysical uncertainties in the analysis of direct detection experiments, a number of parametrisations for the WIMP speed distribution have been proposed. In Chapter 4, we explored two such empirical parametrisation which aim to fit $f(v)$ without making any *a priori* assumptions about its form. These methods involved writing the WIMP speed distribution and momentum distribution as a series of constant bins.

However, the introduction of a fixed scale, in the form of the bin width, results in a bias in the reconstruction of the WIMP mass. While binning the momentum rather than speed distribution helps to reduce this problem, there may remain residual bias. Furthermore, the method is expected to fail for low mass WIMPs and the choice of momentum range to parametrise may not always be clear.

In this chapter, we propose an alternative parametrisation for the speed distribution which is smooth and can fit a wide range of possible functional forms of $f(v)$. This method involves parametrising the *logarithm* of $f(v)$ as a polynomial in the WIMP speed v . We describe the parametrisation in detail in Sec. 5.1.

We test the parametrisation, as in Chapter 4, using mock data sets from future experiments, generated from a range of particle physics and astrophysics benchmarks, outline in Sec. 5.2.2. We show in Sec. 5.4, that the parametrisation allows an unbiased reconstruction of the WIMP mass, even when Poisson noise and realistic experimental parameters are incor-

porated into the analysis. We show the performance of the method as a function of WIMP mass and also outline how to determine the optimal number of basis functions for the polynomial parametrisation.

Finally, in Sec. ??, we show how the speed distribution can be reconstructed using this parametrisation. A lack of information about the normalisation of $f(v)$ impairs our ability to reconstruct the absolute value of $f(v)$. However, we propose a method for reconstructing the *shape* of the mean inverse speed $\eta(v_{\min})$ even when information about the overall normalisation is not available.

5.1 Parametrising the logarithm of $f(v)$

We would like to write down a smooth, general parametrisation for the free function $f(v)$. However, the speed distribution is subject to two constraints in order to qualify as a physical distribution function:

- (i) $f(v)$ must be normalised (or at least should be capable of being normalised), and
- (ii) $f(v)$ must be everywhere greater than or equal to zero.

Motivated by the (ii), we propose parametrising the *natural logarithm* of the speed distribution. The properties of the logarithm will ensure that the speed distribution remains everywhere positive. Moreover, logarithmic dependence on the parameters means that a wide range of shapes for the speed distribution can be spanned by the parametrisation.

We parametrise $\ln f(v)$ as a polynomial in v . That is, we wish to write

$$\ln f(v) = \sum_{k=0}^{N-1} a_k P_k(v), \quad (5.1)$$

meaning that

$$f_1(v) = v^2 \exp \left(\sum_{k=0}^{N-1} a_k P_k(v) \right), \quad (5.2)$$

where we use N polynomial basis functions $P_k(v)$, multiplied by the coefficients a_k . Normalisation is imposed by fixing a_0 once the remaining parameters have been chosen. By using enough basis functions for the polynomial parametrisation, we can approximate any smooth, bounded function arbitrarily well [], so this choice provides complete generality. However, which

polynomial basis should be used? We see immediately that a naive power series of the form

$$\ln f(v) \approx a_0 + a_1 v + a_2 v^2 + a_3 v^3 + \dots, \quad (5.3)$$

is not practical for the purposes of parameter estimation. Higher powers of v will have rapidly growing contributions to $\ln f$, meaning that the associated coefficients must be rapidly decreasing in order to suppress these contributions. Fitting to the SHM using just 5 terms, the range of values for the a_k in the case of a simple power series would span around 13 orders of magnitude. Ideally, we would like to specify an identical prior on each of the coefficients. However, in this scenario this would result in a highly inefficient exploration of the parameter space when some of the terms are so small.

This problem can be significantly improved by rescaling v . We choose to rescale by a factor of $v_{\max} = 1000 \text{ km s}^{-1}$, and cut off the distribution function at v_{\max} . We should choose v_{\max} to ensure that $f_1(v)$ is negligible above the cut off. However, too high a choice of v_{\max} will result in $f_1(v)$ being close to zero over a large range of the parametrization, making fitting more difficult. We use the value $v_{\max} = 1000 \text{ km s}^{-1}$, which lies significantly above the Galactic escape speed. The basis functions $(v/v_{\max})^k$ are now less than unity by construction and the coefficients a_k are now dimensionless:

$$\ln f(v) \approx a_0 + a_1 (v/v_{\max}) + a_2 (v/v_{\max})^2 + a_3 (v/v_{\max})^3 + \dots \quad (5.4)$$

We now address the problem of *conditioning* of the polynomial basis (see e.g. Refs. [303, 304]). Conditioning is a measure of how much the value of a polynomial changes, given a small change in the coefficients. For a well-conditioned polynomial, small changes in the coefficient are expected to lead to small changes in the value of the polynomial. This is ideal for parameter estimation as it leads to a more efficient exploration of the parameter space. Orthogonal polynomial basis functions typically have improved conditioning [303] and we consider two specific choices: the Legendre polynomials and the Chebyshev polynomials. The Legendre polynomials are a familiar series of orthogonal basis functions. The Chebyshev polynomials are used extensively in polynomial approximation theory [305] and are expected to be well conditioned [303]. We examine both which polynomials perform best and how many basis functions are required in Sec. 5.3.1.

We plot in Fig. 5.1 some examples of distribution functions which can be described by the polynomial $\ln f(v)$ parametrisation with $N = 5$ basis functions. These examples were generated by randomly picking values for the $\{a_i\}$ values. However, we wish to determine how well we can *fit* these parameters, along with the WIMP mass and cross section, to data. As in the case of the binned distribution of Chapter 4, we now define a series of theoretical and experimental benchmarks which we use to generate mock data sets and test the parametrisation.

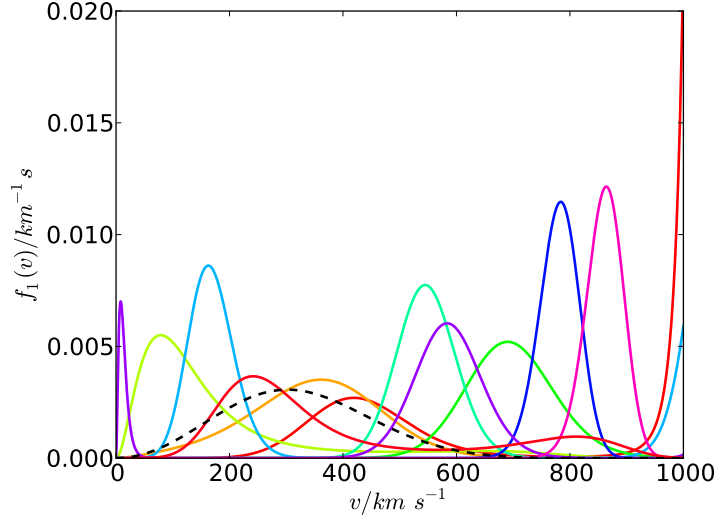


Figure 5.1: Examples of speed distributions $f_1(v)$ generated using the polynomial parametrisation for $\ln f(v)$ with $N = 5$ basis functions. The SHM distribution function in the Earth frame is shown as a black dashed line for comparison.

5.2 Parameter reconstruction

5.2.1 Experimental benchmarks

I can probably shorten this section... Maybe put all the experimental stuff in one place... In order to generate mock data sets, we consider three idealized mock experiments, loosely based on detectors which are currently in development. The three target materials we consider here are Xenon, Argon and Germanium. We describe each experiment in terms of its nucleon number A , fiducial detector mass m_{det} , efficiency ϵ and energy sensitivity

Experiment	Target Mass, A	Detector Mass (fid.), m_{det}/kg	Efficiency, ϵ	Energy Range/keV
Xenon	131	1100 [212]	0.7 [210]	7-45 [306]
Argon	40	1000	0.9 [307]	30-100 [308]
Germanium	73	150 [309]	0.6 [310]	8-100 [310]

Table 5.1: Summary of experimental parameters used in this work, defined in Sec. 5.2.1. An exposure of $t_{\text{exp}} = 2$ years is used for all 3 experiments.

window $[E_{\min}, E_{\max}]$. **I don't use an 'efficiency in Chapter 4. Why not? Unify them...**

We incorporate the effects of detector sensitivity, analysis cuts and detector down-time into the value of the efficiency ϵ , which we take to be energy independent for simplicity. We consider a total exposure time for all experiments of $t_{\text{exp}} = 2$ years. The experimental parameter values used in this chapter are summarized in Tab. 5.1. We note that these values may be slightly adjusted or updated compared to those used in Chapter 4 as a result of updated experimental results and projections. We have tried to indicate the source of the values used in Tab. 5.1.

The exact parameter values we used in this work do not strongly impact the results we present. However, it is important to note that the total mass and exposure of the experiments will affect the total number of events observed. This in turn will affect the precision of the reconstructions. For example, we have chosen a total Argon mass of 1000 kg. This is the stated target for Argon-based experiments which are in development (e.g. Ref. [183]), though at present typical fiducial masses for Argon prototypes are of the order of 100 kg [308]. The data we have generated does not represent the 'high-statistics' regime: across all three experiments the total number of events observed is roughly 200-300 with as few as 10 events in the Germanium detector for some scenarios. Using a smaller exposure (or equivalently a smaller interaction cross section) will reduce the precision of the results, but should not introduce any additional bias. We also briefly consider the impact of a *larger* number of events in Sec. 5.6.

5.2.2 Theoretical benchmarks

As in Chapter 4, we assume that SI interactions dominate and use a single value of the interaction cross section $\sigma_p^{\text{SI}} = 10^{-45} \text{ cm}^2$. However, we will consider a range of WIMP masses from 10 GeV, below which the sensitivity of current direct detection experiments decreases dramatically, up to 1000 GeV above which sensitivity to the precise WIMP mass is lost. *Talk at some point about the degeneracy and refer back to it.*

We consider several benchmark speed distributions in this work, including the SHM and the SHM with the addition of a moderate dark disk which accounts for 23% of the total WIMP density [30]. For the SHM, we assume a fixed DM density of $\rho_0 = 0.3 \text{ GeV cm}^{-3}$. However, we treat the dark disk as an overdensity contributing an *additional* WIMP population, bring the local density up to $\rho_0 = 0.39 \text{ GeV cm}^{-3}$ **Justify...** We model the speed distributions as combinations of Gaussian functions in the Earth frame

$$g(\mathbf{v}) = N \exp\left(-\frac{(\mathbf{v} - \mathbf{v}_{\text{lag}})^2}{2\sigma_v^2}\right) \Theta(v_{\text{esc}} - |\mathbf{v} - \mathbf{v}_{\text{lag}}|), \quad (5.5)$$

where \mathbf{v}_{lag} specifies the peak velocity of the distribution in the Earth frame and σ_v the velocity dispersion. We truncate the distribution above the escape speed $v_{\text{esc}} = 544 \text{ km s}^{-1}$. In addition, we also use the speed distribution of Lisanti et al. [265], which has the following form in the Earth's frame:

$$f(\mathbf{v}) = N \left[\exp\left(\frac{v_{\text{esc}}^2 - |\mathbf{v} - \mathbf{v}_0|^2}{kv_0^2}\right) - 1 \right]^k \Theta(v_{\text{esc}} - |\mathbf{v} - \mathbf{v}_0|). \quad (5.6)$$

We use the parameter values $k = 2$ and $v_0 = 220 \text{ km s}^{-1}$ in this work. We summarize in Tab. 5.2 the different speed distributions considered. We also plot several of these in Fig. 5.2 for reference. **NB:Time dependence...**

5.2.3 Parameter sampling

The parameter space of the speed distribution parameters is now much larger and is poorly explored using conventional MCMC methods. We therefore make parameter inferences using the MultiNest nested sampling package described in Chapter 3. We summarize the priors used in this work in Tab. 5.3. We also summarize in Tab. 5.4 the MultiNest sampling parameters used.

Speed distribu- tion benchmark	Fraction	$v_{\text{lag}}/\text{km s}^{-1}$	$\sigma_v/\text{km s}^{-1}$
SHM	1	220	156
SHM+DD	0.77	220	156
	0.23	50	50
Stream	1	400	20
Bump	0.97	220	156
	0.03	500	20
Double-peak	0.5	200	20
	0.5	400	20
Lisanti et al.	$v_0 = 220 \text{ km s}^{-1} \quad k = 2$		

Table 5.2: Summary of speed distribution benchmarks used in this work. Some benchmarks are modelled as mixtures of two gaussian components (defined in Eq. ??), for which we give the fractional contribution of each component (labelled ‘Fraction’). The remaining parameters are defined in Eqs. ?? and ?? and the accompanying text. The ‘bump’ and ‘double-peak’ distributions are discussed in Sec. 5.3.1.

Parameter	Prior type	Prior range
m_χ/GeV	log-flat	$[10^0, 10^3]$
σ_p/cm^2	log-flat	$[10^{-46}, 10^{-42}]$
$\{a_k\}$	linear-flat	$[-50, 50]$
R_{BG}/dru	log-flat	$[10^{-12}, 10^{-5}]$

Table 5.3: Summary of the priors on the parameters used in this work. The background rate R_{BG} is defined in Sec. 5.4 while the $\{a_k\}$ are the polynomial coefficients used in the parametrisation.

In Sec. 5.5 and Sec. 5.6, we consider many realisations of data, including the effects of Poisson noise. We therefore use the unbinned likelihood of Eq. 3.22 in MultiNest. As in Chapter 4, make parameter inferences from the marginalised posterior distribution **What’s the symbol**. We take the mode of the distribution to be the reconstructed parameter value and construct p% *minimal* credible intervals. This method performs well for small numbers of observations (compared to the number of free parameters in the fit). It is therefore a sensible choice here, where in some cases the number of events observed in an experiment is less than 10. **Reorder**

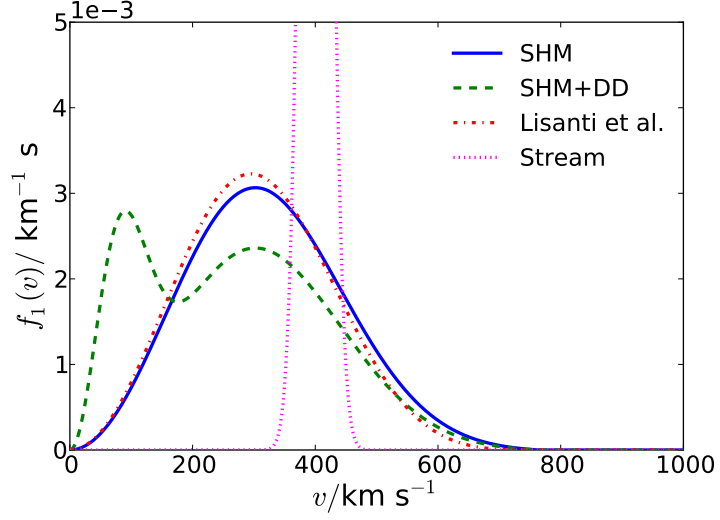


Figure 5.2: Several of the benchmark speed distributions used in this work. They are defined in Eqs. 5.5 and 5.6 with parameters from Tab. 5.2. These distributions are the SHM (solid blue), SHM+DD (dashed green), Lisanti et al. (dot-dashed red) and the stream (dotted magenta).

Parameter	Value
N_{live}	10000
efficiency	0.25
tolerance	10^{-4}

Table 5.4: Summary of the MultiNest sampling parameters used in this work.

these paragraphs...?

In Sec. 5.3.1 and Sec. 5.4, we consider the effects of varying the form of the parametrization and of varying the input WIMP mass. In order to eliminate the effects of Poisson noise, we use Asimov data [311] for these sections. This means that we divide the energy window of each experiment into bins of width 1 keV. We then set the observed number of events $N_o^{(i)}$ in bin i equal to the expected number of events $N_e^{(i)}$ and use the binned likelihood described by Eq. 3.21. Here, we have a very large number of observations, namely the exact (non-integer) event numbers in each energy bin. We can therefore use the best fit point as the reconstructed value and construct confidence intervals using the asymptotic properties of the profile likelihood, as described in Sec. 3.2.1.

Parametrisation	Reconstructed mass (GeV)
Polynomial $\ln f(v)$	$44.7^{+6.9}_{-3.6}$
Binned $f(v)$	$29.3^{+0.4}_{-1.0}$
Binned $\tilde{f}(p)$	$38.2^{+1.6}_{-2.3}$

Table 5.5: Reconstructed mass using the parametrization presented in this chapter, as well as the the speed binning and momentum binning methods of Chapter 4 for comparison. The benchmark used is a stream distribution function described in **Somewhere!** and a 50 GeV WIMP. In all cases, 5 speed distribution parameters (either bins or basis coefficients) are used.

5.3 Results

Mention the stream distribution somewhere

Mention the priors on a - and widening them...

Before we consider in detail the properties of the parametrisation (including performance as a function of number of basis functions and as a function of input mass), we show some reconstructions using a small numbers of benchmarks. *Show an example - in particular with the σ_p^{SI} degeneracy - to say that it works - need to show that first. Can't necessarily use the Peter review ones - too many experiments, too few Nlive and not enough basis functions...*

We compare the performance of the polynomial $\ln f(v)$ presented here with the binned distribution functions of the previous chapter. We use a 50 GeV WIMP with a stream distribution function **defined where?** and, using a single realisation of data, attempt to reconstruct the WIMP mass using each method. The results are shown in Table 5.5. The polynomial $\ln f(v)$ method shows a clear improvement over the other two methods. Not only is the parametrised distribution smooth, removing the need for any fixed lengthscales, but it is also better able to capture the rapidly varying form of the stream distribution function. **Redo this, I don't think I want to use the stream...**

We will now explore in more detail the properties of this new parametrisation method.

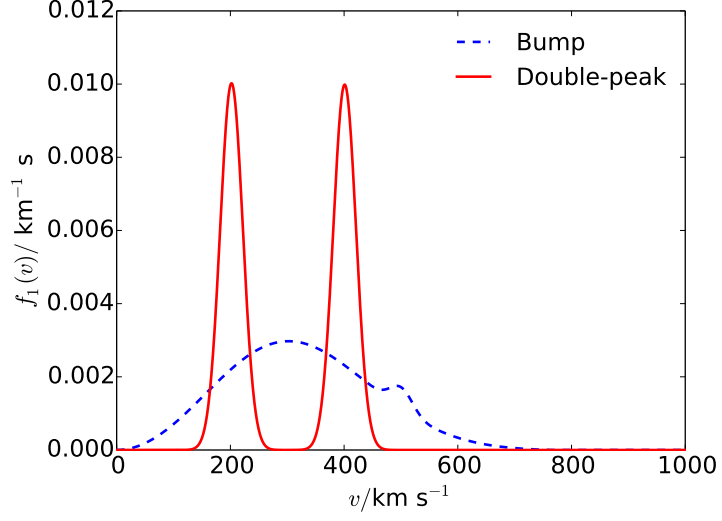


Figure 5.3: Benchmark speed distributions used in Sec. 5.3.1 to test the performance of the parametrization as a function of the number and type of basis functions.

5.3.1 Testing the parametrisation

We now consider the two questions: 1. how many basis functions are required and 2. which polynomial basis should be used? In order to answer these questions, we use the two benchmark distribution functions illustrated in Fig. 5.3. We have chosen these benchmarks not because they are necessarily realistic distribution functions but because they should be difficult to fit using standard techniques and fitting functions (e.g. [265]). The first distribution (referred to as ‘bump’) is a SHM distribution with the addition of a small bump, which contributes just 3% of the total WIMP population and could correspond to a small sub-halo or stream [268]. This should be difficult to fit because it represents only a very small deviation from the standard scenario. The second distribution (referred to as ‘double-peak’) has a sharp and rapidly varying structure, which we anticipate should be difficult to capture using a small number of basis functions.

Varying the number of basis functions

We first investigate how the reconstructed WIMP mass m_{rec} and uncertainty varies with the number of basis functions N . For now, we fix our

choice of basis to shifted Legendre polynomials:

$$P_k(v) = L_k \left(2 \frac{v}{v_{\max}} - 1 \right), \quad (5.7)$$

where L_k is the Legendre polynomial of order k , and v_{\max} is a cut off for the parametrization.

The lower panel of Fig. 5.4 shows the best fit mass and 68% confidence intervals as a function of N , using as input a WIMP of mass 50 GeV and the ‘bump’ distribution function. The reconstructed mass very rapidly settles close to the true value, using as few as three basis functions. This is because adding the bump near $v \sim 500 \text{ km s}^{-1}$ still leaves the mean inverse speed relatively smooth, so a large number of basis function are not required. The correct mass is reconstructed and we emphasize in the lower panel of Fig. 5.4 that the reconstruction is stable with the addition of more basis functions.

We should also consider how the quality of the fit changes as a function of N . We would expect that adding fit parameters should always lead to a better fit. Eventually, the fit should be good enough that adding additional basis functions will no longer improve it significantly. We can then be confident that our reconstruction is accurate and not an artifact of using too few basis functions. In order to investigate this, we utilise the Bayesian Information Criterion (BIC) [312], which is given by:

$$BIC = 2N_p \ln(N_m) - \ln(\mathcal{L}_{\max}), \quad (5.8)$$

where N_p is the number of free parameters, N_m is the number of measurements or observations and \mathcal{L}_{\max} is the maximum likelihood value obtained in the reconstruction. For the case of binned data, N_m corresponds simply to the total number of energy bins across all experiments. This criterion penalises the inclusion of additional free parameters and in comparing several models, we should prefer the one which minimises the BIC.

The upper panel of Fig. 5.4 shows the BIC (in arbitrary units) as a function of the number of basis functions for the ‘bump’ distribution function. The BIC is comparable for the cases of $N = 2$ and $N = 3$, indicating that the quality of the fit is improved slightly by the addition of another basis function. However, adding further basis functions does not have a significant impact on the maximum likelihood, leading to an increase in the BIC. This coincides with the stabilization of the reconstructed mass around

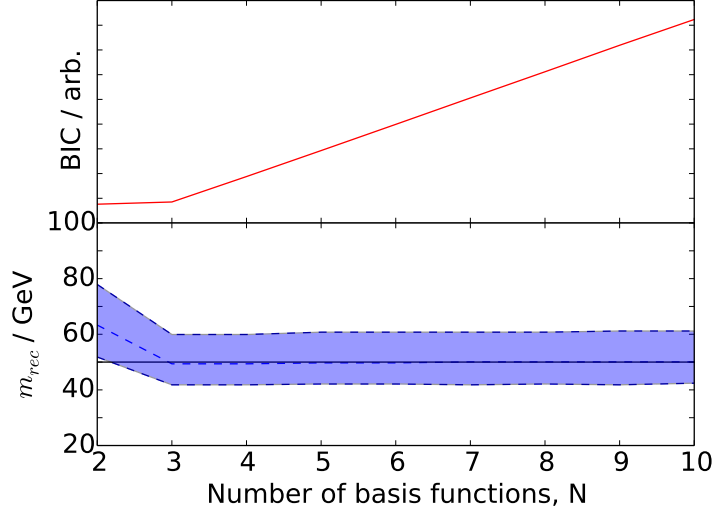


Figure 5.4: Bayesian information criterion (BIC) as a function of the number of basis functions for an underlying ‘bump’ distribution function, 50 GeV WIMP and using Legendre polynomial basis functions (upper panel). Also shown (lower panel) are the reconstructed WIMP mass (dashed blue line), 68% confidence interval (shaded blue region) and underlying WIMP mass (solid horizontal black line).

the true value and we conclude that only two or three basis functions are required to provide a good fit to the data.

Figure 5.5 shows the corresponding results for the ‘double-peak’ distribution function. Here, we note that the bias induced by using too small a number of basis functions is larger than for the case of the ‘bump’ distribution, due to the more complicated structure in this case. The BIC is minimized for $N = 7$, indicating that additional basis functions do not significantly improve the quality of the fit to data. This suggests that the shape of the speed distribution can be well fit by $N \geq 7$ basis functions. As shown in the lower panel of Fig. 5.5, the reconstruction of the WIMP mass is stable around the true mass for these values of N .

We propose that such a procedure should be used in the case of real data should a dark matter signal be observed at multiple detectors. We have shown that by analyzing the reconstructed mass as a function of N we can recover the true mass and that by using the BIC we can be confident that we have obtained an adequate fit to data.

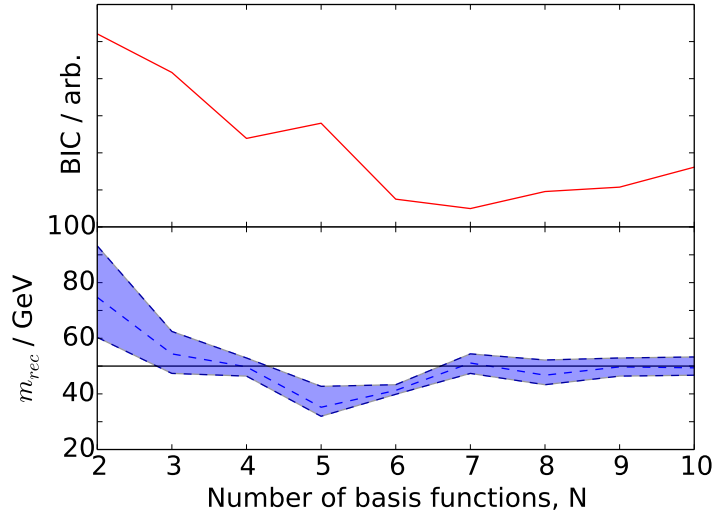


Figure 5.5: As Fig. 5.4 but for an underlying ‘double-peak’ distribution function.

5.3.2 Choice of basis functions

We now consider the second question posed at the start of Sec. 5.1: which polynomial basis should be used? As previously mentioned, we test two different polynomial bases: Legendre and Chebyshev polynomials. **Beef this section up and copy some of the ‘chebyshev is used often for approximation’ stuff down here...**

We have checked that the reconstruction results using Chebyshev polynomials are largely indistinguishable from the case of Legendre polynomials for both the ‘bump’ and ‘double-peak’ distributions and as a function of N . This leads us to conclude that the accuracy of the reconstruction is independent of the specific choice of basis. However, the reconstruction was much faster in the case of the Chebyshev basis. This is illustrated in Fig. 5.6, which shows the time taken for reconstruction of the ‘bump’ benchmark as a function of N . The time taken grows much more slowly for the Chebyshev basis (roughly as N^2) than for the Legendre basis (roughly as N^3). We have also checked that this difference is not an artifact of how we calculate the basis functions. These results indicate that this choice of basis provides both reliable and efficient reconstruction for the WIMP mass and we therefore use the Chebyshev basis in the remainder of this work.

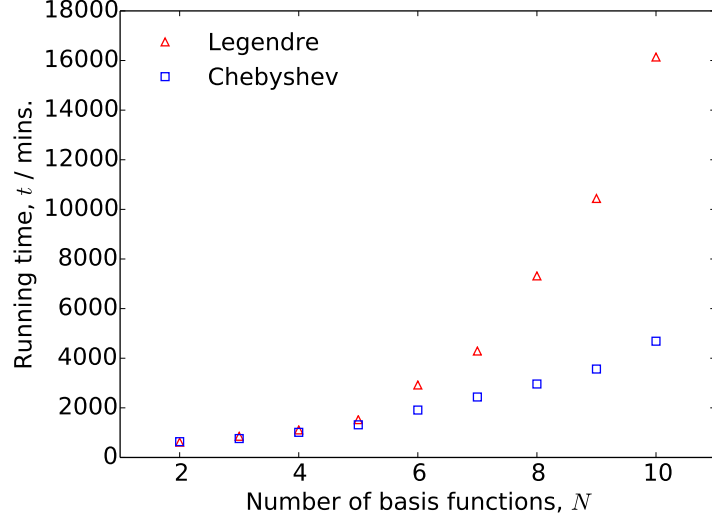


Figure 5.6: Time taken (using 4 processors in parallel) for the reconstruction of the ‘bump’ benchmark, as a function of number of basis functions. The time taken using the Chebyshev basis (blue squares) grows more slowly with N than for the Legendre basis (red triangles).

5.4 Varying m_χ

We now consider the performance of the parametrisation over a wide range of WIMP masses. We generate Asimov data for WIMP masses of 10, 20, 30, 40, 50, 75, 100, 200 and 500 GeV and reconstruct the best fit WIMP mass m_{rec} and 68% and 95% confidence intervals from the profile likelihood. We use the SHM as a benchmark distribution function and use a fixed number of $N = 5$ basis functions. The results are shown in Fig. 5.7, along with the line $m_{\text{rec}} = m_\chi$ for reference.

For large values of m_χ , the shape of the event spectrum becomes independent of m_χ [313], which results in a widening of the confidence intervals as the WIMP mass increases. For low mass WIMPs, fewer events are observed in each bin, again resulting in wider confidence intervals. It should be noted that for this analysis we have used Asimov data, in which the exact (non-integer) number of events is recorded in each bin. For low mass WIMPs, this means that the spectrum (and therefore the correct WIMP mass) is still well reconstructed using Asimov data, in spite of the small number of events. The tightest constraints are obtained when the input WIMP mass is close to the masses of several of the detector nuclei (in the range 30-80 GeV). There also appears to be no bias in the WIMP mass:

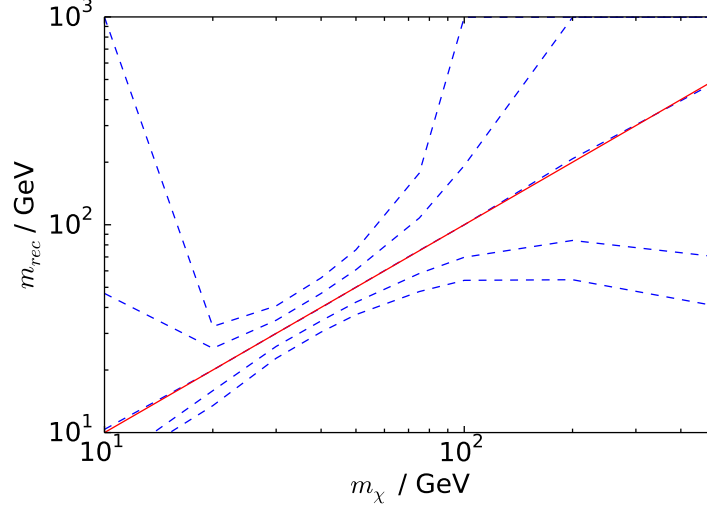


Figure 5.7: Reconstructed WIMP mass m_{rec} (central dashed blue line) as a function of input WIMP mass m_χ as well as 68% and 95% intervals (inner and outer blue dashed lines respectively). The line $m_{\text{rec}} = m_\chi$ (solid red line) is also plotted for reference.

the reconstruction matches the true mass across all values considered.

As described in Chapter 4, for low mass WIMPs the momentum distribution may be very narrow, owing to their lower momenta. However, if we wish to parametrise the full momentum range to which the experiments are sensitive, this would be much wider. **Better explanation...?** The momentum parametrization method therefore performs poorly for low mass WIMPs. The parametrization presented in this chapter does not suffer from similar problems.

So far, we have only considered idealized direct detection experiments. We now apply the method to more realistic mock detectors, taking into account the effects of finite energy resolution, as well as unrejected background events. We assume here that each experiment has a gaussian energy resolution with fixed width $\sigma_E = 1$ keV, such that the observed event rate for recoils of energy E is given by: **Do I say this in a previous chapter?**

$$\frac{dR}{dE} = \int_0^\infty \frac{1}{\sqrt{2\pi}\sigma_E} \exp\left\{-\frac{(E - E')^2}{2\sigma_E^2}\right\} \frac{dR'}{dE'} dE', \quad (5.9)$$

where the primed event rate is the underlying (perfect resolution) rate. We also assume a constant flat background rate for each experiment $R_{\text{BG}} = 10^{-6}$ events/kg/keV/day (which has been suggested as a possible background rate for Xenon1T [306] and WArP-100L [308]) when generating

mock data sets. However, we allow the flat background rate in each experiment to vary as free parameters during the fit.

We have chosen relatively generic resolution and background parameters in this work, because the precise details of energy resolution and background shape and rate will depend on the specific experiment under consideration. Instead, we hope to show that the inclusion of more realistic experimental setups does not introduce an additional bias or otherwise spoil the good properties of the method presented here.

Figure 5.8 shows the reconstructed mass as a function of input mass in this more realistic scenario. The 68% and 95% confidence intervals are now wider and the reconstructed mass does not appear to be as accurate. For input masses above ~ 100 GeV, the uncertainties become very wide, with only a lower limit of $m_{\text{rec}} > 20$ GeV being placed on the WIMP mass. Due to the poorer energy resolution the shape of the energy spectrum is less well-determined. In addition, a flat background contribution can mimic a higher mass WIMP, as it leads to a flatter spectrum. This leads to a strong degeneracy, as a wide range of mass values can provide a good fit to the data. For high input masses, the profile likelihood is approximately constant above $m_{\text{rec}} \sim 20$ GeV, indicating that there is no sensitivity to the underlying WIMP mass.

In spite of this, the true mass values still lie within the 68% and 95% confidence intervals. In addition, the poor values for the reconstructed mass for heavy WIMPs are a side effect of the loss of sensitivity. Because the profile likelihood is approximately flat, the maximum likelihood point is equally likely to be anywhere within the 68% interval. These effects would be present even if we had considered a fixed form for the speed distribution. However, when we allow for a range of possible speed distributions, the effects become more pronounced. These results show that for more realistic experimental scenarios, the method presented in this paper remains reliable over a range of masses, though its precision may be significantly reduced.

5.5 Statistical properties

Include the coverage maps...

We now consider the impact of statistical fluctuations on the reconstruction of the WIMP mass. In reality, the number of events observed N_o at a given experiment will be Poisson distributed about the expected value

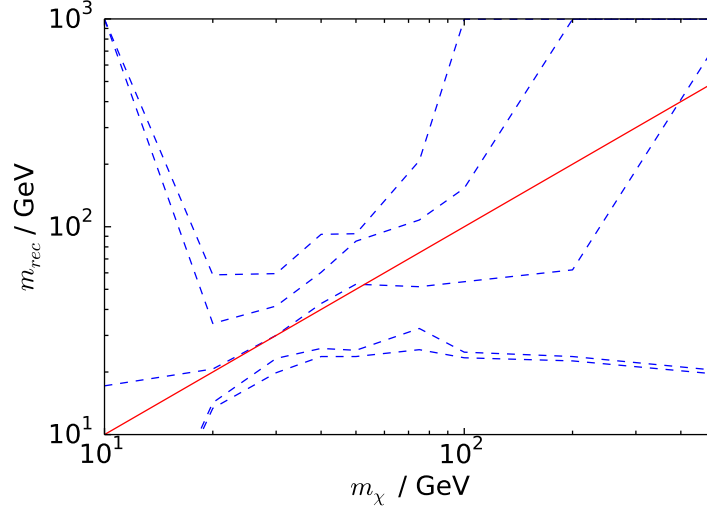


Figure 5.8: As fig. 5.7 but including the effects of finite energy resolution and non-zero backgrounds, as described in the text.

N_e , while the observed distribution of recoil energies will not exactly match that expected from the calculated event rate. The fundamental statistical limitations of future direct detection experiments have been studied in detail in Ref. [299]. As in Chapter 4, we generate 250 realisations of data from the mock experiments described in Tab. 5.1. Each realisation of the mock data is generated as follows: **Move this to the previous chapter...**

1. Calculate the number of expected events N_e , given $\{m_\chi, \sigma_p, f(v)\}$, using Eq. ??,
2. Pick the number of observed events N_o from a Poisson distribution with mean N_e ,
3. Pick recoil energies $\{E_1, E_2, \dots, E_{N_o}\}$, from the distribution $P(E)$ in Eq. ??,
4. Repeat for all three experiments.

For each realisation, we then use the method described in Sec. ?? (using $N = 5$ basis functions) to reconstruct the WIMP mass and 68% and 95% credible intervals. Figure 5.9 shows the distribution of reconstructed masses for an input mass of 50 GeV for three benchmark speed distributions: SHM, SHM+DD and Lisanti et al. as described in Sec. 5.2.2. In all three cases, the reconstructions are peaked close to the true value, regardless of

Benchmark speed distribution	Mean bias $\langle b \rangle$
SHM	0.002 ± 0.008
SHM+DD	0.005 ± 0.007
Lisanti et al.	0.01 ± 0.01

Table 5.6: Mean bias $\langle b \rangle$ in the reconstructed log WIMP mass (Eq. 5.10). This was calculated over 250 realisations using three different benchmark speed distributions.

the underlying distribution. For the SHM+DD distribution, the spread of reconstructions is slightly wider (with more reconstructions extending up to higher masses). This is due to the smaller number of events for this benchmark, making the data sets more susceptible to Poisson fluctuations.

In order to assess the accuracy of the reconstructed value of the mass m_{rec} , we also calculate the bias b for each realisation:

$$b = \ln(m_{\text{rec}}/\text{GeV}) - \ln(m_{\text{true}}/\text{GeV}). \quad (5.10)$$

We compare the logarithms of the mass values because we have used logarithmically-flat priors on the WIMP mass. In Tab. 5.6 we show the average bias across all 250 realisations for each of the three benchmark distributions. In all three cases, the average bias is consistent with zero. Even in the SHM+DD case, which shows larger fluctuations away from the true value, there is no statistical bias.

We also test the *coverage* of the credible intervals which have been constructed. **Refer back to the section on coverage.** Table 5.7 shows the coverage values for the 68% and 95% intervals obtained in this section. In each case, there is very close to exact coverage. We have also checked that these intervals only provide exact coverage for the true WIMP mass of 50 GeV. Other values of m_{rec} are contained within the intervals less frequently than the true value, again indicating that this parametrization allows for unbiased and statistically robust reconstructions of the WIMP mass.

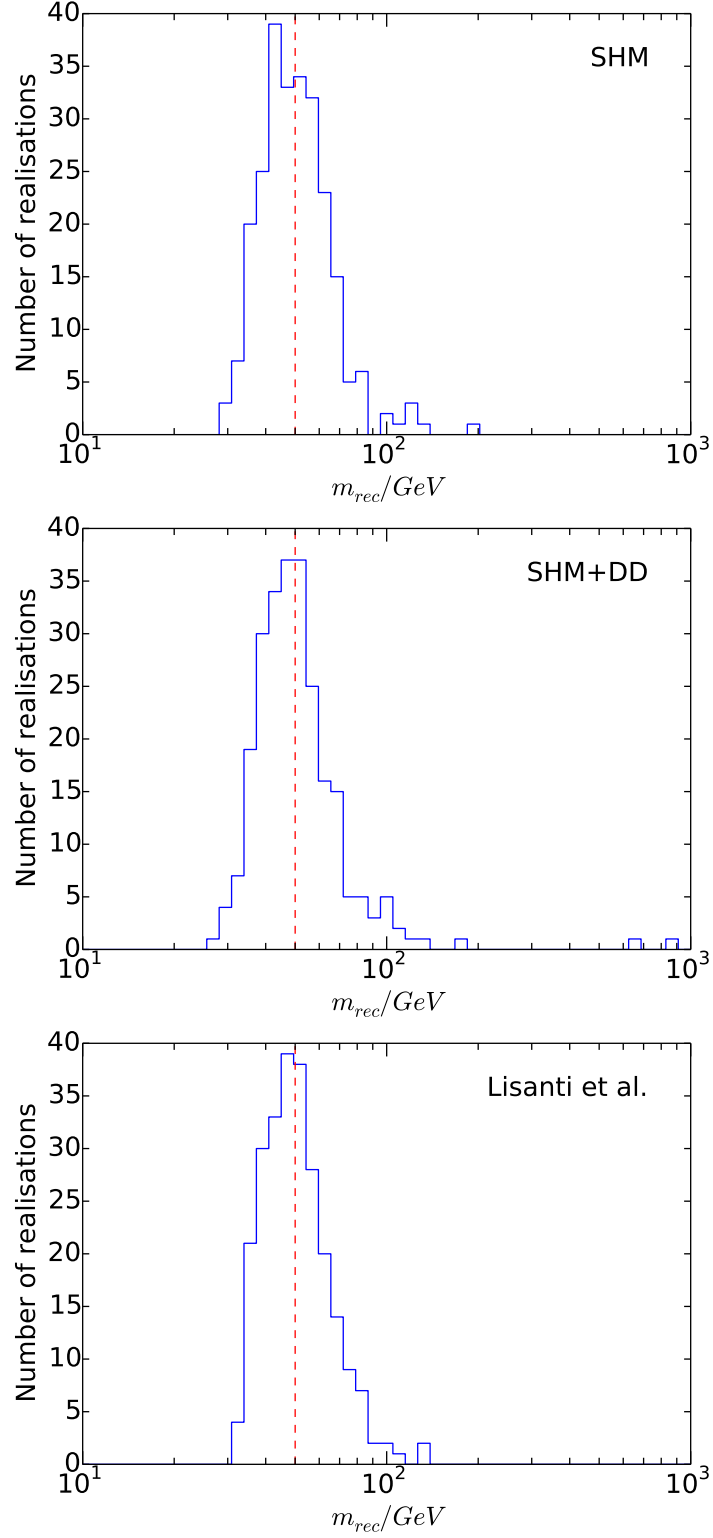


Figure 5.9: Distribution of the reconstructed mass m_{rec} for 250 mock data sets generated using several benchmark speed distributions, defined in Sec. 5.2.2. These are the SHM (top), SHM+DD (middle) and Lisanti et al. (bottom) distributions. The input WIMP mass of $m_\chi = 50$ GeV is shown as a vertical dashed red line.

Benchmark speed distri- bution	68% coverage	95% coverage
SHM	$71 \pm 3 \%$	$94 \pm 3 \%$
SHM+DD	$68 \pm 3 \%$	$91 \pm 4 \%$
Lisanti et al.	$70 \pm 3 \%$	$95 \pm 3 \%$

Table 5.7: Coverage of 68% and 95% credible intervals calculated from 250 data realisations each for three benchmark speed distributions. The concept of coverage is described in the text of Sec. 5.5.

5.6 Reconstructing $f_1(v)$

Using the method described in this paper, we can obtain the posterior probability distribution for the coefficients $\{a_1, \dots, a_{N-1}\}$ given the data, which we refer to as $P(\mathbf{a})$. We would like to be able to present this information in terms of the distribution function $f_1(v)$ in order to compare with some known distribution or look for particular features in the distribution. However, due to the fact that the distribution function is normalized, the values of f_1 at different speeds will be strongly correlated. We illustrate here how robust comparisons with benchmark distributions can be made.

As a first step, we can attempt to sample from the $P(\mathbf{a})$, in order to obtain $P(f_1(v))$. This is the probability distribution for the value of f_1 at a particular speed v , marginalizing over the values of f_1 at all other speeds. We can repeat for a range of speeds to obtain 68% and 95% credible intervals for the whole of $f_1(v)$. The result of this procedure is presented in Fig. 5.10, for a randomly selected realisation from the SHM ensemble of Sec. 5.5. The underlying SHM distribution is shown as a solid line, while the 68% and 95% marginalized intervals are shown as dark and light shaded regions respectively. In this naive approach, we see that there is little shape information which can be recovered from the reconstruction, with only upper limits being placed on the speed distribution.

This method performs poorly because, as initially mentioned in Sec. 5.2.3, we have no information about the fraction of dark matter particles below the energy threshold of our experiments. If this fraction is large, the event rate for a given cross-section is suppressed. However, increasing the cross-section will increase the total event rate. There is thus a degeneracy be-

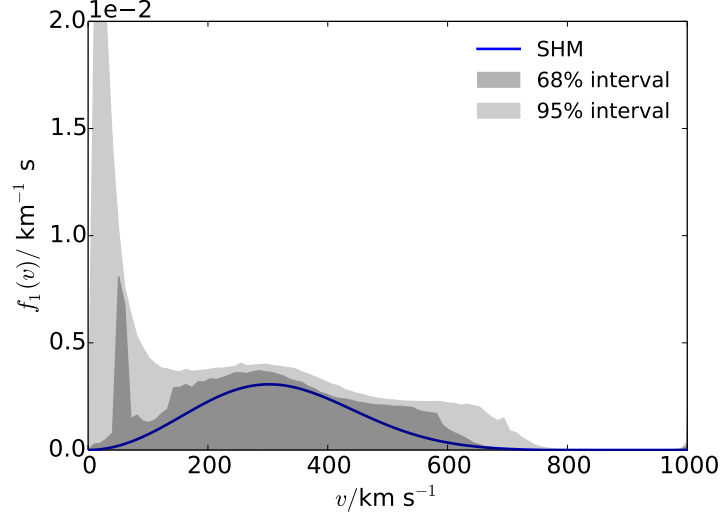


Figure 5.10: Reconstructed speed distribution for a single realisation of data, generated for a 50 GeV WIMP. 68% and 95% credible intervals are shown as dark and light shaded regions respectively, while the underlying SHM distribution function is shown as a solid blue line.

tween the shape of the speed distribution and the cross-section, meaning that we can only probe the shape of $f_1(v)$, rather than its overall normalization. This degeneracy has not been accounted for in Fig. 5.10. We can attempt to correct for this by adjusting the normalization of $f_1(v)$. If we fix $f_1(v)$ to be normalized to unity above v_a (where $v_a \approx 171 \text{ km s}^{-1}$ is the lowest speed probed by the experiments for a WIMP of mass 50 GeV), we can compare the shapes of the underlying and reconstructed distribution functions. This is illustrated in Fig. 5.11, which shows that we now broadly reconstruct the correct shape of $f_1(v)$. Below v_a , the value of $f_1(v)$ is poorly constrained, because the experiments provide no information about the shape of the distribution below threshold.

There remain several issues with this approach. In order to utilize this method, we must know the approximate value of the lowest speed probed by the experiments. However, this value is set by the WIMP mass. We could determine v_a using the reconstructed WIMP mass, but this would be subject to significant uncertainty. In addition, direct reconstructions of the speed distribution are easily biased. The upper limit of the energy windows of the experiments corresponds to a particular WIMP speed (for a given WIMP mass). WIMPs above this speed still contribute to the total event rate, but contribute no spectral information. The reconstructed shape of

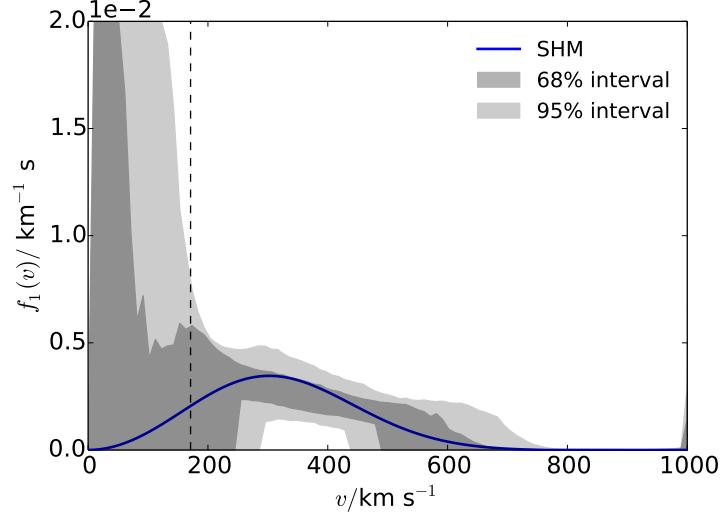


Figure 5.11: Reconstructed speed distribution for the same realisation of data as Fig. 5.10. In this case, we have also normalized $f_1(v)$ to unity above $v_a \approx 171 \text{ km s}^{-1}$ (vertical dashed line). This is the lowest speed accessible to the experiments for a WIMP of mass 50 GeV. 68% and 95% credible intervals are shown as dark and light shaded regions respectively, while the underlying SHM distribution function is shown as a solid blue line.

the high speed tail of the distribution is therefore not constrained by the data, but may affect the reconstructed value of f_1 at lower speeds.

An alternative approach is to reconstruct the mean inverse speed $\eta(v)$ (defined in Eq. ??) at some speed v . Because $\eta(v)$ is an integral function of f_1 , it is less prone to bias as it takes into account the full shape of the distribution at speeds greater than v . However, we do not know the normalization of f_1 and so we must normalize η appropriately. For each point sampled from $P(\mathbf{a})$, we calculate η . We then divide by $\alpha(v)$, the fraction of WIMPs above speed v , calculated using the same parameter point:

$$\alpha(v) = \int_v^\infty f_1(v') dv'. \quad (5.11)$$

We will write this rescaled mean inverse speed as $\eta^*(v) = \eta(v)/\alpha(v)$. The value of $\eta^*(v)$ is a measure of the shape of the distribution function above v . However, information about the normalization of the distribution has been factored out by dividing by $\alpha(v)$. We no longer need to know the value of v_a in order to obtain information about the shape of the distribution at higher speeds. We may still need to decide the speed down to

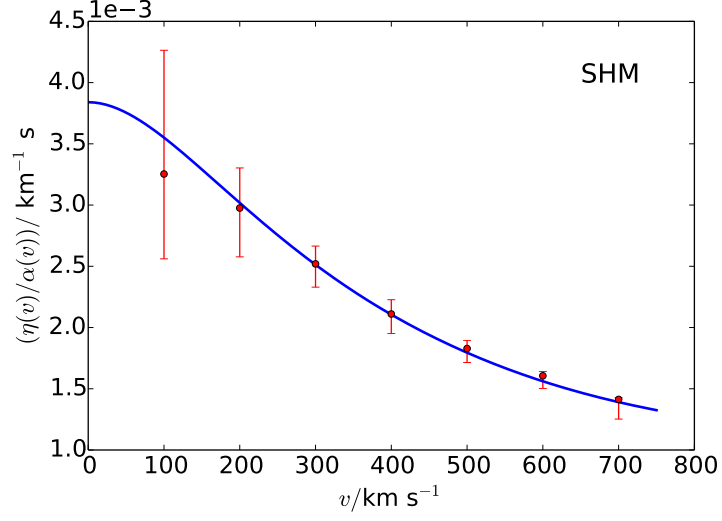


Figure 5.12: Mean reconstructed values of the rescaled mean inverse speed $\eta(v)/\alpha(v)$ at several values of v , calculated over 250 realisations of data using a 50 GeV WIMP and underlying SHM distribution function. Errorbars indicate the mean upper and lower limits of the 68% credible intervals. The underlying form of $\eta(v)/\alpha(v)$ obtained from the SHM is shown as a solid blue line.

which we trust our reconstruction, but this no longer relies on an arbitrary choice of v_a to normalize the reconstructions at all speeds.

In Fig. 5.12, we plot the mean reconstructed value of η^* at several values of v , using 250 realisations of the 50 GeV SHM benchmark. We also show the mean upper and lower limits of the 68% credible intervals as errorbars. The form of η^* for the SHM is shown as a solid blue line. In all cases except for $v = 100 \text{ km s}^{-1}$, the mean reconstructed value is close to the true value, indicating that η^* can be reconstructed without bias using this method. At low speeds, the reconstructed value deviates from the true value. In addition, the credible intervals lead to *undercoverage* in the $v = 100 \text{ km s}^{-1}$ case. However, this point lies below the lowest speed to which the experiments are sensitive and therefore we cannot trust the reconstruction at this low speed. We have checked that for the remaining values of v the method provides exact or overcoverage, indicating that at higher speeds we can use η^* as a reliable and statistically robust measure of the shape of the distribution.

In the case of a single realisation of data, we would like to compare the probability distribution for $\eta^*(v)$ (obtained from $P(\mathbf{a})$) to the value calculated from some test distribution. We note that several distributions

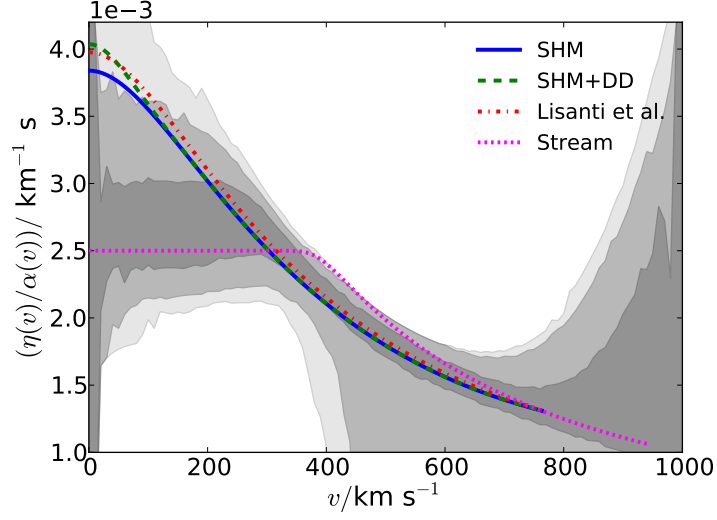


Figure 5.13: Rescaled mean inverse speed $\eta(v)/\alpha(v)$, reconstructed from a single realisation of data using a 50 GeV WIMP and underlying SHM distribution function. At each value of v we calculate 68%, 95% and 99% credible intervals (shown as shaded intervals). We also show the calculated values of $\eta(v)/\alpha(v)$ for several possible benchmark speed distributions: SHM (solid blue), SHM+DD (dashed green), Lisanti et al. (dot-dashed red) and stream (dotted magenta). The benchmark curves are truncated when the underlying distribution function goes to zero.

may produce the same value of $\eta^*(v)$ at a given value of v . Thus, we may fail to reject a distribution function which is not the true distribution. However, if the calculated value of $\eta^*(v)$ does lie outside the $p\%$ interval, we can reject it at the $p\%$ level.

Make sure I don't confuse the definitions of α ...

We can increase the discriminating power of this method by repeating this reconstruction over all speeds and checking to see if the benchmark value of η^* is rejected at any value of v . The result of this procedure is shown in Fig. 5.13 for a single realisation of data generated using an SHM distribution (the same data as in Figs. 5.10 and 5.11). We plot the 68%, 95% and 99% credible intervals as shaded regions, as well as the values of $\eta^*(v)$ calculated from several benchmark speed distribution. We will focus on the intermediate speed range ($v \gtrsim 200 \text{ km s}^{-1}$), as we do not know *a priori* the lowest speed to which the experiments are sensitive.

The reconstructed intervals are consistent with a range of possible distribution functions. The SHM and SHM+DD distributions are identical over a wide range of speeds. This is because above $\sim 200 \text{ km s}^{-1}$, the two

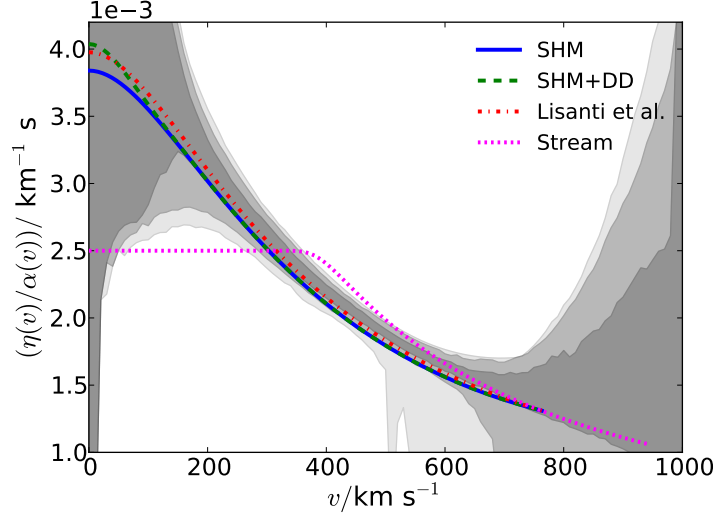


Figure 5.14: As Fig. 5.13, but using as input a Lisanti et al. speed distribution and an exposure time which is 2.5 times longer.

distributions differ in normalization but not in shape. Differences appear between the two at low speeds where their shapes diverge. The Lisanti et al. distribution results in a larger deviation from the SHM, but not sufficiently large to differentiate between the two distributions given the size of the uncertainties. Finally, the stream distribution results in a significantly different form for $\eta^*(v)$. At approximately 400 km s^{-1} , the curve for the stream distribution lies outside the reconstructed 99% credible interval. We can therefore use this method to reject the stream distribution at the 99% confidence level.

Figure 5.14 shows the results of a reconstruction using a larger exposure. In this case, we generate data using the Lisanti et al. distribution and an exposure increased by a factor of 2.5, resulting in approximately 1000 events across the three detectors. As expected, the resulting credible intervals are now substantially narrower. The stream distribution now lies significantly outside the 99% interval. In Fig. 5.15, we show the same results, but focusing in on the region around $v \sim 400 \text{ km s}^{-1}$. At certain points, the SHM and SHM+DD distributions now lie outside the 95% credible interval, suggesting that with a number of events of the order of 1000, we may be able to reject these benchmarks.

While the method displayed in Fig. 5.11 allows the approximate shape of the speed distribution to be reconstructed, reconstructions of $\eta^*(v)$ allow more statistically robust statements to be made about the underlying speed

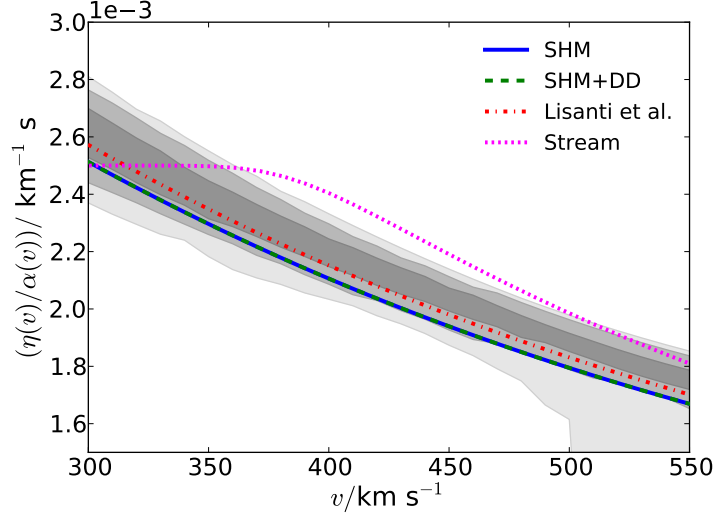


Figure 5.15: As Fig. 5.14, but focusing on the region around $v \sim 400 \text{ km s}^{-1}$. Notice that in the range $400 - 550 \text{ km s}^{-1}$, both the SHM and SHM+DD curves lie at or below the lower limit of the 95% credible interval.

distribution. In particular, Fig. 5.15 illustrates that with larger exposures deviations from Maxwellian speed distributions can be detected in a model-independent fashion.

We have studied in detail a new parametrization for the local dark matter speed distribution, which provides a significant improvement over previous model-independent parametrizations. This method involves writing the logarithm of the speed distribution as a polynomial in speed v and fitting the polynomial coefficients (along with the WIMP mass and cross section) to the data. We have attempted to disentangle in this paper the influence of different benchmark speed distributions, different benchmark WIMP masses and different forms for the parametrization. **These conclusions may be a little wordy...** We summarize our conclusions as follows:

- We have shown that the reconstruction of the WIMP mass is robust under changes in the number of basis functions N . We have used the Bayesian Information Criterion (BIC) to compare models with different values of N and have shown that minimizing the BIC allows us to determine how many basis functions are required for a reliable reconstruction. We have also demonstrated that the results of the method do not depend strongly on the choice of basis func-

tions, but that the speed of reconstructions may improved by using the Chebyshev polynomial basis.

- We have shown that the method leads to unbiased reconstructions of the WIMP mass for masses in the range 10-500 GeV. Including realistic experimental parameters, including non-zero backgrounds and finite energy resolution, reduces the precision of these reconstructions. In particular, for large values of the input mass, we can only place a lower limit of approximately 20 GeV on the reconstructed mass. This is significantly lower than in the idealized case, where we can typically constrain the WIMP mass to be heavier than around 50 GeV.
- We have used several ensembles of data realisations to demonstrate the statistical properties of the method, including unbiased reconstructions and exact coverage of the WIMP mass.
- We have presented several ways of displaying the reconstructed WIMP speed distribution using this method. In order to make robust statistical inferences about the speed distribution, we calculate the probability distribution of $\eta(v)/\alpha(v)$. This is the mean inverse speed $\eta(v)$, which appears in the direct detection event rate (eq. ??), rescaled by the fraction of WIMPs $\alpha(v)$ above speed v . This can be used as a measure of the *shape* of the distribution function, from which the unknown normalization has been factored out. We can then compare to the expected value of $\eta(v)/\alpha(v)$ from a given benchmark speed distribution, allowing us to distinguish between different underlying models.

It should be noted that due to the finite threshold energies of direct detection experiments, we cannot probe the low speed population of WIMPs. If we make no assumptions, we have no information about the form of $f(v)$ below threshold and therefore little information about the overall normalisation of $f(v)$. This translates to an unavoidable degeneracy in the WIMP interaction cross section σ_p^{SI} .

In spite of this, we have shown that the method allows for a robust determination of the WIMP mass over a large range of input parameters, both in terms of particle physics and astrophysics. The inclusion of more realistic experimental parameters does not introduce any additional bias,

but does reduce the precision of reconstructions. Finally, we have shown that we can distinguish different forms of the speed distribution. With around 1000 events, it may be possible to detect minor deviations from the Standard Halo Model and begin to search for more interesting structure in the speed distribution of the Milky Way.

Chapter 6

Breaking the cross section degeneracy: neutrino telescopes

Chapter 7

Speed parametrisation for directional experiments

7.1 Introduction

While traditional direct detection experiments seek to measure the recoil energies deposited by WIMPs scattering off detector nuclei, *directional* experiments aim to measure both the energy and direction of the recoil. While the recoil distribution of typical backgrounds is expected to be roughly isotropic, the WIMP-induced recoil distribution is expected to be highly directional. The motion of the Sun through the Galactic DM halo generates a so-called ‘WIMP wind,’ leading to an event rate peaked in the opposing direction, the direction of the constellation of Cygnus.

The ability of directional detection to distinguish background from signal and to provide a model independent confirmation of the dark matter origin of the signal make it a promising search strategy. However, measuring the direction of rare, low energy recoils remains challenging []. A number of directional detectors are currently in development and a number of novel methods for directional detection have been proposed.

Measuring the directional recoil spectrum allows us to probe not only the energy distribution of WIMPs in the Galactic halo (embodied in the speed distribution $f(v)$), but the full 3-dimensional velocity distribution $f(\mathbf{v})$. This may allow us to gain new insight into the formation processes at hand in the growth of the Milky Way halo []. However, it also introduces new uncertainty into calculating the event rate. While non-directional detection leaves us with a single free function in the form of $f(v)$, the direc-

tional case relies upon the *a priori* unknown function of a 3-dimensional vector, $f(\mathbf{v})$.

In this chapter, we will first introduce the formalism by which the directional rate is calculated. Specifically, we introduce the Radon transform which relates the WIMP velocity distribution to the corresponding nuclear recoil distribution. We then discuss the current state of directional detection technology and the progress of several directional experiments. We then discuss previous approaches to mitigating the uncertainties associated with the velocity distribution. Finally, we consider a new method for parametrising $f(\mathbf{v})$, which allows it to be written in terms of a finite number of one-dimensional functions, and how to calculate the Radon transform of this new, discretised distribution function.

7.2 Directional event rate

First, we wish to calculate the directional event spectrum in a dark matter detector. We follow the treatment of Gondolo [314], noting that similar calculations were performed previously by Copi, Heo and Krauss [315] and later by Copi and Krauss [316]. The scattering of a dark matter (DM) particle with a nucleus is illustrated in Fig. 7.1.

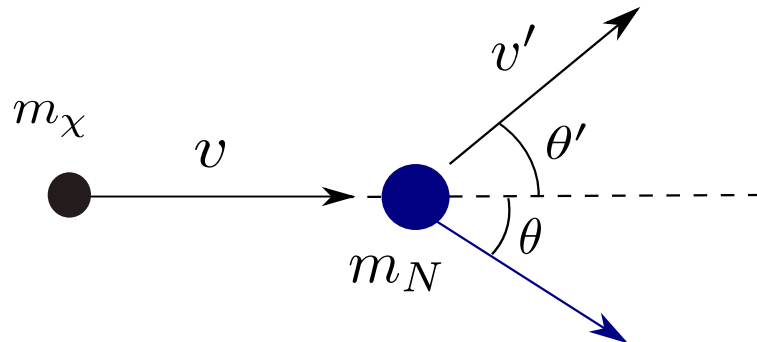


Figure 7.1: Illustration of the scattering of a DM particle of mass m_χ from a nucleus of mass m_N .

We consider a DM particle of mass m_χ impinging with velocity $\mathbf{v} = v(1, 0)$ on a stationary target nucleus of mass m_N . The dark matter scatters with velocity $\mathbf{v}' = v'(\cos \theta', \sin \theta')$ and the nucleus scatters with final momentum $\mathbf{q} = q(\cos \theta, \sin \theta)$. From conservation of linear momentum we obtain:

$$m_\chi v' \cos \theta' = m_\chi v - q \cos \theta, \quad (7.1)$$

$$m_\chi v' \sin \theta' = q \sin \theta. \quad (7.2)$$

We can eliminate θ' by summing the squares of Eqs. 7.1 and 7.2, to obtain:

$$v'^2 = v^2 - \frac{2vq \cos \theta}{m_\chi} + \frac{q^2}{m_\chi^2}. \quad (7.3)$$

From energy conservation, we obtain:

$$v'^2 = v^2 - \frac{q^2}{m_\chi m_N}. \quad (7.4)$$

Combining these, we see that the recoil momentum of the target nucleus is given by

$$q = 2\mu_{\chi N} v \cos \theta, \quad (7.5)$$

where $\mu_{\chi N} = m_\chi m_N / (m_\chi + m_N)$ is the DM-nucleus reduced mass.

For a WIMP-nucleus interaction cross section which is independent of velocity, we can write the differential cross section as

$$\frac{d\sigma}{dE_R} = \frac{m_N \sigma_p}{2\mu_{\chi p}^2 v^2} \mathcal{C} F^2(E_R), \quad (7.6)$$

where E_R is the nuclear recoil energy, σ_p is the WIMP-proton interaction cross section (which may be spin-dependent (SD) or spin-independent (SI)) and \mathcal{C} and F^2 are the corresponding enhancement factor and nuclear form factor (see Eq. 2.25).

We now obtain from here the double differential cross-section $\frac{d\sigma}{dE_R d\Omega_q}$. The collision is azimuthally symmetric, so that $d\Omega_q = 2\pi d\cos\theta$. We then require a Dirac δ -function to impose the condition in Eq. 7.5: $\delta(\cos\theta - q/2\mu_{\chi N}v) = v\delta(v\cos\theta - q/2\mu_{\chi N})$. We finally obtain

$$\frac{d\sigma}{dE_R d\Omega_q} = \frac{m_N \sigma_p}{4\pi \mu_{\chi p}^2 v} \mathcal{C} F^2(E_R) \delta(v\cos\theta - v_{\min}) \quad (7.7)$$

where v_{\min} is the minimum WIMP speed required to excite a recoil of momentum q or, equivalently, energy E_R :

$$v_{\min} = \frac{q}{2\mu_{\chi N}} = \sqrt{\frac{m_N E_R}{2\mu_{\chi N}^2}}. \quad (7.8)$$

To obtain the differential rate per unit detector mass, we divide by the mass of the target nucleus and multiply by the WIMP flux at velocity \mathbf{v} ,

$$\frac{\rho_0}{m_\chi} v f(\mathbf{v}) d^3\mathbf{v}, \quad (7.9)$$

before integrating over all WIMP velocities, where ρ_0 is the local dark matter mass density. Combining these, we obtain:

$$\frac{dR}{dE_R d\Omega_q} = \frac{\rho_0 \sigma_p}{4\pi \mu_{\chi p}^2 m_\chi} \mathcal{C} F^2(E_R) \hat{f}(v_{\min}, \hat{\mathbf{q}}), \quad (7.10)$$

where $\hat{f}(v_{\min}, \hat{\mathbf{q}})$ is the Radon Transform of the velocity distribution, defined as:

$$\hat{f}(v_{\min}, \hat{\mathbf{q}}) = \int \delta(v_{\min} - \mathbf{v} \cdot \hat{\mathbf{q}}) f(\mathbf{v}) d^3\mathbf{v}. \quad (7.11)$$

Geometrically, this is the integral of $f(\mathbf{v})$ over a plane perpendicular to $\hat{\mathbf{q}}$ at a distance v_{\min} from the origin. In physical terms, for a given recoil angle and energy, we integrate over all WIMP velocities satisfying the kinematic constraint given by Eq. 7.5.

7.2.1 Examples

We consider several examples of velocity distributions and their corresponding Radon transforms. For an isotropic Maxwell-Boltzmann distribution with dispersion σ_v ,

$$f(\mathbf{v}) = \frac{1}{(2\pi\sigma_v^2)^{\frac{3}{2}}} \exp\left[-\frac{\mathbf{v}^2}{2\sigma_v^2}\right], \quad (7.12)$$

the Radon transform is also isotropic,

$$\hat{f}(v_q, \hat{\mathbf{q}}) = \frac{1}{(2\pi\sigma_v^2)^{\frac{1}{2}}} \exp\left[-\frac{v_q^2}{2\sigma_v^2}\right]. \quad (7.13)$$

If we take this form to describe the DM velocity distribution in the galactic frame, we must transform to the laboratory frame using the relation [314]

$$\hat{f}_{\text{lab}}(v_q, \hat{\mathbf{q}}) = \hat{f}_{\text{gal}}(v_q - \mathbf{v}_{\text{lag}} \cdot \hat{\mathbf{q}}, \hat{\mathbf{q}}), \quad (7.14)$$

where \mathbf{v}_{lag} is the velocity of the peak of the galactic distribution with respect to the laboratory. We therefore obtain the Radon transform of the Standard Halo Model

$$\hat{f}(v_q, \hat{\mathbf{q}}) = \frac{1}{(2\pi\sigma_v^2)^{\frac{1}{2}}} \exp \left[-\frac{(v_q - \mathbf{v}_{\text{lag}} \cdot \hat{\mathbf{q}})^2}{2\sigma_v^2} \right]. \quad (7.15)$$

This can be extended to incorporate a cut off at the galactic escape velocity, or for more general anisotropic velocity distributions [314].

Another interesting velocity distribution is that of a stream

$$f(\mathbf{v}) = \delta(\mathbf{v} - \mathbf{v}_s), \quad (7.16)$$

which has Radon transform

$$\hat{f}(v_q, \hat{\mathbf{q}}) = \delta(v_q - \mathbf{v}_{\text{lag}} \cdot \hat{\mathbf{q}}). \quad (7.17)$$

This results in a highly directional signal, producing a spherical recoil spectrum centred on $\mathbf{v} = \mathbf{v}_s/2$.

In Fig. 7.2, we illustrate the Radon transform of the SHM (top), the SHM with a contribution from a dark disk (middle), and a stream (bottom). We evaluate the Radon transform at a value $v_q = 100 \text{ km s}^{-1}$. In all cases, there is a clear anisotropy and the three scenarios are easily distinguishable. This highlights the discriminatory power of directional detection. It has previously been demonstrated that only of order 10 events would be required to distinguish a directional WIMP signal from an isotropic background. Furthermore, with of order 100 events, it should be possible to detect any deviation in peak recoil direction due to a stream [317].

Say more about DD

7.3 Directional experiments

Directional experiments are still in the prototype stage, with detectors being around 1 m^3 in size, with hopes for a scale up to ton-scale experiments in the future. A number of experiments use time projection chamber (TPC) technology to achieve directional sensitivity. These include DRIFT [318, 319], NEWAGE [320, 321], MIMAC [322, 323], DMTPC [324, 325] and D3 [326].

In order to have directional sensitivity, a detector must image the tracks produced by the recoiling nucleus in the detector. The typical range of a

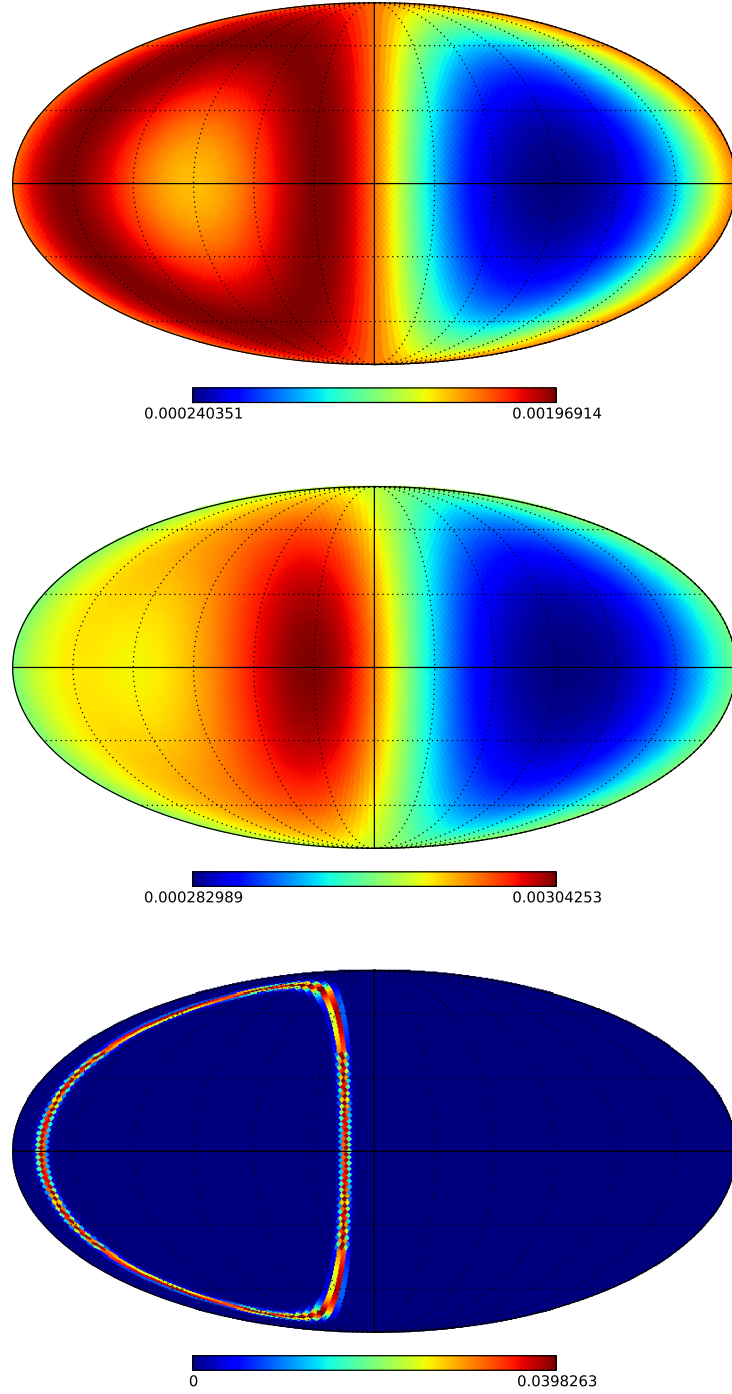


Figure 7.2: Radon transform of the SHM (top), SHM with a dark disk contribution (middle) and stream (bottom) distribution functions, evaluated at $v_q = 100 \text{ km s}^{-1}$.

WIMP-nucleus recoil is only $\sim 100 \text{ nm}$, however, which makes track reconstruction difficult. Directional experiments therefore operate in the low

pressure gas phase (around 0.05 atm [319]) in order to maximise the distance travelled by a recoiling nucleus. The detector is filled with a target gas such as CF_4 (in the case of the DRIFT experiment) which provides sensitivity to spin-dependent recoils. Nuclear recoils in the detector ionize the target gas. The freed electrons are drifted under an electric field to the faces of the detector where the charge is collected. Alternatively, an electron transport gas (CS_2 in the DRIFT experiment) may be added, which attracts the free electrons forming ions which are then collected.

The energy of the recoil can be recovered from the total amount of ionisation in the event. The three dimensional track (which is only a few mm long) can be reconstructed from the distribution of charge detected at the surface of the detector volume, with information about the z-direction obtained from the timing of the charges arriving at the surface. **Check this...** This method allows an angular resolution of 20° - 80° using current prototypes [327], with higher resolution at higher recoil energies. However, the sense of the recoil is much more difficult to determine, requiring sensitivity to tiny asymmetries between the start and end of the track. While sense discrimination has previously been demonstrated [328], it cannot be achieved with 100% efficiency. Even for high energy (100 keV) recoils, studies suggest that only partial sense recognition may be possible (with only a 65% probability of correctly determining the sense) [327]. Without sense discrimination the anisotropy of the WIMP signal is reduced and roughly 3 times more events are required to establish the directionality of the signal and distinguish from an anisotropic background [313, 317].

Talk about anodes rather than surfaces...

Background - Radon progeny; fiducialisation; thresholds

A number of other directional technologies have also been suggested. Nuclear emulsion experiments use as a target silver halide crystals suspended in gelatin [329]. The emulsion required must be composed of very fine grains in order to image dark matter recoil tracks smaller than $1\ \mu\text{m}$, however angular resolutions below 20° may be achievable. DNA based experiments [216] have also been proposed which may be able to achieve directional sensitivity. The main TPC-based experiments are in cooperation and are ultimately aiming to construct a ton-scale ‘CYGNUS’ detector [330].

7.4 Reconstructing the velocity distribution

With promising developments in directional detector technology, it is interesting to ask what information about the velocity distribution we could, in principle, extract from a directional signal. Alves, Hendri and Wacker [331] investigated the possibility of describing $f(\mathbf{v})$ in terms of a series of special functions of integrals of motion (energy and angular momentum). These can then be fit to data, with around 1000 events required to distinguish between the SHM and a Via Lactea II distribution function [332]. However, the special, separable form of the velocity distribution requires that the dark matter halo is in equilibrium. Moreover, this method requires an *a priori* knowledge of the DM mass (for example from earlier non-directional detectors or from collider experiments).

A more general parametrisation for the velocity distribution was recently proposed by Lee [333]. In this approach, the velocity distribution is decomposed into products of Fourier-Bessel functions and spherical harmonics. This is completely general and does not require that the halo is completely virialised. Lee also gives an analytic expression for the Radon transform of the Fourier-Bessel basis, making this approach computationally efficient. However, this basis does not guarantee that the resulting $f(\mathbf{v})$ is everywhere positive and therefore not all combinations of coefficients correspond to physical distribution functions. **Might be a good idea after a large number of events have been found...**

In fact, any decomposition in terms of spherical harmonics leads to this problem. It is unclear how this issue will affect parameter reconstruction. Without some criteria which determines which coefficients of the spherical harmonics lead to strictly positive distribution functions, it may be necessary to numerically test each parametrised distribution function for negative values. However, for a real function of three parameters $f(\mathbf{v}) = f(v_x, v_y, v_z)$ this would require a very large number of evaluations, which may not be computationally feasible. In addition, it is not clear how this property would affect an exploration of the parameter space using, for example, Markov Chain Monte Carlo or Nested Sampling [?]. Physical distribution functions may occupy only a small fraction of the total space of parameters or may be distributed over a large number of irregular regions in the parameter space, making sampling from them difficult.

In Sec. 7.5, I will present an alternative method of parametrising the velocity distribution, which can guarantee that the velocity distribution is everywhere positive and therefore represents a promising and general method for extracting information from directional experiments. However, first it will be instructive to discuss the invertibility of the Radon transform. That is, given a perfect realisation of the directional recoil spectrum, can we perfectly reconstruct the corresponding velocity distribution.

Point out that this is harder when you have a full 3-D function...?

7.4.1 Invertibility of the Radon transform

Make sure to check and improve the terminology - especially ‘null functions’

It has been shown that for distributions $f(\mathbf{v})$ which are rapidly decreasing at infinity [334] or which are compactly supported [335], the Radon Transform is one-to-one and is therefore exactly invertible. This inversion is typically unstable (that is, the reconstructions are very sensitive to noise in the signal) and ill-posed (as not all functions are valid Radon Transforms). However, assuming that \hat{f} is a valid Radon Transform and that we have full knowledge of it, we can reconstruct $f(\mathbf{v})$ exactly.

However, due to finite energy thresholds, we do not have access to the low-speed region of $\hat{f}(v_{\min}, \hat{q})$. We must therefore consider the related Exterior Radon Transform \mathcal{R}_E . Only using values of the Radon Transform for $v_{\min} > v_a$, is it possible to reconstruct $f(\mathbf{v})$ for $v > v_a$? If f is rapidly decreasing at infinity, this transform is still one-to-one, as in the complete case. However, if f decays as an inverse power of v (i.e. $f \sim v^{-k}$ as $v \rightarrow \infty$) the Exterior Transform is no longer one-to-one [336]. *Define null space...* In this case, the null space in 3 dimensions is non-trivial [337], consisting of functions of the form:

$$f_N(\mathbf{v}) = \frac{\alpha}{v^{3+k}} Y_{lm}(\hat{\mathbf{v}}), \quad (7.18)$$

where α is some constant, Y_{lm} is a spherical harmonic, $0 \leq k < l$ and $l - k$ is even. This means that there are no null functions for $l = 0$ or $l = 1$. It can be shown by explicit calculation that such functions have a Radon Transform of zero for all $v_{\min} > 0$.

In the case of direct detection, the point at $v = v_{\min} = 0$ corresponds to DM particles at rest with respect to the detector, which can impart no recoil energy and are therefore undetectable. For directional detection

then, even for infinitesimally small threshold energies, we must consider the Exterior Radon Transform.

This means that for a given Radon transform, adding any combination of functions of the form $f_N(\mathbf{v})$ to $f(\mathbf{v})$ leads to the same Radon transform. However, we note that the spherical harmonics with $l > 0$ can take negative values. However, at large values of v , f_{SHM} decays exponentially. By contrast, f_N decays as a power of v , meaning at some (potentially large) value of v the magnitude of the null function will exceed that of $f(\mathbf{v})$ leading to a negative distribution function. A more general distribution function will have a natural cut-off (say at the galactic escape speed) and will certainly decay rapidly to zero for high values of v . As a result, we can neglect the impact of null functions on reconstructions.

Thus, as long as we choose basis functions which are everywhere positive and therefore physically valid, we ensure that the Radon transform is invertible. This means that no information is lost in reconstructing $f(\mathbf{v})$ and also that there are no unphysical degeneracies present in the parametrisation we have chosen.

NB: Make it very clear that if we choose a parametrisation which can be somewhere negative (even if it's a high energies where these things don't matter because its above threshold and only a small effect), it can lead to problems of non-invertibility and introduce unphysical degeneracies in the parametrisation. Therefore it is very important to make sure that $f(\mathbf{v})$ is everywhere positive. I should include some plots of the null functions and of truncated null functions (added to $f(\mathbf{v})$) to indicate what can go wrong - and how bad things can be. Also, talk about truncated null functions and check that if we ensure positive-definiteness then truncated null functions shouldn't cause a problem... Double-check to see if truncated null functions (truncated at the same place as the full distribution function) are still null (they shouldn't be, don't just look along one direction, but all... IT DEFINITELY IS NOT NULL, SO THAT'S FINE...)

Also say that I don't think that this has previously been discussed...

7.5 Discretising the velocity distribution

In order to ensure that the velocity distribution is everywhere positive, we propose an alternative methodology. We propose that the velocity dis-

tribution be discretised into N angular components, each described by a single function of the WIMP speed:

$$f(\mathbf{v}) = f(v, \cos \theta', \phi') = \begin{cases} f_1(v) & \text{for } \theta' \in [0, \pi/N] , \\ f_2(v) & \text{for } \theta' \in [\pi/N, 2\pi/N] , \\ \vdots & \\ f_k(v) & \text{for } \theta' \in [(k-1)\pi/N, k\pi/N] , \\ \vdots & \\ f_N(v) & \text{for } \theta' \in [(N-1)\pi/N, \pi] . \end{cases} \quad (7.19)$$

We consider for simplicity only a discretisation in $\cos \theta'$, though this can be extended to an additional discretisation in ϕ' if required.

The motivation for this description is that the simplest signal (beyond an isotropic $N = 1$ signal) which can be observed with a directional detectors is a discrete asymmetry (between the event rates in, say, the forward and backward directions). Shortly after the confirmation of a dark matter signal at a directional detector, the number of events may still be quite small (for example, the roughly 10 events required to distinguish from an isotropic background). In this small statistics scenario, constraining a large number of free functions is not feasible. However, if we discretise $f(\mathbf{v})$ into $N = 2$ angular components, it should be possible to extract some meaningful directional information with only a small number of events. With larger numbers of events, N can be increased to allow more directional information to be extracted. **Improve justification...**

Because angular information is being lost from the velocity distribution, we cannot consider using the full Radon transform to constrain the functions $f_k(v)$, as this contains additional angular information. Instead, we should consider integrated Radon transforms of the form:

$$\hat{f}_k(v_{\min}) = \int_{\phi=0}^{2\pi} \int_{(k-1)\pi/N}^{k\pi/N} \hat{f}(v_{\min}, \hat{\mathbf{q}}) d \cos \theta d\phi, \quad (7.20)$$

where $\hat{\mathbf{q}} = (\cos \theta, \phi)$. Thus, we will be using a discretised version of the Radon transform (or equivalently, the event rate and, ultimately, data) in order to constrain the functional form of a discretised velocity distribution.

Improve this justification and/or swap this paragraph with the one before it...

What form should be used for the free functions $f_k(v)$? This discretisation scheme does not depend on choosing a particular form for the v dependence of the velocity distribution. We can therefore choose any parametrisation for $f_k(v)$ - such as those described in Sec. ?? - having convinced ourselves that they introduce no bias into the fitting procedure. The question we will address here is what *angular* errors are introduced by such a discretisation. We will now demonstrate for the cases of $N = 1, 2, 3$ how the corresponding Radon transform is calculated and how it compares to the true Radon transform for some benchmark cases.

Talk somewhere about tomography...

7.5.1 $N = 1$ discretisation

The $N = 1$ case corresponds to the assumption that $f(\mathbf{v})$ is isotropic. That is, we could consider setting $f(\mathbf{v})$ equal to its angular average: $f(\mathbf{v}) = \bar{f}(v) \equiv \frac{1}{4\pi} \int f(\mathbf{v}) d\Omega_v$. The Radon transform then reduces to

$$\hat{f}(v_{\min}, \hat{\mathbf{q}}) = \int \delta(v_{\min} - \mathbf{v} \cdot \hat{\mathbf{q}}) \bar{f}(v) d^3\mathbf{v}. \quad (7.21)$$

We can rewrite the delta function as

$$\delta(v_{\min} - \mathbf{v} \cdot \hat{\mathbf{q}}) = \frac{1}{v} \delta(v_{\min}/v - \hat{\mathbf{v}} \cdot \hat{\mathbf{q}}), \quad (7.22)$$

which means that Eq. 7.21 becomes

$$\hat{f}(v_{\min}, \hat{\mathbf{q}}) = \int_{v=0}^{\infty} \frac{v^2 \bar{f}(v)}{v} \oint \delta(v_{\min}/v - \hat{\mathbf{v}} \cdot \hat{\mathbf{q}}) d\Omega_v dv. \quad (7.23)$$

The angular integral evaluates to unity as long as $v_{\min}/v = \hat{\mathbf{v}} \cdot \hat{\mathbf{q}}$ for some value of $\hat{\mathbf{v}}$ in the domain of integration. Because we integrate over all directions $\hat{\mathbf{v}}$, this is guaranteed to be satisfied for some value, as long as $v > v_{\min}$ (because $\hat{\mathbf{v}} \cdot \hat{\mathbf{q}}$ cannot exceed unity). Thus,

$$\oint \delta(v_{\min}/v - \hat{\mathbf{v}} \cdot \hat{\mathbf{q}}) d\Omega_v = \Theta(v - v_{\min}), \quad (7.24)$$

and

$$\hat{f}(v_{\min}, \hat{\mathbf{q}}) = \int_{v=v_{\min}}^{\infty} \frac{v^2 \bar{f}(v)}{v} dv. \quad (7.25)$$

Finally, to obtain the directionally averaged Radon transform $\hat{f}(v_{\min})$, we integrate over all directions $\hat{\mathbf{q}}$. As the Radon transform is isotropic in

this case, this gives a contribution of 4π . Replacing the expression for $\bar{f}(v)$ with the directionally averaged velocity distribution, we therefore obtain

What should I call the directionally averaged RT?

$$\hat{f}(v_{\min}) = \int_{v=v_{\min}}^{\infty} \frac{f(\mathbf{v})}{v} d^3\mathbf{v}. \quad (7.26)$$

This matches the expression for the total non-directional scattering rate. While we assumed here that $f(v)$ was isotropic, in first deriving this expression in Chapter ??, no such assumption was required **Was it?**. We therefore see that in the $N = 1$ case, the angular-discretised ‘approximation’ is in fact exact and leads to the correct angular-averaged Radon transform.

7.5.2 $N = 2$ discretisation

For the $N = 2$ case, we are considering a forward-backward asymmetry in the velocity distribution:

$$f(\mathbf{v}) = \begin{cases} f_1(v) & \text{if } \theta' \in [0, \pi/2] \\ f_2(v) & \text{if } \theta' \in [\pi/2, \pi]. \end{cases} \quad (7.27)$$

From these, we wish to obtain the integrated recoil spectra for the forward and back directions. Specifically:

$$\hat{f}_1 = \int_0^1 \hat{f}(v_q, \cos \theta) d \cos \theta \quad (7.28)$$

$$\hat{f}_2 = \int_{-1}^0 \hat{f}(v_q, \cos \theta) d \cos \theta. \quad (7.29)$$

We will focus on the first of these, \hat{f}_1 , as the other can be obtained simply by exchanging which directions are forward and backward (that is, by interchanging f_1 and f_2). From now on, we will therefore be working under the assumption that $\cos \theta \in [0, 1]$.

We first consider calculating the azimuthally averaged Radon transform:

$$\hat{f}(v_q, \cos \theta) = \int_0^{2\pi} \hat{f}(v_q, \cos \theta, \phi) d\phi \quad (7.30)$$

$$= \int_0^{2\pi} \left(\int_{\mathbb{R}^3} f(\mathbf{v}) \delta(\mathbf{v} \cdot \hat{\mathbf{q}} - v_q) d^3\mathbf{v} \right) d\phi \quad (7.31)$$

$$= \int_{\phi=0}^{2\pi} \int_{v=0}^{\infty} \oint v f(\mathbf{v}) \delta(v_{\min}/v - \hat{\mathbf{v}} \cdot \hat{\mathbf{q}}) d\Omega_v dv d\phi. \quad (7.32)$$

We focus on performing the ϕ integral, which we define as:

$$I(v_q, \cos \theta, \mathbf{v}) = \int_0^{2\pi} \delta(\sin \theta \sin \theta' \cos(\phi - \phi') + \cos \theta \cos \theta' - v_q/v) d\phi \quad (7.33)$$

$$\equiv \int_0^{2\pi} \delta(g(\phi)) d\phi. \quad (7.34)$$

We then rewrite the delta function as a function of ϕ :

$$\delta(g(\phi)) = \sum_i \frac{\delta(\phi - \phi_i)}{|g'(\phi_i)|}. \quad (7.35)$$

Here, we sum over those values of ϕ_i satisfying $g(\phi_i) = 0$. We leave the details of the full calculation to Appendix ???. However, we obtain,

$$I(v_q, \cos \theta, \mathbf{v}) = \frac{2C(\alpha)}{\sqrt{(\sin \theta \sin \theta')^2 - (\beta - \cos \theta \cos \theta')^2}} \Theta(v - v_q), \quad (7.36)$$

where

$$\beta = v_q/v; \quad \alpha = \frac{\beta - \cos \theta \cos \theta'}{\sin \theta \sin \theta'}, \quad (7.37)$$

and $C(\alpha) = 1$ for $\alpha \in [-1, 1]$ and vanishing otherwise.

We therefore obtain

$$\hat{f}(v_q, \cos \theta) = \int_{v=v_q}^{\infty} \int_{\cos \theta=-1}^1 \int_{\cos \theta'=-1}^1 f(v, \cos \theta') I(v_q, \cos \theta, v, \cos \theta') v dv d\cos \theta d\cos \theta', \quad (7.38)$$

with

$$f(v, \cos \theta') = \int_0^{2\pi} f(v, \cos \theta', \phi') d\phi'. \quad (7.39)$$

Leave a load of the details for the appendix

In the $N = 2$ case, we obtain

$$\hat{f}_1 = 4\pi \int_{v_q}^{\infty} v \left(\pi f_1(v) + \tan^{-1} \left\{ \frac{\sqrt{1-\beta^2}}{\beta} \right\} (f_2(v) - f_1(v)) \right) dv \quad (7.40)$$

$$\hat{f}_2 = 4\pi \int_{v_q}^{\infty} v \left(\pi f_2(v) + \tan^{-1} \left\{ \frac{\sqrt{1-\beta^2}}{\beta} \right\} (f_1(v) - f_2(v)) \right) dv. \quad (7.41)$$

We have also checked using Monte Carlo calculations that these are the correct forms of the forward and backward averaged Radon transforms in the case of a discretised velocity distribution.

We now wish to compare these approximate Radon transforms with the Radon transforms obtained from the full (non-discretised) velocity distribution. To do this, we select a benchmark velocity distribution (such as the SHM) and calculate $f_{1,2}$ according to Eq. 7.27 by averaging over the $\cos \theta'$ in the forward and backward directions. This discretised velocity distribution is shown in Fig. 7.5.2. We then insert these into Eq. 7.40 to obtain the forward and backward Radon transform. For comparison, we use the full velocity distribution of Eq. 7.15 to obtain the *true* forward and backward Radon transforms by integrating over $\cos \theta$.

The results of this comparison for a SHM model with $v_{\text{lag}} = 220 \text{ km s}^{-1}$ and $\sigma_v = 156 \text{ km s}^{-1}$ are shown in Fig. 7.5.2. While the general features are reproduced, there are some discrepancies. In particular, the forward Radon transform obtained using the approximate method is roughly 80% of the correct result, while the backward Radon transform is up to 100% larger using the approximate method. The reason for this is clear from Fig. 7.5.2, which shows that the discretised velocity distribution has a greater fraction of WIMPs with velocities at right angles to the forward direction ($\theta' = 0$). Thus, the discretised velocity distribution has a greater chance of producing scatters in the backward direction. Overall, the discretised distribution is less focused in the forward direction, resulting in a reduced asymmetry between the forward and backward scattering rates.

These discrepancies between the true and approximate recoil spectra may prove problematic when this method is employed in parameter estimation and the reconstruction of $f(\mathbf{v})$. However, these discrepancies should be reduced when the finite angular resolution of detectors is taken into account. *Mention finite angular resolution...Do some plots...*

Consider a more radical distribution - such as a stream and show that it doesn't work so well...

7.5.3 $N = 3$ discretisation

Given the discrepancies in the $N = 2$ case, we will now consider the $N = 3$ discretisation, which should improve the fit between the true and approximate distribution. In addition, the $N = 3$ will allow us to employ this methodology to the case where sense discrimination of recoils is not possible. Without sense discrimination, the forward and backward directions cannot be distinguished and the $N = 2$ discretisation provides no directional sensitivity. As we shall see shortly, directional sensitivity is possible in the $N = 3$ case.

We write the velocity distribution in discretised form as

$$f(\mathbf{v}) = \begin{cases} f_1(v) & \text{if } \theta' \in [0, \pi/3] \\ f_2(v) & \text{if } \theta' \in [\pi/3, 2\pi/3] \\ f_3(v) & \text{if } \theta' \in [2\pi/3, \pi]. \end{cases} \quad (7.42)$$

If we interpret this discretisation as an averaging of the underlying velocity distribution, as before, we obtain the distribution in the bottom panel of Fig. 7.5.3 (the full SHM distribution is shown in the top panel for reference). Following the same procedure as for the $N = 2$ case, we can obtain the corresponding forward, backward and transverse Radon transforms. The exact form of these is complicated (and not particularly instructive). However, this form can be generated using the algorithm described in Sec. ??, in which we treat the case of general N .

Again, we wish to test how closely the $N = 3$ discretised distribution can reproduce the true forward-, backward- and transverse-averaged Radon transforms. The results are shown in Fig. 7.5.2. Compared to the $N = 2$ case, the recoil spectra are reproduced much more closely, with a discrepancy of at most 15% **check** between the true and approximate distributions.

Emphasise that we haven't included the form factors...

The folded distribution

As discussed in Sec. 7.3, sense discrimination between forward and backward-going recoils may not be possible with near-future detectors. In this case

then, all that can be measured is the so called ‘folded’ recoil spectrum

$$\frac{dR}{dE_R d|\cos\theta|} = \frac{dR}{dE_R d\cos\theta} + \frac{dR}{dE_R d(-\cos\theta)}. \quad (7.43)$$

As a result, we are concerned not will the full Radon transform of $f(\mathbf{v})$, but the folded Radon transform $\hat{f}(v_q, |\cos\theta|)$. In the case of $N = 2$ discretisation, this folded Radon transform would have no directional information (because the forward and backward scattering rates differ only in the sign of $\cos\theta$). However, in the $N = 3$ case, the transverse Radon transform, given by **define this earlier in the text...**

$$\hat{f}_T(v_q) = \hat{f}_2(v_q) = \int_{-1/2}^{1/2} \hat{f}(v_q, \cos\theta) d\cos\theta, \quad (7.44)$$

is invariant under $\hat{f}(v_q, \cos\theta) \rightarrow \hat{f}(v_q, |\cos\theta|)$ (apart from an overall factor of 2). That is, the transverse event rate ‘folds’ back onto itself. Thus, even without sense discrimination, directional experiments will still be sensitive to this transverse scattering rate. By comparison, if the forward and backward directions cannot be distinguished, the remaining two averaged Radon transforms (the top two panels in Fig. 7.5.3) are folded together, to obtain the longitudinal rate

$$\hat{f}_L(v_q) = \int_{-1}^{-1/2} \hat{f}(v_q, \cos\theta) d\cos\theta + \int_{1/2}^1 \hat{f}(v_q, \cos\theta) d\cos\theta. \quad (7.45)$$

We plot the transverse and longitudinal averaged in Fig. 7.5.3. **Need a factor of 2 in the transverse bit...?** As expected, the two rates are now more similar in shape as we have lost some directional information. The approximate Radon transforms, obtained from the discretisation, match the true transforms closely for speeds above $v_q \approx 200 \text{ km s}^{-1}$. **Why the discrepancy at low v ?** For realistic experiments, these low speeds will be below the threshold energy of the experiment and the bias introduced by this discrepancy should be minimal **find some numbers for this...**

We note that in this folded case, we would fit to two functions, corresponding to the longitudinal and transverse event rates. However, our original discretisation required 3 free functions of v : $f_{1,2,3}(v)$. However, due to the properties of the Radon transform (**which are...?**), the longitudinal rate is not a function of $f_1(v)$ and $f_3(v)$ but of the sum $f_1(v) + f_3(v) \equiv f_L(v)$. Thus, we have only two free functions to fit $f_{L,T}(v)$.

-Fix captions on figures...

-Discuss a dark disk case...

-Discuss the poorly aligned - off axis case...

7.6 Discretisation for general N

The procedure which has been described above can be extended to any number N of angular bins. Significantly, for any value of N , the resulting Radon transform remains a sum of elementary, analytic functions multiplied by one dimensional functions $f_k(v)$. This means that no angular integration must be performed in order to obtain the Radon transform and at most N one-dimensional integrals over the velocity v must be performed, one for each of the $\hat{f}_k(v_q)$.

While the details of the calculation can be found in Appendix ??, we show below the full algorithm for calculating the averaged Radon transforms from a velocity distribution discretised into N angular pieces...

FINISH

7.7 Conclusion

Check consistency with v_{min} and $v_q...$, be careful about f 's with subscript 1

Check notation consistency with lefts(and rights) **We can even combine this with the non-directional experiments...**

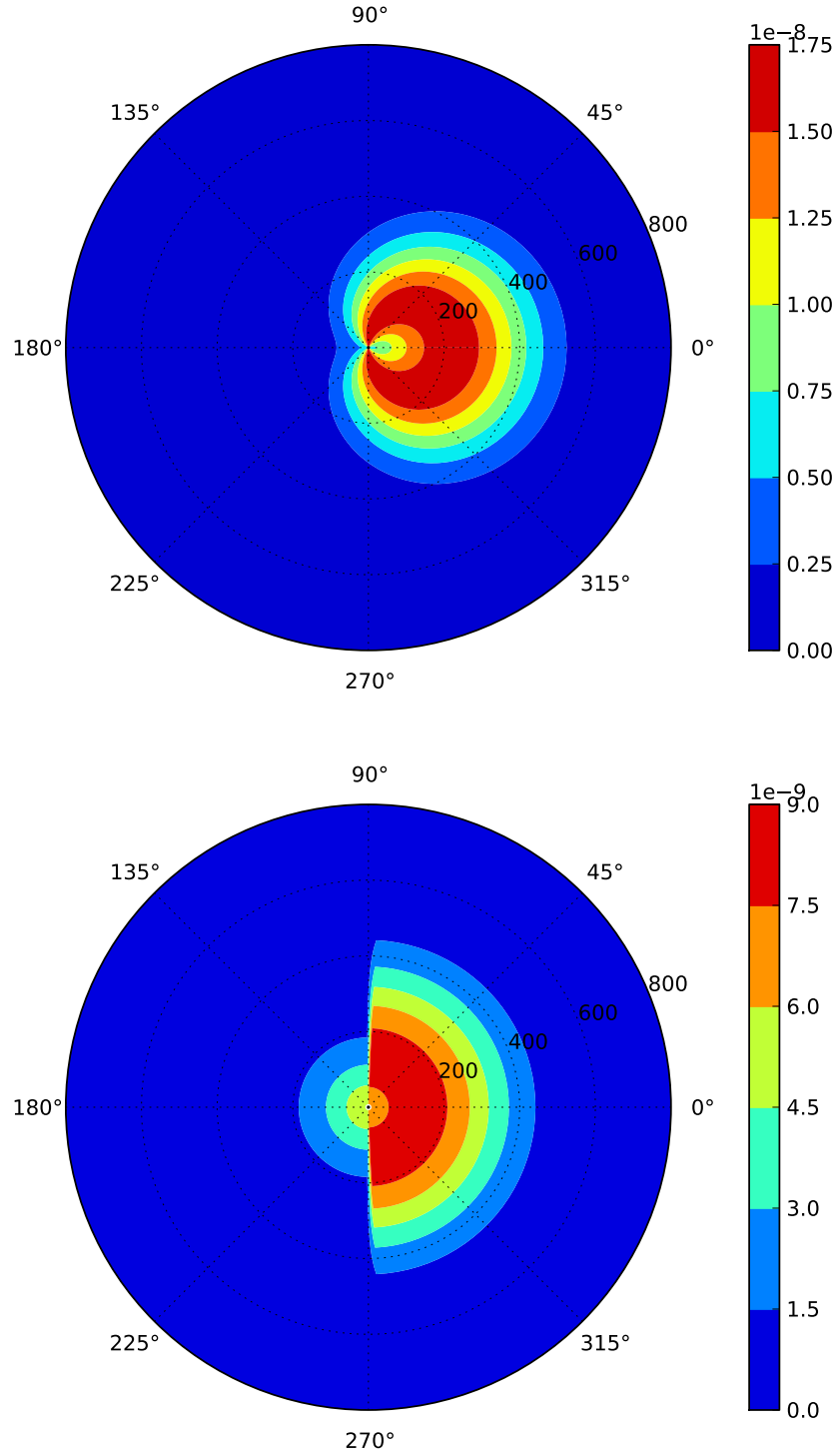


Figure 7.3: Polar plots in (v, θ') for two velocity distributions. Shown are the SHM velocity distribution for $v_{\text{lag}} = 220 \text{ km s}^{-1}$ and $\sigma_v = 156 \text{ km s}^{-1}$ (top) and the discretised SHM distribution obtained by averaging in the forward and backward directions (bottom). The vector \mathbf{v}_{lag} is aligned along $\theta' = 0$. Note the different color scales in the two plots.

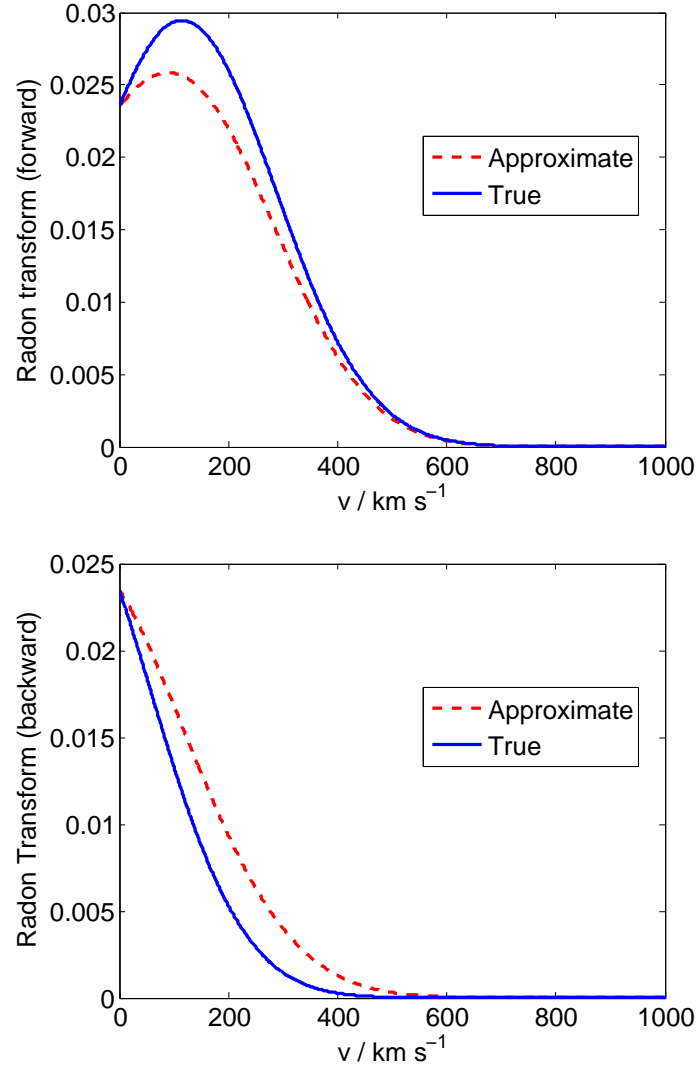


Figure 7.4: True and approximate forward and backward radon transforms when the full velocity distribution is discretised into $N = 2$ directional pieces. **Finish**

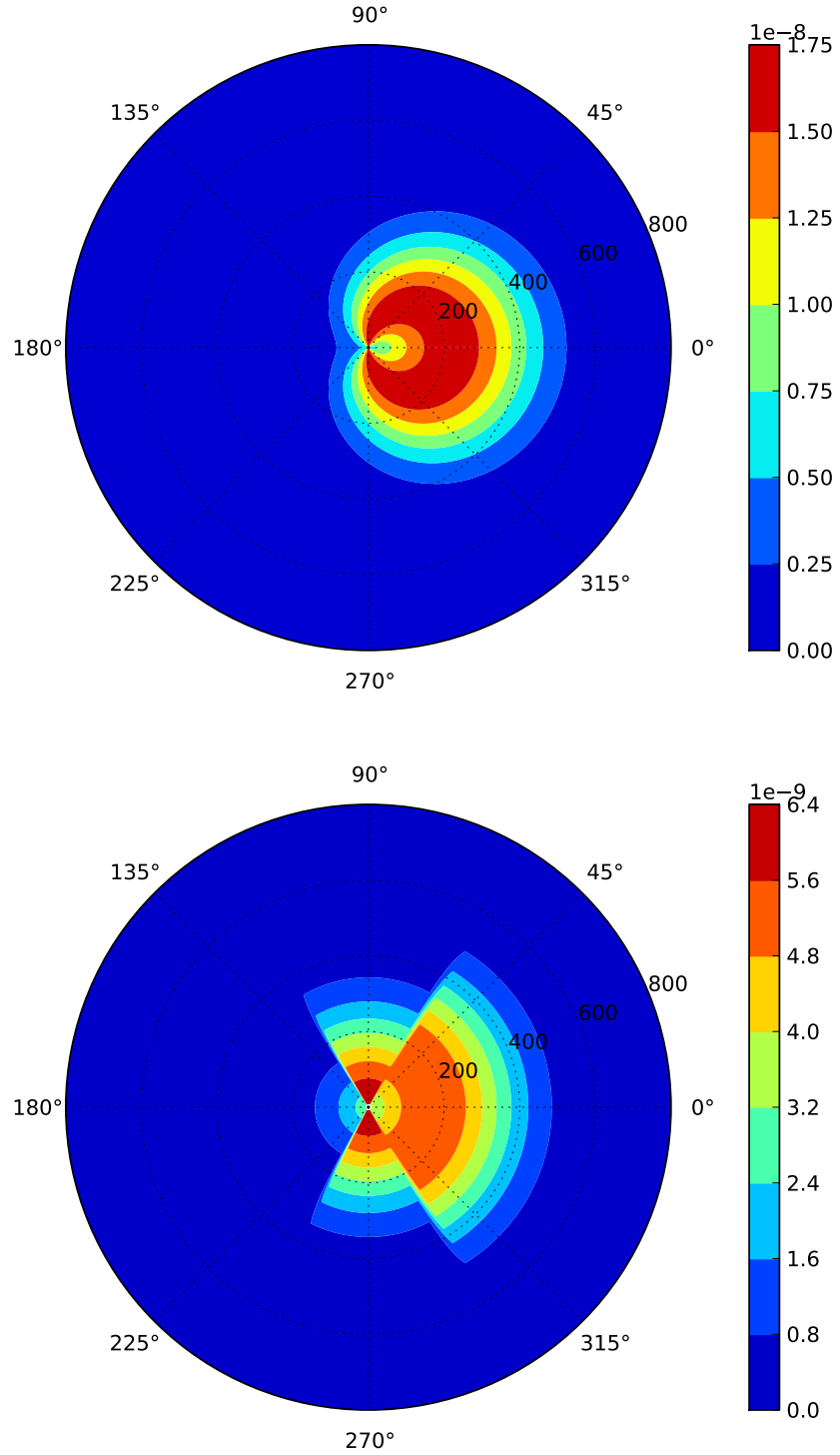


Figure 7.5: Polar plots in (v, θ') for two velocity distributions. Shown are the SHM velocity distribution for $v_{\text{lag}} = 220 \text{ km s}^{-1}$ and $\sigma_v = 156 \text{ km s}^{-1}$ (top) and the discretised SHM distribution obtained by averaging in the forward, backward and transverse directions (bottom). The vector \mathbf{v}_{lag} is aligned along $\theta' = 0$. Note the different color scales in the two plots.

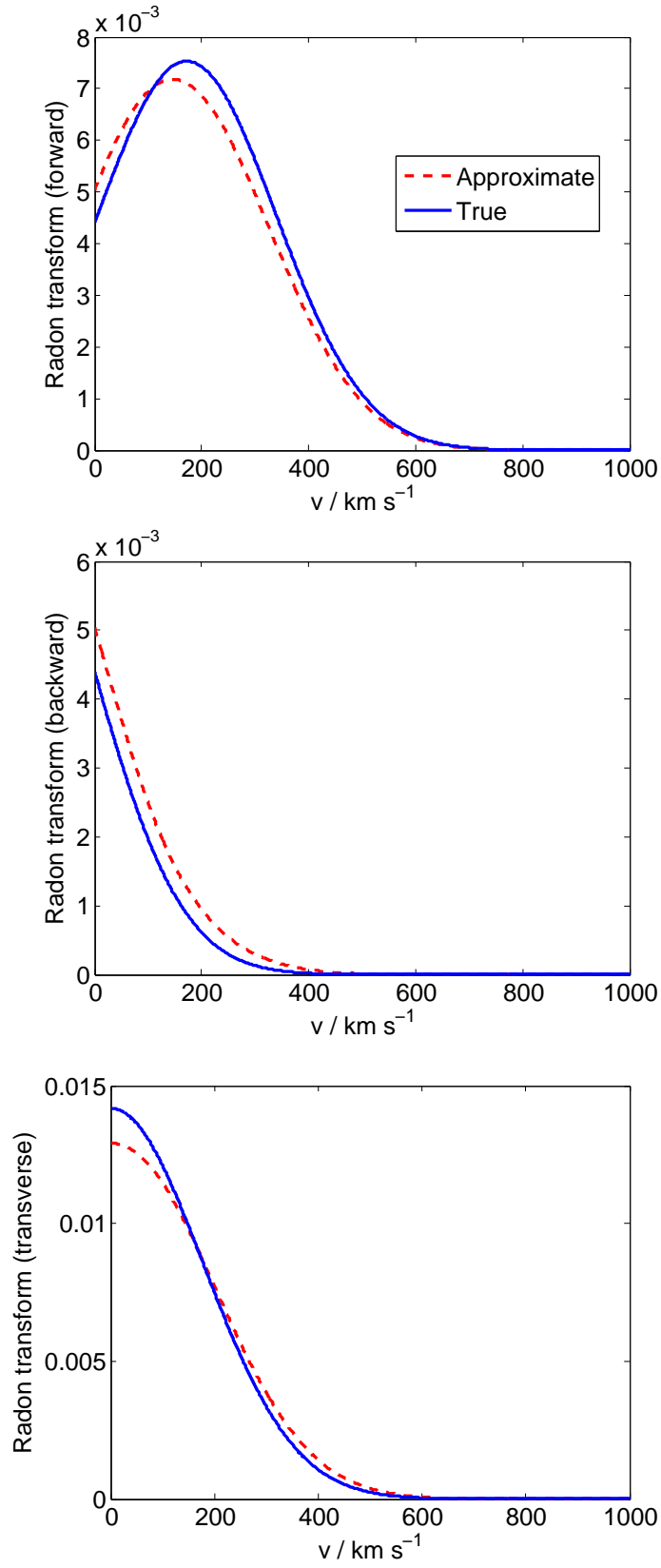


Figure 7.6: True and approximate transforms when the full velocity distribution is discretised into $N = 3$ directional pieces. In the ‘forward’ case $\cos \theta \in [1/2, 1]$, in the ‘backward’ case $\cos \theta \in [-1, -1/2]$, and in the ‘transverse case’ $\cos \theta \in [-1/2, 1/2]$.

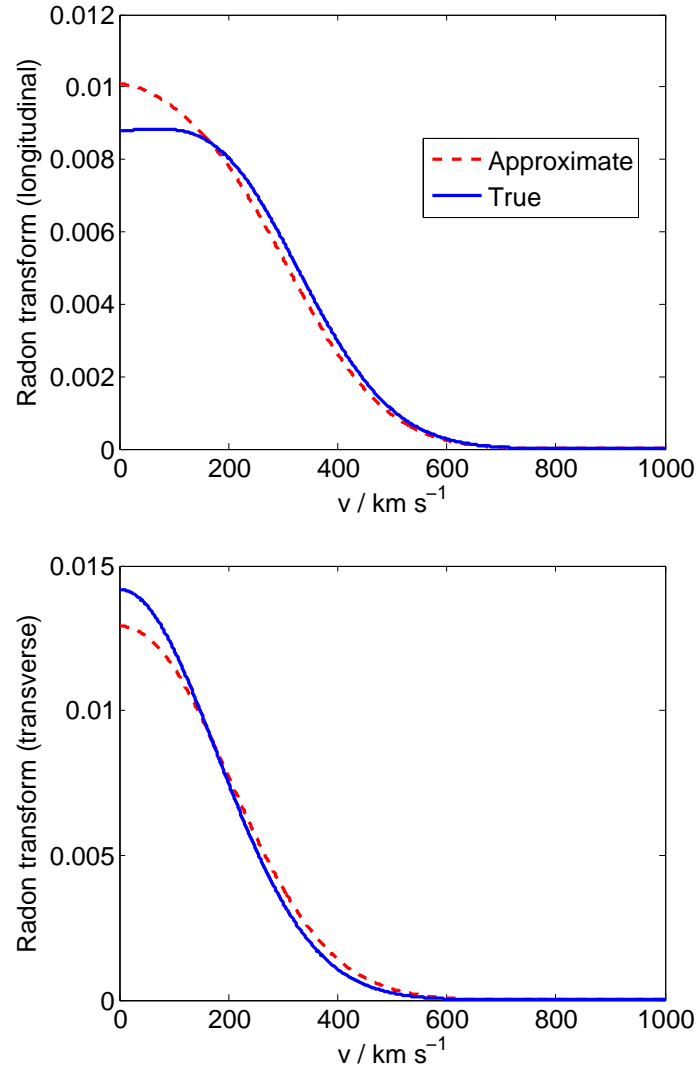


Figure 7.7: True and approximate folded transforms when the full velocity distribution is discretised into $N = 3$ directional pieces. In the ‘longitudinal’ case $|\cos \theta| \in [1/2, 1]$ while in the ‘transverse case’ $|\cos \theta| \in [0, 1/2]$.

Chapter 8

Conclusions

Bibliography

- [1] A. H. G. Peter, Phys. Rev. D **83**, 125029 (2011), arXiv:1103.5145 .
- [2] A. G. Riess, *et al.*, Astrophys. J. **116**, 1009 (1998), astro-ph/9805201 .
- [3] S. Perlmutter, *et al.*, Astrophys. J. **517**, 565 (1999), astro-ph/9812133 .
- [4] E. W. Kolb and M. S. Turner, *The Early Universe* (Addison-Wesley, Reading, Massachusetts, 1990) Chap. 9.
- [5] G. R. Blumenthal, S. M. Faber, J. R. Primack, and M. J. Rees, Nature **311**, 517 (1984).
- [6] G. Hinshaw, *et al.*, Astrophys. J. Suppl. Ser. **208**, 19+ (2013).
- [7] C. J. MacTavish, *et al.*, Astrophys. J. **647**, 799 (2005), astro-ph/0507503 .
- [8] K. S. Dawson, *et al.*, Astron. J. **145**, 10+ (2013).
- [9] P. A. R. Ade, *et al.* (BICEP2 Collaboration), (2014), arXiv:1403.3985 .
- [10] T. D. Kitching, *et al.*, (2014), arXiv:1401.6842 .
- [11] L. Fu, *et al.*, “CFHTLenS: Cosmological constraints from a combination of cosmic shear two-point and three-point correlations,” (2014), arXiv:1404.5469 .
- [12] D. G. York, *et al.*, Astron. J. **120**, 1579 (2000), arXiv:astro-ph/0006396 .
- [13] N. Suzuki, *et al.*, Astrophys. J. **746**, 85+ (2011), arXiv:1105.3470 .

- [14] P. A. R. Ade *et al.* (Planck Collaboration), (2013), arXiv:1303.5062 .
- [15] P. A. R. Ade *et al.* (Planck Collaboration), *Astron. Astrophys.* (2014), arXiv:1303.5076 .
- [16] F. Zwicky, *Helv. Phys. Acta.* **6**, 110 (1933).
- [17] J. S. Sanders, A. C. Fabian, E. Churazov, A. A. Schekochihin, A. Simionescu, S. A. Walker, and N. Werner, *Science* **341**, 1365 (2013), arXiv:1309.4866 .
- [18] R. Fusco-Femiano and J. P. Hughes, *Astrophys. J.* **429**, 545+ (1994).
- [19] N. Makino, *Publ. Astron. Soc. Jpn.* **46**, 139 (1994).
- [20] N. Okabe, G. P. Smith, K. Umetsu, M. Takada, and T. Futamase, *Astrophys. J.* **769**, L35 (2013), arXiv:1302.2728 .
- [21] S. Ettori, A. Donnarumma, E. Pointecouteau, T. H. Reiprich, S. Giodini, L. Lovisari, and R. W. Schmidt, *Space Sci. Rev.* **177**, 119 (2013), arXiv:1303.3530 .
- [22] R. G. Carlberg, H. K. C. Yee, E. Ellingson, R. Abraham, P. Gravel, S. Morris, and C. J. Pritchet, *Astrophys. J.* **462**, 32+ (1996), arXiv:astro-ph/9509034 .
- [23] V. Springel, *et al.*, *Nature* **435**, 629 (2005), arXiv:astro-ph/0504097 .
- [24] J. Diemand, M. Kuhlen, and P. Madau, *Astrophys. J.* **657**, 262 (2006), astro-ph/0611370 .
- [25] V. Springel, J. Wang, M. Vogelsberger, A. Ludlow, A. Jenkins, A. Helmi, J. F. Navarro, C. S. Frenk, and S. D. M. White, *Mon. Not. R. Astron. Soc.* **391**, 1685 (2008), arXiv:0809.0898 .
- [26] P. Mollitor, E. Nezri, and R. Teyssier, “Baryonic and dark matter distribution in cosmological simulations of spiral galaxies,” (2014), arXiv:1405.4318 .
- [27] M. Vogelsberger, S. Genel, V. Springel, P. Torrey, D. Sijacki, D. Xu, G. Snyder, S. Bird, D. Nelson, and L. Hernquist, *Nature* **509**, 177 (2014), arXiv:1405.1418 .

- [28] M. Vogelsberger, S. Genel, D. Sijacki, P. Torrey, V. Springel, and L. Hernquist, *Mon. Not. R. Astron. Soc.* **436**, 3031 (2013), arXiv:1305.2913 .
- [29] D. Martizzi, R. Teyssier, B. Moore, and T. Wentz, *Mon. Not. R. Astron. Soc.* **422** (2012), arXiv:1112.2752 .
- [30] A. Pillepich, M. Kuhlen, J. Guedes, and P. Madau, *Astrophys. J.* **784**, 161+ (2014), arXiv:1308.1703 .
- [31] G. Stinson, J. Bailin, H. Couchman, J. Wadsley, S. Shen, C. Brook, and T. Quinn, *Mon. Not. R. Astron. Soc.* **408**, 812 (2010), arXiv:1004.0675 .
- [32] M. L. Norman and G. L. Bryan, “Cosmological adaptive mesh refinement,” in *Numerical Astrophysics 1998*, Vol. 240, edited by S. M. Miyama, K. Tomisaka, and T. Hanawa (Springer Netherlands, Dordrecht, 1999) Chap. 3, pp. 19–28, arXiv:astro-ph/9807121 .
- [33] V. Springel, *Mon. Not. R. Astron. Soc.* **401**, 791 (2010), arXiv:0901.4107 .
- [34] K. Begeman, A. Broeils, and R. Sanders, *Mon. Not. R. Astron. Soc.* **249**, 523 (1991).
- [35] M. Persic, P. Salucci, and F. Stel, *Mon. Not. R. Astron. Soc.* **281**, 27 (1996), astro-ph/9506004 .
- [36] A. Bosma, *Astron. J.* **86**, 1791+ (1981).
- [37] A. Bosma, *Astron. J.* **86**, 1825+ (1981).
- [38] A. J. Deason, V. Belokurov, N. W. Evans, and J. An, *Mon. Not. R. Astron. Soc.: Lett.* **424**, L44 (2012), arXiv:1204.5189 .
- [39] M. López-Corredoira, *Astron. Astrophys.* **563**, A128+ (2014), arXiv:1402.3551 .
- [40] P. Bhattacharjee, S. Chaudhury, and S. Kundu, *Astrophys. J.* **785**, 63+ (2014), arXiv:1310.2659 .
- [41] G. Kauffmann, S. D. White, and B. Guiderdoni, *Mon. Not. R. Astron. Soc.* **264**, 201 (1993).

- [42] M. G. Walker, M. Mateo, E. W. Olszewski, J. Peñarrubia, N. W. Evans, and G. Gilmore, *Astrophys. J.* **704**, 1274+ (2009).
- [43] V. Belokurov, *et al.*, *Astrophys. J. Lett.* **712**, L103 (2010), arXiv:1002.0504 .
- [44] A. Klypin, A. V. Kravtsov, O. Valenzuela, and F. Prada, *Astrophys. J.* **522**, 82 (1999).
- [45] M. Boylan-Kolchin, J. S. Bullock, and M. Kaplinghat, *Mon. Not. R. Astron. Soc. Lett.* **415**, L40 (2011), arXiv:1103.0007 .
- [46] S. Garrison-Kimmel, M. Boylan-Kolchin, J. S. Bullock, and E. N. Kirby, (2014), arXiv:1404.5313 .
- [47] W. J. G. de Blok, *Adv. Astron.* **2010**, 1 (2010), arXiv:0910.3538 .
- [48] J. Dubinski and R. G. Carlberg, *Astrophys. J.* **378**, 496+ (1991).
- [49] J. F. Navarro, C. S. Frenk, and S. D. M. White, *Astrophys. J.* **462**, 563+ (1996), arXiv:astro-ph/9508025 .
- [50] P. Salucci, *Mon. Not. R. Astron. Soc.* **320**, L1 (2001).
- [51] F. Donato, G. Gentile, and P. Salucci, *Mon. Not. R. Astron. Soc.* **353**, L17 (2004), arXiv:astro-ph/0403206 .
- [52] E. Hayashi, J. F. Navarro, C. Power, A. Jenkins, C. S. Frenk, S. D. M. White, V. Springel, J. Stadel, and T. R. Quinn, *Mon. Not. R. Astron. Soc.* **355**, 794 (2004), arXiv:astro-ph/0310576 .
- [53] M. Gritschneider and D. N. C. Lin, *Astrophys. J.* **765**, 38+ (2013).
- [54] N. C. Amorisco, J. Zavala, and T. J. L. de Boer, *Astrophys. J.* **782**, L39+ (2014), arXiv:1309.5958 .
- [55] A. Del Popolo, J. A. S. Lima, J. C. Fabris, and D. C. Rodrigues, “A unified solution to the small scale problems of the λ cdm model,” (2014), arXiv:1404.3674 .
- [56] B. Moore, T. Quinn, F. Governato, J. Stadel, and G. Lake, *Mon. Not. R. Astron. Soc.* **310**, 1147 (1999), astro-ph/9903164 .

- [57] P. Bode, J. P. Ostriker, and N. Turok, *Astrophys. J.* **556**, 93 (2001), astro-ph/0010389 .
- [58] A. V. Macciò and F. Fontanot, *Mon. Not. R. Astron. Soc. Lett.* **404**, L16 (2010).
- [59] A. Kudo and M. Yamaguchi, *Phys. Lett. B* **516**, 151 (2001).
- [60] M. L. Perl, P. C. Kim, V. Halyo, E. R. Lee, I. T. Lee, D. Loomba, and K. S. Lackner, *Int. J. Mod. Phys. A* **16**, 2137 (2001), hep-ex/0102033 .
- [61] S. N. Gninenko, N. V. Krasnikov, and A. Rubbia, *Phys. Rev. D* **75**, 075014 (2007), hep-ph/0612203 .
- [62] A. Melchiorri, A. Polosa, and A. Strumia, *Phys. Lett. B* **650**, 416 (2007), hep-ph/0703144 .
- [63] P. Natarajan, A. Loeb, J.-P. Kneib, and I. Smail, *Astrophys. J.* **580**, L17 (2002), astro-ph/0207045 .
- [64] X. Chen, S. Hannestad, and R. J. Scherrer, *Phys. Rev. D* **65**, 123515 (2002), astro-ph/0202496 .
- [65] S. D. L. Amigo, W. M. Cheung, Z. Huang, and S.-P. Ng, *J. Cosmol. Astropart. Phys.* **2009**, 005 (2009), arXiv:0812.4016 .
- [66] N. F. Bell, A. J. Galea, and K. Petraki, *Phys. Rev. D* **82** (2010), arXiv:1004.1008 .
- [67] M. Taoso, G. Bertone, and A. Masiero, *J. Cosmol. Astropart. Phys.* **03**, 022 (2008), arXiv:0711.4996 .
- [68] J. R. Bond and A. S. Szalay, *Astrophys. J.* **274**, 443 (1983).
- [69] D. Boyanovsky, H. J. de Vega, and N. Sanchez, *Phys. Rev. D* **78** (2008), arXiv:0807.0622 .
- [70] V. K. Narayanan, D. N. Spergel, R. Davé, and C.-P. Ma, *The Astrophysical Journal* **543**, L103 (2000), astro-ph/0005095 .
- [71] K. Abazajian, E. R. Switzer, S. Dodelson, K. Heitmann, and S. Habib, *Phys. Rev. D* **71**, 043507 (2005), astro-ph/0411552 .

- [72] R. de Putter, *et al.*, *Astrophys. J.* **761**, 12+ (2012), arXiv:1201.1909 .
- [73] D. Feldman, Z. Liu, P. Nath, and G. Peim, *Phys. Rev. D* **81**, 095017 (2010), arXiv:1004.0649 .
- [74] G. Gelmini and P. Gondolo, “DM production mechanisms,” in *Particle Dark Matter*, edited by G. Bertone (Cambridge University Press, Cambridge, 2010) Chap. 7, pp. 121–141, arXiv:1009.3690 .
- [75] K. Griest, *Phys. Rev. D* **43**, 3191 (1991).
- [76] L. J. Hall, K. Jedamzik, J. March-Russell, and S. M. West, *J. High Energy Phys.* **2010** (2010), arXiv:0911.1120 .
- [77] D. J. H. Chung, E. W. Kolb, and A. Riotto, *Phys. Rev. D* **59** (1998), hep-ph/9802238 .
- [78] V. A. Kuzmin and I. I. Tkachev, *JETP Lett.* **68**, 271 (1998), hep-ph/9802304 .
- [79] T. Gherghetta, G. F. Giudice, and J. D. Wells, *Nucl. Phys. B* **559**, 27 (1999), hep-ph/9904378 .
- [80] D. Tytler, J. M. O’Meara, N. Suzuki, and D. Lubin, *Physica Scripta* **T85**, 12+ (2000), arXiv:astro-ph/0001318 .
- [81] B. Fields and S. Sarkar, *J. Phys. G.* **33**, 1 (2006), astro-ph/0601514 .
- [82] M. Maggiore, *Phys. Rep.* **331**, 283 (2000), gr-qc/9909001 .
- [83] R. H. Cyburt, B. D. Fields, K. A. Olive, and E. Skillman, *J. Astropart. Phys.* **23**, 313 (2005), astro-ph/0408033 .
- [84] K. Jedamzik, *Phys. Rev. D* **74** (2006), hep-ph/0604251 .
- [85] G. Jungman, M. Kamionkowski, and K. Griest, *Phys. Rep.* **267**, 195 (1995), hep-ph/9506380 .
- [86] G. L. Kane and S. P. Martin, “A supersymmetry primer,” in *Perspectives on Supersymmetry II*, Vol. 21 (WORLD SCIENTIFIC, Singapore, 2011) pp. 1–153, hep-ph/9709356 .

- [87] J. Ellis, J. S. Hagelin, D. V. Nanopoulos, K. Olive, and M. Srednicki, Nucl. Phys. B **238**, 453 (1984).
- [88] B. Shakya, “The status of neutralino dark matter,” (2013), arXiv:1312.7505 .
- [89] K.-Y. Choi and O. Seto, Phys. Rev. D **88**, 035005 (2013), arXiv:1305.4322 .
- [90] E. W. Kolb, D. J. H. Chung, and A. Riotto, “Wimpzillas!” in *DARK98: Proceedings of the Second International Conference on Dark Matter in Astro and Particle Physics*, edited by H. V. Klapdor-Kleingrothaus and L. Baudis (AIP, 1999) pp. 91–105, hep-ph/9810361 .
- [91] M. J. Duff, “Kaluza-Klein theory in perspective,” (1994), hep-th/9410046 .
- [92] T. Appelquist, H.-C. Cheng, and B. A. Dobrescu, Phys. Rev. D **64**, 035002 (2001), hep-ph/0012100 .
- [93] H.-C. Cheng, K. T. Matchev, and M. Schmaltz, Phys. Rev. D **66**, 036005 (2002), hep-ph/0204342 .
- [94] G. Servant and T. M. P. Tait, Nucl. Phys. B **650**, 391 (2002), hep-ph/0206071 .
- [95] L. Bergström, *New J. Phys.*, New Journal of Physics **11**, 105006+ (2009), arXiv:0903.4849 .
- [96] C. Amsler, *et al.*, Phys. Lett. B **667**, 1 (2008).
- [97] S. Dodelson and L. Widrow, Phys. Rev. Lett. **72**, 17 (1994), hep-ph/9303287 .
- [98] X. Shi and G. M. Fuller, Phys. Rev. Lett. **82**, 2832 (1999), astro-ph/9810076 .
- [99] T. Asaka, M. Shaposhnikov, and A. Kusenko, Phys. Lett. B **638**, 401 (2006), hep-ph/0602150 .
- [100] S. H. Hansen, J. Lesgourgues, S. Pastor, and J. Silk, Mon. Not. R. Astron. Soc. **333**, 544 (2002), arXiv:astro-ph/0106108 .

- [101] K. Abazajian and S. M. Koushiappas, Phys. Rev. D **74** (2006), arXiv:astro-ph/0605271 .
- [102] R. D. Peccei and H. R. Quinn, Phys. Rev. Lett. **38**, 1440 (1977).
- [103] G. Raffelt, “Axions in astrophysics and cosmology,” (1995), hep-ph/9502358 .
- [104] P. Sikivie and Q. Yang, Phys. Rev. Lett. **103** (2009), arXiv:0901.1106 .
- [105] C. J. Copi, D. Huterer, D. J. Schwarz, and G. D. Starkman, Adv. in Astron. **2010**, 1 (2010), arXiv:1004.5602 .
- [106] A. Arvanitaki, S. Dimopoulos, S. Dubovsky, N. Kaloper, and J. March-Russell, Phys. Rev. D **81** (2010), arXiv:0905.4720 .
- [107] J. Kumar, J. L. Feng, G. Alverson, P. Nath, and B. Nelson, AIP Conf. Proc. **1200**, 1059 (2010), arXiv:0909.2877 .
- [108] R. Foot, Int. J. Mod. Phys. A **29**, 1430013+ (2014), arXiv:1401.3965 .
- [109] A. Birkedal, A. Noble, M. Perelstein, and A. Spray, Phys. Rev. D **74** (2006), arXiv:hep-ph/0603077 .
- [110] M. Cirelli, N. Fornengo, and A. Strumia, Nucl. Phys. B **753**, 178 (2007), arXiv:hep-ph/0512090 .
- [111] L. Edelhäuser, T. Flacke, and M. Krämer, J. High Energy Phys. **2013** (2013), arXiv:1302.6076 .
- [112] T. Kakuda, K. Nishiwaki, K.-y. Oda, N. Okuda, and R. Watanabe, “Phenomenological constraints on universal extra dimensions at LHC and electroweak precision test,” (2013), arXiv:1304.6362 .
- [113] ATLAS Collaboration, https://atlas.web.cern.ch/Atlas/GROUPS/PHYSICS/CombinedSummaryPlots/SUSY/ATLAS_SUSY_Summary/ATLAS_SUSY_Summary.pdf (2013).
- [114] CMS Collaboration, https://twiki.cern.ch/twiki/pub/CMSPublic/SUSYSMSSummaryPlots8TeV/barplot_blue_orange_SUSY2013.pdf (2013).

-
- [115] H. Zhang, Q.-H. Cao, C.-R. Chen, and C. S. Li, J. High Energy Physics **2011** (2011), arXiv:0912.4511 .
- [116] N. Zhou, D. Berge, and D. Whiteson, Phys. Rev. D **87**, 095013 (2013), arXiv:1302.3619 .
- [117] P. J. Fox, R. Harnik, J. Kopp, and Y. Tsai, Phys. Rev. D **85**, 056011+ (2011), arXiv:1109.4398 .
- [118] H. Baer, E.-K. Park, and X. Tata, New J. Phys. **11**, 105024+ (2009), arXiv:0903.0555 .
- [119] O. Buchmuller, M. J. Dolan, and C. McCabe, J. High Energy Phys. **2014** (2014), arXiv:1308.6799 .
- [120] G. Busoni, A. De Simone, E. Morgante, and A. Riotto, Phys. Lett. B **728**, 412 (2013), arXiv:1307.2253 .
- [121] P. Bechtle, *et al.*, Journal of High Energy Physics **2012** (2012), arXiv:1204.4199 .
- [122] P. Bechtle, *et al.*, “Constrained supersymmetry after the higgs boson discovery: A global analysis with fittino,” (2013), arXiv:1310.3045 .
- [123] B. Barish and J. E. Brau, Int. J. Mod. Phys. A **28**, 1330039+ (2013), arXiv:1311.3397 .
- [124] D. Schmeier, “Effective models for dark matter at the international linear collider,” (2013), arXiv:1308.4409 .
- [125] Y. J. Chae and M. Perelstein, Journal of High Energy Physics **2013** (2013), arXiv:1211.4008 .
- [126] M. Ackermann, *et al.* (Fermi-LAT), Physical Review D **86**, 022002 (2012), arXiv:1205.2739 .
- [127] M. Boezio, *et al.*, New J. Phys. **11**, 105023+ (2009).
- [128] M. Aguilar, *et al.* (AMS Collaboration), Physical Review Letters **110** (2013).
- [129] A. Ibarra, A. S. Lamperstorfer, and J. Silk, Phys. Rev. D **89**, 063539 (2014), arXiv:1309.2570 .

-
- [130] G. A. Medina Tanco, E. M. de Gouveia Dal Pino, and J. E. Horvath, *Astrophys. J.* **492**, 200 (1998).
- [131] J. Lavalle, Q. Yuan, D. Maurin, and X. J. Bi, *Astron. Astrophys.* **479**, 427 (2008), arXiv:0709.3634 .
- [132] M. Ackermann, *et al.* (Fermi-LAT Collaboration), *Phys. Rev. D* **89**, 042001 (2014), arXiv:1310.0828 .
- [133] C. Weniger, *J. Cosmol. Astropart. Phys.* **2012**, 007 (2012), arXiv:1204.2797 .
- [134] E. Bloom, E. Charles, E. Izaguirre, A. Snyder, A. Albert, B. Winer, Z. Yang, and R. Essig, “Search of the earth limb fermi data and Non-Galactic center region fermi data for signs of narrow lines,” (2013), arXiv:1303.2733 .
- [135] W. Buchmüller and M. Garny, *J. Cosmol. Astropart. Phys.* **2012**, 035 (2012), arXiv:1206.7056 .
- [136] T. Cohen, M. Lisanti, T. R. Slatyer, and J. G. Wacker, *J. High Energy Phys.* **2012** (2012), arXiv:1207.0800 .
- [137] L. Goodenough and D. Hooper, “Possible evidence for dark matter annihilation in the inner milky way from the fermi gamma ray space telescope,” (2009), arXiv:0910.2998 .
- [138] D. Hooper and L. Goodenough, *Phys. Lett. B* **697**, 412 (2011), arXiv:1010.2752 .
- [139] A. Boyarsky, D. Malyshev, and O. Ruchayskiy, *Phys. Lett. B* **705**, 165 (2010), arXiv:1012.5839 .
- [140] K. N. Abazajian, *J. Cosmol. Astropart. Phys.* **2011**, 010 (2011), arXiv:1011.4275 .
- [141] T. Daylan, D. P. Finkbeiner, D. Hooper, T. Linden, S. K. N. Portillo, N. L. Rodd, and T. R. Slatyer, “The characterization of the Gamma-Ray signal from the central milky way: A compelling case for annihilating dark matter,” (2014), arXiv:1402.6703 .
- [142] A. Abramowski, *et al.* (H.E.S.S. Collaboration), *Phys. Rev. Lett.* **110** (2013), arXiv:1301.1173 .

- [143] J. Aleksić, *et al.*, J. Cosmol. Astropart. Phys. **2014**, 008 (2014), arXiv:1312.1535 .
- [144] V. A. Acciari, *et al.*, Astrophys. J. **720**, 1174 (2010), arXiv:1006.5955 .
- [145] M. Doro, *et al.*, J. Astropart. Phys. **43**, 189 (2013).
- [146] J. Zornoza, Nucl. Instrum. Methods **725**, 76 (2013), arXiv:1204.5290 .
- [147] M. G. Aartsen, *et al.* (IceCube Collaboration), “The IceCube neutrino observatory part IV: Searches for dark matter and exotic particles,” (2013), arXiv:1309.7007 .
- [148] M. W. Goodman and E. Witten, Phys. Rev. D **31**, 3059 (1985).
- [149] A. K. Drukier, K. Freese, and D. N. Spergel, Phys. Rev. D **33**, 3495 (1986).
- [150] R. Bernabei, *et al.*, Eur. Phys. J. C **67**, 39 (2010), arXiv:1002.1028 .
- [151] C. Aalseth, *et al.* (CoGeNT Collaboration), Phys. Rev. Lett. **106**, 131301+ (2011).
- [152] C. E. Aalseth, *et al.*, Phys. Rev. Lett. **107**, 141301+ (2011), arXiv:1106.0650 .
- [153] L. Stodolsky, *et al.*, J. Phys.: Conf. Ser. **384**, 012013+ (2012), arXiv:1203.6835 .
- [154] D. S. Akerib, *et al.* (LUX Collaboration), Phys. Rev. Lett. **112** (2014), arXiv:1310.8214 .
- [155] D. G. Cerdeño and A. M. Green, “Direct detection of WIMPs,” in *Particle Dark Matter*, edited by G. Bertone and G. Bertone (Cambridge University Press, Cambridge, 2010) Chap. 17, pp. 347–369, arXiv:1002.1912 .
- [156] A. Kurylov and M. Kamionkowski, Phys. Rev. D **69**, 063503 (2003), arXiv:hep-ph/0307185 .
- [157] K. Freese, J. Frieman, and A. Gould, Phys. Rev. D **37**, 3388 (1988).

-
- [158] A. L. Fitzpatrick, W. Haxton, E. Katz, N. Lubbers, and Y. Xu, J. Cosmol. Astropart. Phys. **2013**, 004 (2013), arXiv:1203.3542 .
- [159] J. M. Alarcón, J. M. Camalich, and J. A. Oller, Phys. Rev. D **85**, 051503 (2012), arXiv:1110.3797 .
- [160] G. S. Bali, *et al.* (QCDSF Collaboration), Phys. Rev. D **85**, 054502 (2012), arXiv:1111.1600 .
- [161] M. Shifman, A. Vainshtein, and V. Zakharov, Phys. Lett. B **78**, 443 (1978).
- [162] J. Engel, Phys. Lett. B **264**, 114 (1991).
- [163] J. Engel, S. Pittel, and P. Vogel, Int. J. Mod. Phys. E **01**, 1 (1992).
- [164] S. Scholl and J. Jochum, J. Phys.: Conf. Ser. **375**, 012020+ (2012).
- [165] E. Aprile, *et al.*, J. Phys. G **40**, 115201+ (2013), arXiv:1306.2303 .
- [166] A. Münster, *et al.*, “Radiopurity of CaWO₄ crystals for direct dark matter search with CRESST and EURECA,” (2014), arXiv:1403.5114 .
- [167] R. Bernabei, *et al.*, Nucl. Instrum. Methods A **592**, 297 (2008), arXiv:0804.2738 .
- [168] M. Kuźniak, M. Boulay, and T. Pollmann, J. Astropart. Phys. **36**, 77 (2012), arXiv:1203.1576 .
- [169] C. Galbiati, *et al.*, J. Phys.: Conf. Ser. **120**, 042015+ (2008), arXiv:0712.0381 .
- [170] K. Abe, J. Hosaka, T. Iida, M. Ikeda, K. Kobayashi, Y. Koshio, A. Minamino, M. Miura, S. Moriyama, and M. Nakahata, Astropart. Phys. **31**, 290 (2009).
- [171] E. Aprile, T. Yoon, A. Loose, L. W. Goetzke, and T. Zelevinsky, Rev. Sci. Instrum. **84**, 093105+ (2013), arXiv:1305.6510 .
- [172] Z. Ahmed *et al.* (CDMS Collaboration), (2009), arXiv:0912.3592 .
- [173] Z. Ahmed, *et al.* (CDMS Collaboration), Phys. Rev. Lett. **106** (2011), arXiv:1011.2482 .

- [174] R. Agnese, *et al.*, Phys. Rev. Lett. **111** (2013), arXiv:1304.4279 .
- [175] G. Angloher, *et al.*, Eur. Phys. J. C **72** (2012), arXiv:1109.0702 .
- [176] C. E. Aalseth, *et al.*, Phys. Rev. D **88** (2013), arXiv:1208.5737 .
- [177] C. E. Aalseth, *et al.*, “Search for an annual modulation in three years of CoGeNT dark matter detector data,” (2014), arXiv:1401.3295 .
- [178] C. E. Aalseth, *et al.*, “Maximum likelihood signal extraction method applied to 3.4 years of CoGeNT data,” (2014), arXiv:1401.6234 .
- [179] E. Armengaud, *et al.*, Phys. Lett. B **702**, 329 (2011), arXiv:1103.4070 .
- [180] D. Akimov, *et al.*, Phys. Lett. B **709**, 14 (2012), arXiv:1110.4769 .
- [181] E. Aprile, *et al.* (XENON Collaboration), Phys. Rev. Lett. **107**, 131302+ (2011), arXiv:1104.2549 .
- [182] A. Marchionni, *et al.*, J. Phys.: Conf. Ser. **308**, 012006+ (2011), arXiv:1012.5967 .
- [183] A. Badertscher, *et al.*, J. Instrum. **8**, C09005+ (2013).
- [184] M. Boulay and B. Cai (DEAP/CLEAN Collaboration), Journal of Physics: Conference Series **136**, 042081+ (2008).
- [185] E. Behnke, *et al.*, Phys. Rev. Lett. **106**, 021303+ (2011).
- [186] M. Felizardo, *et al.* (SIMPLE Collaboration), Phys. Rev. Lett. **108** (2012), arXiv:1106.3014 .
- [187] S. Archambault, *et al.* (PICASSO Collaboration), Phys. Lett. B **711**, 153 (2012), arXiv:1202.1240 .
- [188] S. K. Kim, H. J. Kim, and Y. D. Kim, New J. Phys. **12**, 075003+ (2010).
- [189] R. Bernabei, *et al.*, Eur. Phys. J. C **56**, 333 (2008), arXiv:0804.2741 .
- [190] R. Bernabei, *et al.*, Eur. Phys. J. C **73** (2013), arXiv:1308.5109 .
- [191] H. S. Lee, *et al.*, Phys. Rev. Lett. **99** (2007), arXiv:0704.0423 .

-
- [192] B. Ahmed, *et al.*, J. Astropart. Phys. **19**, 691 (2003), arXiv:hep-ex/0301039 .
- [193] R. Bernabei, *et al.*, Riv. Nuovo Cimento **26**, 1 (2003), arXiv:astro-ph/0307403 .
- [194] P. Belli, R. Bernabei, A. Bottino, F. Cappella, R. Cerulli, N. Fornengo, and S. Scopel, Phys. Rev. D **84**, 055014 (2011), arXiv:1106.4667 .
- [195] D. Hooper, J. I. Collar, J. Hall, D. McKinsey, and C. Kelso, Phys. Rev. D **82**, 123509+ (2010), arXiv:1007.1005 .
- [196] R. Agnese, *et al.*, “Search for Low-Mass WIMPs with SuperCDMS,” (2014), arXiv:1402.7137 .
- [197] N. Bozorgnia, G. B. Gelmini, and P. Gondolo, J. Cosmol. Astropart. Phys. **2010**, 019 (2010), arXiv:1006.3110 .
- [198] K. Blum, “DAMA vs. the annually modulated muon background,” (2011), arXiv:1110.0857 .
- [199] R. Bernabei, *et al.*, Eur. Phys. J. C **72**, 1 (2012), arXiv:1202.4179 .
- [200] M. Fairbairn and T. Schwetz, J. Cosmol. Astropart. Phys. **2009**, 037 (2009), arXiv:0808.0704 .
- [201] J. Herrero-Garcia, T. Schwetz, and J. Zupan, Phys. Rev. Lett. **109** (2012), arXiv:1205.0134 .
- [202] P. J. Fox, J. Liu, and N. Weiner, Phys. Rev. D **83** (2011), arXiv:1011.1915 .
- [203] M. T. Frandsen, F. Kahlhoefer, C. McCabe, S. Sarkar, and K. Schmidt-Hoberg, J. Cosmol. Astropart. Phys. **2012**, 024 (2012), arXiv:1111.0292 .
- [204] M. R. Buckley and W. H. Lippincott, Phys. Rev. D **88**, 056003 (2013), arXiv:1306.2349 .
- [205] J. L. Feng, J. Kumar, D. Marfatia, and D. Sanford, Phys. Lett. B **703**, 124 (2011), arXiv:1102.4331 .

- [206] D. Smith and N. Weiner, Phys. Rev. D **64**, 043502 (2001), arXiv:hep-ph/0101138 .
- [207] R. Foot, Phys. Lett. B **728**, 45 (2014), arXiv:1305.4316 .
- [208] T. Schwetz and J. Zupan, J. Cosmol. Astropart. Phys. **2011**, 008 (2011), arXiv:1106.6241 .
- [209] E. Aprile, *et al.* (XENON Collaboration), Phys. Rev. Lett. **111** (2013), arXiv:1301.6620 .
- [210] E. Aprile, *et al.* (XENON Collaboration), Phys. Rev. Lett. **109**, 181301 (2013), arXiv:1207.5988 .
- [211] D. C. Mallin, *et al.*, “After LUX: The LZ program,” (2011), arXiv:1110.0103 .
- [212] E. Aprile, “The Xenon1T dark matter search experiment,” in *Sources and Detection of Dark Matter and Dark Energy in the Universe*, Vol. 148, edited by D. Cline (Springer Netherlands, Dordrecht, 2012) Chap. 14, pp. 93–96, arXiv:1206.6288 .
- [213] H. Kraus, *et al.*, Nucl. Phys. B: Proc. Suppl. **173**, 168 (2007).
- [214] S. Roth, C. Ciemniak, C. Coppi, F. Feilitzsch, A. Gütlein, C. Isaila, J. Lanfranchi, S. Pfister, W. Potzel, and W. Westphal, J. Opt. Mater. **31**, 1415 (2009), arXiv:0810.0423 .
- [215] L. Baudis (DARWIN consortium), J. Phys.: Conf. Ser. **375**, 012028+ (2012), arXiv:1201.2402 .
- [216] A. Drukier, K. Freese, D. Spergel, C. Cantor, G. Church, and T. Sano, “New dark matter detectors using DNA for nanometer tracking,” (2012), arXiv:1206.6809 .
- [217] A. Lopez, A. Drukier, K. Freese, C. Kurdak, and G. Tarle, “New dark matter detector using nanoscale explosives,” (2014), arXiv:1403.8115 .
- [218] A. A. Aguilar-Arevalo, *et al.* (DAMIC Collaboration), “DAMIC: a novel dark matter experiment,” (2013), arXiv:1310.6688 .
- [219] P. deNiverville, D. McKeen, and A. Ritz, Phys. Rev. D **86**, 035022 (2012), arXiv:1205.3499 .

- [220] B. Borasoy and Ulf-G, Phys. Lett. B **365**, 285 (1995), arXiv:hep-ph/9508354 .
- [221] M. M. Pavan, I. I. Strakovsky, R. L. Workman, and R. A. Arndt, “The pion-nucleon sigma term is definitely large: results from a G.W.u. analysis of pion nucleon scattering data,” (2001), arXiv:hep-ph/0111066 .
- [222] L. Alvarez-ruso, T. Ledwig, M. J. Vicente Vacas, and J. Martin-camalich, Int. J. Mod. Phys.: Conf. Ser. **26**, 1460089+ (2014), arXiv:1402.1031 .
- [223] J. Ashman, *et al.*, Phys. Lett. B **206**, 364 (1988).
- [224] R. L. Jaffe and A. Manohar, Nucl. Phys. B **337**, 509 (1990).
- [225] D. Adams, Phys. Rev. D **56**, 5330 (1997), arXiv:hep-ex/9702005 .
- [226] D. Qing, X.-S. Chen, and F. Wang, Phys. Rev. C **57**, R31 (1998).
- [227] A. Thomas, Phys. Rev. Lett. **101**, 102003+ (2008).
- [228] R. Helm, Phys. Rev. **104**, 1466 (1956).
- [229] J. D. Lewin and P. F. Smith, Astropart. Phys. **6**, 87 (1996).
- [230] G. Fricke, C. Bernhardt, K. Heilig, L. Schaller, L. Schellenberg, E. Shera, and C. Dejager, At. Data. Nucl. Data Tables **60**, 177 (1995).
- [231] G. Dda, A. Kemper, and P. Gondolo, J. Cosmol. Astropart. Phys. **2007**, 012 (2007), arXiv:hep-ph/0608035 .
- [232] G. Co’, V. De Donno, M. Anguiano, and A. M. Lallena, J. Cosmol. Astropart. Phys. **2012**, 010+ (2012).
- [233] C. Ya-Zheng, C. Jun-Mou, L. Yan-An, S. Hong, and L. Xue-Qian, Chin. Phys. C **36**, 505+ (2012).
- [234] M. Cannoni, Phys. Rev. D **87**, 075014 (2013), arXiv:1211.6050 .
- [235] M. Ressel and D. Dean, Phys. Rev. C **56**, 535 (1997), hep-ph/9702290 .
- [236] J. Engel and P. Vogel, Phys. Rev. D **40**, 3132 (1989).

- [237] F. Iachello, L. M. Krauss, and G. Maino, *Phys. Lett. B* **254**, 220 (1991).
- [238] J. Ellis and R. A. Flores, *Nucl. Phys. B* **307**, 883 (1988).
- [239] D. G. Cerdeno, M. Fornasa, J.-H. Huh, and M. Peiro, *Phys. Rev. D* **87**, 023512 (2012), arXiv:1208.6426 .
- [240] J. Kumar, *Int. J. Mod. Phys.: Conf. Ser.* **10**, 115 (2012), arXiv:1201.0217 .
- [241] K. Hamaguchi, S. P. Liew, T. Moroi, and Y. Yamamoto, “Isospin-Violating dark matter with colored mediators,” (2014), arXiv:1403.0324 .
- [242] K. Schmidt-Hoberg, F. Staub, and M. W. Winkler, *Phys. Lett. B* **727**, 506 (2013), arXiv:1310.6752 .
- [243] H. An, L.-T. Wang, and H. Zhang, “Dark matter with $t\bar{t}$ -channel mediator: a simple step beyond contact interaction,” (2014), arXiv:1308.0592 .
- [244] M. Pospelov and T. T. Veldhuis, *Phys. Lett. B* **480**, 181 (2000), arXiv:hep-ph/0003010 .
- [245] C. M. Ho and R. J. Scherrer, *Phys. Lett. B* **722**, 341 (2013), arXiv:1211.0503 .
- [246] J. Fan, M. Reece, and L.-T. Wang, *J. Cosmol. Astropart. Phys.* **2010**, 042 (2010), arXiv:1008.1591 .
- [247] M. Cirelli, E. D. Nobile, and P. Panci, *J. Cosmol. Astropart. Phys.* **2013**, 019 (2013), arXiv:1307.5955 .
- [248] R. Catena and P. Ullio, *J. Cosmol. Astropart. Phys.* **2010**, 004 (2010), arXiv:0907.0018 .
- [249] M. Weber and W. de Boer, *Astron. Astrophys.* **509**, A25+ (2010), arXiv:0910.4272 .
- [250] F. Nesti and P. Salucci, *J. Cosmol. Astropart. Phys.* **07**, 016 (2013), arXiv:1304.5127 .

- [251] S. Garbari, C. Liu, J. I. Read, and G. Lake, *Mon. Not. R. Astron. Soc.* **425**, 1445 (2012), arXiv:1206.0015 .
- [252] F. Iocco, M. Pato, G. Bertone, and P. Jetzer, *J. Cosmol. Astropart. Phys.* **11**, 029 (2011), arXiv:1107.5810 .
- [253] P. Salucci, F. Nesti, G. Gentile, and C. Frigerio Martins, *Astron. Astrophys.* **523**, A83+ (2010), arXiv:1003.3101 .
- [254] C. Moni Bidin, G. Carraro, R. A. Méndez, and R. Smith, *Astrophys. J.* **751**, 30+ (2012), arXiv:1204.3924 .
- [255] J. Bovy and S. Tremaine, *Astrophys. J.* **756**, 89 (2012), arXiv:1205.4033 .
- [256] A. M. Green, *Mod. Phys. Lett. A* **27**, 1230004 (2012), arXiv:1112.0524 .
- [257] F. J. Kerr and D. Lynden-Bell, *Mon. Not. R. Astron. Soc.* **221**, 1023 (1986).
- [258] M. Feast and P. Whitelock, *Mon. Not. R. Astron. Soc.* **291**, 683 (1997), arXiv:astro-ph/9706293 .
- [259] R. Schönrich, *Mon. Not. R. Astron. Soc.* **427**, 274 (2012), arXiv:1207.3079 .
- [260] J. Bovy, *et al.*, *Astrophys. J.* **759**, 131+ (2012), arXiv:1209.0759 .
- [261] M. C. Smith, *et al.*, *Mon. Not. R. Astron. Soc.* **379**, 755 (2007), astro-ph/0611671 .
- [262] T. Piffl, *et al.*, *Astron. Astrophys.* **562**, A91+ (2014), arXiv:1309.4293 .
- [263] N. W. Evans, C. M. Carollo, and P. T. de Zeeuw, *Mon. Not. R. Astron. Soc.* **318**, 1131 (2000), arXiv:astro-ph/0008156 .
- [264] L. M. Widrow, *Astrophys. J. Suppl. Ser.* **131**, 39 (2000).
- [265] M. Lisanti, L. E. Strigari, J. G. Wacker, and R. H. Wechsler, *Phys. Rev. D* **83**, 023519 (2011), arXiv:1010.4300 .

-
- [266] P. Bhattacharjee, S. Chaudhury, S. Kundu, and S. Majumdar, Phys. Rev. D **87**, 083525 (2013), arXiv:1210.2328 .
- [267] M. Fornasa and A. M. Green, Phys. Rev. D **89** (2013), arXiv:1311.5477 .
- [268] M. Vogelsberger, A. Helmi, V. Springel, S. D. M. White, J. Wang, C. S. Frenk, A. Jenkins, A. Ludlow, and J. F. Navarro, Mon. Not. R. Astron. Soc. **395**, 797 (2009), arXiv:0812.0362 .
- [269] M. Kuhlen, N. Weiner, J. Diemand, P. Madau, B. Moore, D. Potter, J. Stadel, and M. Zemp, J. Cosmol. Astropart. Phys. **02**, 030 (2010), arXiv:0912.2358 .
- [270] Y.-Y. Mao, L. E. Strigari, R. H. Wechsler, H.-Y. Wu, and O. Hahn, Astrophys. J. **764**, 35 (2012), arXiv:1210.2721 .
- [271] M. Kuhlen, M. Lisanti, and D. N. Spergel, Phys. Rev. D **86**, 063505 (2012), arXiv:1202.0007 .
- [272] J. I. Read, L. Mayer, A. M. Brooks, F. Governato, and G. Lake, Mon. Not. R. Astron. Soc. **397**, 44 (2009), arXiv:0902.0009 .
- [273] J. I. Read, *et al.*, AIP Conf. Proc. **1240**, 391 (2010), arXiv:0901.2938 .
- [274] A. M. Green, J. Cosmol. Astropart. Phys. **10**, 034 (2010), arXiv:1009.0916 .
- [275] M. Fairbairn, T. Douce, and J. Swift, J. Astropart. Phys. **47**, 45 (2013), arXiv:1206.2693 .
- [276] L. E. Strigari and R. Trotta, J. Cosmol. Astropart. Phys. **2009**, 019 (2009), arXiv:0906.5361 .
- [277] A. H. G. Peter, Phys. Rev. D **81**, 087301+ (2010), arXiv:0910.4765 .
- [278] C. Arina, G. Bertone, and H. Silverwood, Phys. Rev. D **88** (2013), arXiv:1304.5119 .
- [279] M. Pato, L. Baudis, G. Bertone, R. R. de Austri, L. E. Strigari, and R. Trotta, Phys. Rev. D **83** (2011), arXiv:1012.3458 .

-
- [280] M. Pato, L. E. Strigari, R. Trotta, and G. Bertone, *J. Cosmol. Astropart. Phys.* **2013**, 041 (2013), arXiv:1211.7063 .
- [281] M. Drees and C.-L. Shan, *J. Cosmol. Astropart. Phys.* **2007**, 011 (2007), arXiv:astro-ph/0703651 .
- [282] M. Drees and C.-L. Shan, *J. Cosmol. Astropart. Phys.* **2008**, 012+ (2008), arXiv:0803.4477 .
- [283] B. Feldstein and F. Kahlhoefer, “A new halo-independent approach to dark matter direct detection analysis,” (2014), arXiv:1403.4606 .
- [284] P. Gondolo and G. B. Gelmini, *J. Cosmol. Astropart. Phys.* **2012**, 015 (2012), arXiv:1202.6359 .
- [285] E. D. Nobile, G. Gelmini, P. Gondolo, and J.-H. Huh, *J. Cosmol. Astropart. Phys.* **2013**, 048 (2013), arXiv:1306.5273 .
- [286] S. S. Wilks, *Ann. Math. Stat.* **9**, 60 (1938).
- [287] A. Lewis and S. Bridle, “Parameter estimation using monte carlo sampling,” in *Bayesian Methods in Cosmology*, edited by M. P. Hobson, A. H. Jaffe, A. R. Liddle, P. Mukherjee, and D. Parkinson (Cambridge University Press, Cambridge, 2009) Chap. 3, pp. 57–78.
- [288] N. Metropolis, A. W. Rosenbluth, M. N. Rosenbluth, A. H. Teller, and E. Teller, *J. Chem. Phys.* **21**, 1087 (1953).
- [289] A. Lewis and S. Bridle, *Phys. Rev. D* **66**, 103511 (2002), astro-ph/0205436 .
- [290] S. Kirkpatrick, C. D. Gelatt, and M. P. Vecchi, *Science* **220**, 671 (1983).
- [291] J. Skilling, in *BAYESIAN INFERENCE AND MAXIMUM ENTROPY METHODS IN SCIENCE AND ENGINEERING: 24th International Workshop on Bayesian Inference and Maximum Entropy Methods in Science and Engineering*, Vol. 735 (AIP, 2004) pp. 395–405.
- [292] F. Feroz and M. P. Hobson, *Mon. Not. R. Astron. Soc.* **384**, 449 (2007), arXiv:0704.3704 .

- [293] F. Feroz, M. P. Hobson, and M. Bridges, *Mon. Not. R. Astron. Soc.* **398**, 1601 (2008), arXiv:0809.3437 .
- [294] F. Feroz, M. P. Hobson, E. Cameron, and A. N. Pettitt, “Importance nested sampling and the MultiNest algorithm,” (2014), arXiv:1306.2144 .
- [295] E. Aprile, (2009), http://xenon.astro.columbia.edu/presentations/Aprile_SJTU09.pdf.
- [296] T. Bruch (CDMS collaboration), (2010), arXiv:1001.3037 .
- [297] A. M. Szelc (WArP collaboration), *AIP Conf. Proc.* **1115**, 105 (2009).
- [298] E. Aprile, L. Baudis, B. Choi, K. L. Giboni, K. Lim, A. Manalaysay, M. E. Monzani, G. Plante, R. Santorelli, and M. Yamashita, *Phys. Rev. C* **79**, 045807+ (2009), arXiv:0810.0274 .
- [299] C. Stenge, R. Trotta, G. Bertone, A. H. G. Peter, and P. Scott, *Phys. Rev. D* **86**, 023507 (2012), arXiv:1201.3631 .
- [300] L. Demortier and L. Lyons, (2002), www-cdf.fnal.gov/physics/statistics/notes/cdf5776-pulls.ps.gz.
- [301] C. W. Purcell, J. S. Bullock, and M. Kaplinghat, *Astrophys. J.* **703**, 2275 (2009), arXiv:0906.5348 .
- [302] J. Diemand, M. Kuhlen, P. Madau, M. Zemp, B. Moore, D. Potter, and J. Stadel, *Nature* **454**, 735 (2008), arXiv:0805.1244 .
- [303] W. Gautschi, in *Recent advances in numerical analysis*, edited by C. De Boor and G. H. Golub (Academic Press, New York, 1978) pp. 45–72.
- [304] J. H. Wilkinson, in *Studies in numerical analysis*, edited by G. H. Golub (Mathematical Association of America, 1984) p. 3.
- [305] J. C. Mason and D. C. Handscomb, *Chebyshev polynomials*, 1st ed. (Chapman & Hall/CRC, 2002).
- [306] E. Aprile, “XENON1T at LNGS: Proposal April 2010,” www.bo.infn.it/xenon/docs/xe1t_proposal_v2.pdf (2010).

- [307] P. Benetti *et al.*, J. Astropart. Phys. **28**, 495 (2007), arXiv:astro-ph/0701286 .
- [308] L. Grandi, *WARP: an argon double phase technique for Dark Matter search*, Ph.D. thesis, Department of Nuclear and Theoretical Physics, University of Pavia (2005).
- [309] D. Bauer, “SuperCDMS SNOLAB,” <https://indico.fnal.gov/getFile.py/access?sessionId=1&resId=0&materialId=0&confId=6584> (2013).
- [310] D. Bauer, “SuperCDMS update,” www.fnal.gov/directorate/program_planning/all_experimenters_meetings/special_reports/Bauer_supercdms_status_02_04_13.pdf (2013).
- [311] G. Cowan, K. Cranmer, E. Gross, and O. Vitells, Eur. Phys. J. C **71**, 1 (2013), arXiv:1007.1727 .
- [312] G. Schwarz, Ann. Stat. **6**, 461 (1978).
- [313] A. Green and B. Morgan, Phys. Rev. D **77**, 027303 (2008).
- [314] P. Gondolo, Phys. Rev. D **66** (2002), arXiv:hep-ph/0209110 .
- [315] C. J. Copi, J. Heo, and L. M. Krauss, Phys. Lett. B **461**, 43 (1999), arXiv:hep-ph/9904499 .
- [316] C. J. Copi and L. M. Krauss, Phys. Rev. D **67** (2002), arXiv:astro-ph/0208010 .
- [317] B. Morgan, A. Green, and N. Spooner, Phys. Rev. D **71**, 103507 (2005), arXiv:astro-ph/0408047 .
- [318] E. Daw, *et al.*, Astropart. Phys. **35**, 397 (2012), arXiv:1010.3027 .
- [319] E. Daw, *et al.*, EAS Publ. Ser. **53**, 11 (2012), arXiv:1110.0222 .
- [320] K. Miuchi, *et al.*, Phys. Lett. B **686**, 11 (2010), arXiv:1002.1794 .
- [321] K. Miuchi, *et al.*, EAS Publ. Ser. **53**, 33 (2012), arXiv:1109.3099 .
- [322] Q. Riffard, *et al.*, “Dark matter directional detection with MIMAC,” (2013), arXiv:1306.4173 .

- [323] D. Santos, *et al.*, J. Phys.: Conf. Ser. **469**, 012002+ (2013), arXiv:1311.0616 .
- [324] J. Monroe (DMTPC Collaboration), EAS Publ. Ser. **53**, 19 (2012).
- [325] J. B. R. Battat (DMTPC Collaboration), J. Phys.: Conf. Ser. **469**, 012001+ (2013).
- [326] S. Vahsen, H. Feng, M. Garcia-Sciveres, I. Jaegle, J. Kadyk, Y. Nguyen, M. Rosen, S. Ross, T. Thorpe, and J. Yamaoka, EAS Publ. Ser. **53**, 43 (2012).
- [327] J. Billard, F. Mayet, and D. Santos, J. Cosmol. Astropart. Phys. **2012**, 006 (2012), arXiv:1202.3372 .
- [328] S. Burgos, *et al.*, Astropart. Phys. **31**, 261 (2008), arXiv:0809.1831 .
- [329] T. Naka, M. Kimura, M. Nakamura, O. Sato, T. Nakano, T. Asada, Y. Tawara, and Y. Suzuki, EAS Publ. Ser. **53**, 51 (2012), arXiv:1109.4485 .
- [330] S. Ahlen, *et al.*, Int. J. Mod. Phys. A **25**, 1 (2009), arXiv:0911.0323 .
- [331] D. S. M. Alves, S. E. Hedri, and J. G. Wacker, “Dark matter in 3D,” (2012), arXiv:1204.5487 .
- [332] M. Kuhlen, J. Diemand, P. Madau, and M. Zemp, J. Phys.: Conf. Ser. **125**, 012008+ (2008), arXiv:0810.3614 .
- [333] S. K. Lee, “Harmonics in the Dark-Matter sky: Directional detection in the Fourier-Bessel basis,” (2014), arXiv:1401.6179 .
- [334] S. Helgason, *The Radon Transform*, 2nd ed. (Birkhauser, Boston, 1999).
- [335] E. T. Quinto, J. Math. Anal. Appl. **91**, 510 (1983).
- [336] L. A. Shepp and J. B. Kruskal, Amer. Math. Soc. **85**, 420 (1978).
- [337] E. T. Quinto, J. Math. Anal. Appl. **90**, 408 (1982).